

2004

SCANNING ACOUSTIC MICROSCOPE FOR CHARACTERIZATION OF ARTERIAL PLAQUE

<https://hdl.handle.net/2144/1381>

Boston University

BOSTON UNIVERSITY

COLLEGE OF ENGINEERING

Thesis

**SCANNING ACOUSTIC MICROSCOPE FOR
CHARACTERIZATION OF ARTERIAL PLAQUE**

by

CALEB HOOPER FARNY

B.S., University of Rochester, 2001

Submitted in partial fulfillment of the

requirements for the degree of

Master of Science

2004

Approved by

Advisor:

Robin O. Cleveland, Ph.D.

Associate Professor, Aerospace and Mechanical Engineering

Second Reader:

Ronald A. Roy, Ph.D.

Professor, Aerospace and Mechanical Engineering

Third Reader:

T.L. Szabo, Ph.D.

Research Professor, Aerospace and Mechanical Engineering

Acknowledgements

I would like thank Professors Cleveland, Roy and Szabo for sitting on my thesis committee. Tom Szabo's and Ron Roy's critical reading helped make this document comprehensible to everyone unfamiliar with my work. I would like to particularly extend my gratitude to my advisor Dr. Robin Cleveland for his endless patience and counsel throughout the course of my master's research. My knowledge regarding acoustics, experimental setup and a logical method for tackling problems has been greatly expanded thanks to his tutelage.

My tissue study could not have been executed without the help of Dr. Marvin Doyley and an anonymous donor(s-?) somewhere in the Hanover, NH area. I owe a great debt to the Center for Subsurface Sensing and Imaging Systems and the National Science Foundation for supporting my work.

I would also like to thank my fellow students in the Physical Acoustics Group. Specifically, Tara Chklovski for helping introduce me to the project and answering my countless questions. The 'corner office' of Rm. 405, Javier Van Cauwelaert, Parag Chitnis and Paolo Zanetti, deserves special recognition for the many distractions and pieces of advice which were important in helping me along the way. Finally, Preston Wilson, Charlie Thomas, Constantin Coussios, Mike Richards, Jed Wilbur, Xinmai Yang, Li Liu, Lei Sui, Oluwaseyi Balogun, Eun-Joo Park, Yuan Jing, and Carmin Rodriguez were all helpful in providing advice and discussion.

I owe a large debt of gratitude to Joe Estano and Dave Campbell for helping me with the design process and construction of my experiments.

Thanks to my family and to my roommate, Brian Montana, for the support and nec-

essary distractions away from school.

Finally I thank my girlfriend, Natalie Gilks, for her support and understanding of the many late nights.

The path through my master's research was a long one that I couldn't have done without all your help. I'm sure I have omitted some names but please know it's not on purpose!

**SCANNING ACOUSTIC MICROSCOPE FOR
CHARACTERIZATION OF ARTERIAL PLAQUE**

CALEB HOOPER FARNY

ABSTRACT

Unstable arterial plaque is likely the key component of atherosclerosis, a disease which is responsible for two-thirds of heart attacks and strokes, leading to approximately 1 million deaths in the United States. Ultrasound imaging is able to detect plaque but as of yet is not able to distinguish unstable plaque from stable plaque. In this work a scanning acoustic microscope (SAM) was implemented and validated as tool to measure the acoustic properties of a sample. The goal for the SAM is to be able to provide quantitative measurements of the acoustic properties of different plaque types, to understand the physical basis by which plaque may be identified acoustically.

The SAM consists of a spherically focused transducer which operates in pulse-echo mode and is scanned in a 2D raster pattern over a sample. A plane wave analysis is presented which allows the impedance, attenuation and phase velocity of a sample to be determined from measurements of the echoes from the front and back of the sample. After the measurements, the attenuation and phase velocity were analysed to ensure that they were consistent with causality. The backscatter coefficient of the samples was obtained using the technique outlined by Chen et al [8]. The transducer used here was able to determine

acoustic properties from 10-40 MHz. The results for the impedance, attenuation and phase velocity were validated for high and low-density polyethylene against published results. The plane wave approximation was validated by measuring the properties throughout the focal region and throughout a range of incidence angles from the transducer. The SAM was used to characterize a set of recipes for tissue-mimicking phantoms which demonstrate independent control over the impedance, attenuation, phase velocity and backscatter coefficient. An initial feasibility study on a human artery was performed.

Contents

1	Introduction	1
1.1	The human artery	2
1.1.1	Plaque types	4
1.2	Detection techniques	5
1.2.1	IVUS measurements	8
1.3	Measurements for SAM	11
1.3.1	The backscatter coefficient	12
1.3.2	Tissue Phantom	15
2	Theory of Measurements	18
2.1	Pulse Measurements	19
2.1.1	Phase Velocity	24
2.1.2	Specific Acoustic Impedance	26
2.1.3	Attenuation	26

2.2	Time Causal Model	27
2.3	Backscatter Coefficient	28
3	Experiment and Validation	40
3.1	Experimental Setup	40
3.2	Glass Reference Measurement	50
3.3	Validation of the Phase Velocity and Attenuation	51
3.3.1	Uncertainty	56
3.3.2	HDPE results	57
3.3.3	HDPE Comparison	62
3.3.4	LDPE results	66
3.3.5	LDPE comparison	69
3.4	Impedance Measurements	72
3.5	Focal Region	79
3.6	Insonification Angle	87
4	Tissue Phantoms	92
4.1	Phantom Recipe	92
4.2	Construction Protocol	95
4.3	Phantom Scan	98
4.4	Results	100

4.4.1	Base recipe	100
4.4.2	Silica variation	102
4.4.3	Propanol variation	111
4.4.4	Gelatin variation	114
4.4.5	Agar variation	117
5	Tissue Measurements	118
5.1	Measurement	118
5.2	Two-layer analysis	124
5.2.1	Results	127
6	Discussion/Conclusion	136
6.1	Validation of impedance, attenuation and phase velocity measurements . . .	137
6.2	Pulser energy settings	140
6.3	Focal region	141
6.4	Effect of transducer angle	141
6.5	Phantom measurements	142
6.6	Variations in phantom results	144
6.7	Tissue study	146
6.8	Summary and Conclusions	148
A	MATLAB Analysis Codes	150

List of Tables

1.1	Literature results for the backscatter coefficient $[(\text{m Sr})^{-1}]$ of the human artery	10
1.2	Literature results for the human artery (healthy)	11
1.3	Phantom Recipes by Percent Concentration	15
2.1	Coefficients for speed of sound in water [16]	20
2.2	Roberjot phantom properties	31
3.1	Sound speed of the glass reference	51
3.2	Comparison of manufacturer and measured values for HDPE density at 25 MHz	66
3.3	Pulser/Receiver settings	73
4.1	Basic phantom recipe, by percent weight	95
4.2	Phantom recipes for silica studies, by percent weight	104
4.3	Phantom recipes for propanol variation studies, by percent weight	111
4.4	Phantom recipes for gelatin variation studies, by percent weight	114

6.1	Measured and extrapolated results for HDPE at 10 and 35 MHz	137
6.2	Comparison of manufacturer and measured values for HDPE at 25 MHz . .	138
6.3	Measured and extrapolated results for LDPE at 10 and 35 MHz	139
6.4	Effect of silica concentration at 25 MHz	142
6.5	Effect of propanol concentration at 25 MHz	143
6.6	Effect of gelatin concentration at 25 MHz	144
6.7	Tissue results at 25 MHz	147

List of Figures

1.1	Human coronary artery. The blood travels through the lumen, in the center. The intima, media and adventitia make up the three main layers of the artery wall. <i>Photos courtesy of Cormack [12].</i>	2
1.2	Histological comparison of (a) stable and (b) unstable plaque. The stable plaque consists of a large fibrous structure on the inside of the artery. The unstable plaque is distinguished by a lipid pool covered by a thin fibrous cap. <i>Photos courtesy of CIMIT.</i>	5
1.3	IVUS image of a tissue-mimicking phantom. The bright ring in the center of the phantom is the sheath which contained the transducer. The white markers are at 2 mm spacing. The ultrasound pulse penetrated approximately 6 mm through the phantom.	8

- 2.1 The measurement for the phase velocity and attenuation: (a) the sample measurement consisted of a pulse reflected from the top surface and a pulse reflected from the bottom surface of the sample. (b) The reference measurement consisted of a pulse reflected from the top surface of the reference material. The top surfaces of the sample and the reference were positioned a distance D from the transducer surface. 19
- 2.2 The respective difference in the phase angle of the top and bottom surface echoes treated by the MATLAB and SAM unwrapping routines: the slopes should be flat, and the increases show where the MATLAB routine did not correct for the unwrapping. 25
- 2.3 The theoretical backscatter coefficient for the $4\ \mu\text{m}$, $82\ \mu\text{m}$ diameter beads (dotted and solid lines, respectively) and for the combined effect of the two beads, shown in the dashed-dotted line. The bead density was 1.27×10^{15} beads/ m^3 for the $4\ \mu\text{m}$ diameter beads and was 10^{10} beads/ m^3 for the larger $82\ \mu\text{m}$ diameter beads. . . . 32
- 2.4 Comparing scattering in two samples: (a) HDPE has no scattering particles. The pulse travels through water until the 300th data point, approximately, at which point it reaches the top surface of the sample. After the interface the signal travels through the sample. (b) Tissue phantom with 10% silica particles. The scatterers inside the phantom reflect the wave, causing a higher signal inside the phantom. The noise level for the two figures (the signal from the beginning of the window up to the surface reflection signal) appears differently since the measurements were taken with different voltage settings, resulting in different quantizations of the signals. 34
- 3.1 The block diagram for the SAM setup for the point-to-point scan configuration. . . 41

3.2	The block diagram for the SAM setup for the continuous-motion scan configuration.	42
3.3	The sample table for the SAM setup. The table was removed from the tank for clarity.	43
3.4	The SAM raster scan pattern for the reflection off the surface.	47
3.5	Time waveforms for the KP HDPE surfaces: (a) reflection from the top surface; (b) reflection from the bottom surface. Note the difference in the amplitude scale. . .	53
3.6	Frequency spectra for the KP HDPE surfaces for a pulser energy of $8\mu\text{J}$	54
3.7	Attenuation for the KP HDPE sample. All of the data points are plotted over the 0-100 MHz range. The data is in the noise region below 10 MHz and above 40 MHz.	55
3.8	Mean phase velocity for the KP HDPE with the standard deviation of the system.	57
3.9	Mean attenuation for the KP HDPE with the standard deviation of the system. The system uncertainty was highest at the higher frequencies.	58
3.10	Impedance for KP and LP HDPE samples. The slope was similar for both samples.	59
3.11	HDPE Attenuation results from the SAM. The LP had a slightly higher attenuation. The error bars are the standard deviation from the data.	59
3.12	Measured attenuation and power law fit of the measured data for the KP HDPE. The fit is within the standard deviation of the measurement.	60

3.13	Phase velocity results for the HDPE. The thicker KP sample had a higher sound speed than the LP sample but the slopes were similar. The TCM predicted lower dispersion at the lower frequencies for both samples. The larger error bars indicate the standard deviation of the measurement and the smaller error bars are the standard error.	61
3.14	Comparison of the HDPE attenuation values between the referenced results and the SAM over the 1-7 MHz range. The four studies fall within the same range and but the WHZ results exhibit a lower power law than the SAM results.	63
3.15	Comparison of the HDPE attenuation values between the referenced results and the SAM over the 10-35 MHz range. The SAM results have a higher attenuation at the higher frequencies because of the higher power law values.	64
3.16	Comparison of the HDPE phase velocity values from the referenced results and the extrapolated results from the SAM. None of the results agree but exhibit similar slopes.	65
3.17	Comparison of the HDPE phase velocity values from the SAM and the extrapolated WHZ results. The WHZ extrapolated results both exhibited a slightly lower slope than the SAM results.	65
3.18	SAM LDPE impedance results. The LDPE had a lower impedance than both HDPE samples.	67
3.19	SAM LDPE attenuation results. The LDPE had a higher attenuation than both HDPE samples.	68

3.20	LDPE Phase velocity measured by the SAM. The time causal model is within the standard error bars everywhere except the higher frequencies.	68
3.21	Comparison of the WHZ attenuation results with the SAM extrapolation for LDPE. The three studies fell within the same range.	69
3.22	Comparison of the SAM attenuation measurements with the WHZ extrapolations for LDPE. The SAM results were higher than the WHZ extrapolations because the SAM LDPE had a higher power law.	70
3.23	Comparison of the phase velocity of the WHZ results with the extrapolated results from the SAM for LDPE. The slopes are similar but there is a large spread in the results.	71
3.24	Comparison of the LDPE phase velocity results from the SAM and the extrapolated results from the referenced results. The SAM measurement is similar to the He and Zheng results but exhibits a steeper slope.	72
3.25	Initial experimental results for the HDPE impedance at multiple energy levels. ‘E’ indicates the energy.	74
3.26	Spectra of echoes from the glass reference at multiple energy levels.	75
3.27	Spectra of echoes from the top surface of HDPE at multiple energy levels.	75
3.28	HDPE impedance at 13 mm.	77
3.29	HDPE attenuation for each energy level, measured at a transducer-sample distance of 12 mm. The four results overlap their respective standard deviations.	77

3.30	HDPE phase velocity for each energy level, measured at a transducer-sample distance of 12 mm. The four results are similar but vary by approximately 4 m/s. The phase velocity for $E = 8 \mu\text{J}$ has the smallest standard deviation at the higher frequencies.	78
3.31	Frequency spectra of the echo from the top surface of HDPE placed at 9.5, 12 and 14.5 mm from the transducer.	80
3.32	HDPE phase velocity at 25 MHz as a function of transducer-sample distance. The phase velocity decreased as the sample was placed farther from the transducer. . .	81
3.33	HDPE attenuation at 15, 25 and 35 MHz as a function of the sample-transducer distance.	82
3.34	HDPE attenuation at 15, 25 and 35 MHz as a function of the sample-transducer distance normalized by the attenuation at the focal length.	83
3.35	HDPE impedance at 25 MHz per distance. The impedance peaks at the focal length.	84
3.36	The pressure of the glass reference at the 10, 20 and 35 MHz frequencies as a function of transducer-sample length, normalized by the response at 12 mm.	85
3.37	Frequency spectra from the reference at the 11.5 mm focal length.	87
3.38	HDPE phase velocity as a function of angle of incidence relative to the normal at 25 MHz. The phase velocity decreased as the angle increased.	89
3.39	HDPE attenuation at 25 MHz as a function of angle of incidence relative to the normal.	90
3.40	HDPE impedance at 25 MHz as a function of angle of incidence relative to the normal.	90

4.1	Molds used to construct the phantoms. The thickness varied, decreasing from left to right.	94
4.2	Specific acoustic impedance for the base phantom recipe.	101
4.3	Attenuation for the base phantom recipe.	102
4.4	Phase velocity for the base phantom recipe. The time causal model matched the measured results.	103
4.5	Backscatter coefficient for the base phantom recipe.	103
4.6	Specific acoustic impedance for the three silica concentrations at 25 MHz.	104
4.7	Attenuation for the 2% silica phantoms at 25 MHz.	105
4.8	Attenuation for the 6% silica phantoms at 25 MHz.	106
4.9	Attenuation for the 10% silica phantoms at 25 MHz.	106
4.10	Backscatter coefficient and thickness for the 2% silica phantoms at 25 MHz.	107
4.11	Backscatter coefficient and thickness for the 6% silica phantoms at 25 MHz.	109
4.12	Backscatter coefficient and thickness for the 10% silica phantoms at 25 MHz.	110
4.13	Mean attenuation and backscatter coefficient for the three silica concentrations at 25 MHz. Both the attenuation and the backscatter coefficient increased with the silica concentration.	111
4.14	Mean phase velocity for the propanol phantoms at 25 MHz. The phase velocity was expected to increase with an increase in propanol concentration. The range for the phase velocity in human arteries is included for reference.	112

4.15	Mean phase velocity for the four gelatin concentrations at 25 MHz.	114
4.16	Mean attenuation for the four gelatin concentrations at 25 MHz.	116
5.1	Femoral artery used for the SAM measurements. The artery measured approximately 130 mm in length and 12 mm in width.	119
5.2	The femoral artery. The intimal-medial layers and the adventitial layer became separated after being clamped and were visible to the eye.	120
5.3	The signal from the artery in a ‘good’ region. The echoes from the intima-media, media-adventitia and adventitia-water boundaries are clearly visible, delineating each layer. The adventitial layer features more backscatter than the other layers. .	121
5.4	A ‘poor’ signal from the artery. The echoes from the intima-media, media-adventitia and adventitia-water boundaries are clearly visible, delineating each layer. The medial layer features more backscatter than the other layers.	123
5.5	Reflections from a pulse through an artery. A healthy intima is nearly acoustically transparent, so the wave is reflected from the water-media, media-adventitia, and adventitia-water interfaces.	124
5.6	Phase velocity of the femoral artery at 25 MHz. The phase velocity was in the expected range for tissue.	128
5.7	Impedance results for the medial layer. The impedance is in the expected range for tissue and was similar for the four regions.	129

5.8	Impedance results for the adventitial layer at 25 MHz. The impedance is in the expected range for tissue.	130
5.9	Fitted attenuation of the medial layer.	131
5.10	Fitted attenuation of the adventitial layer. The attenuation in the adventitia was higher than the media.	132
5.11	Backscatter coefficient of the medial layer in the femoral artery. Compared to the literature (7.6 (m Sr)^{-1}) the values are low.	133
5.12	Frequency spectra of the backscatter region in the medial layer, normalized against the spectra of the reference reflection for a representative data point in sample <i>2a</i> . The slope is not smooth, since the noise contributes to backscatter signal, and ultimately affects the slope of the backscatter coefficient.	134
5.13	Backscatter coefficient of the adventitia layer for the <i>2a</i> region. The result is low compared to the literature value (30 (m Sr)^{-1} at 25 MHz).	135

Chapter 1

Introduction

A scanning acoustic microscope (SAM) has been developed to measure the impedance, attenuation, phase velocity and backscatter coefficient for planar homogeneous materials over a range of high frequencies (10-40 MHz). The goal for the SAM is to determine what acoustic properties can be used to distinguish between different types of plaque on coronary arteries. Plaque is typically divided into two types: stable and vulnerable. Stable plaque leads to hardening of the artery wall and narrowing of the bloodstream, and the complications from these conditions are generally non-fatal. Vulnerable plaque has a high likelihood of rupture and is thought to be responsible for two-thirds of heart attacks and strokes. If detected, the presence of vulnerable plaque indicates a direction interventional approach. Although plaque can be detected by many modalities, currently there is no imaging modality that can successfully distinguish between stable and vulnerable plaque.

One modality that has been successful at detecting plaque is intravascular ultrasound

(IVUS). Current clinical devices use 10-40 MHz ultrasound to image the arterial layers from inside the artery. There have been some studies that indicate differences in acoustic properties between stable and vulnerable plaque, but most of these studies employ heuristic signal processing algorithms to either the enveloped or radio frequency (RF) data streams. There are few studies that have measured the acoustic properties of arterial walls and plaque deposits. The rationale for developing the SAM is to provide an instrument that can measure all the relevant acoustic properties and from that ascertain the underlying physical properties that can be used to distinguish different types of plaque.

1.1 The human artery

The human artery wall consists of three main layers, shown in Fig. 1.1. The passage in

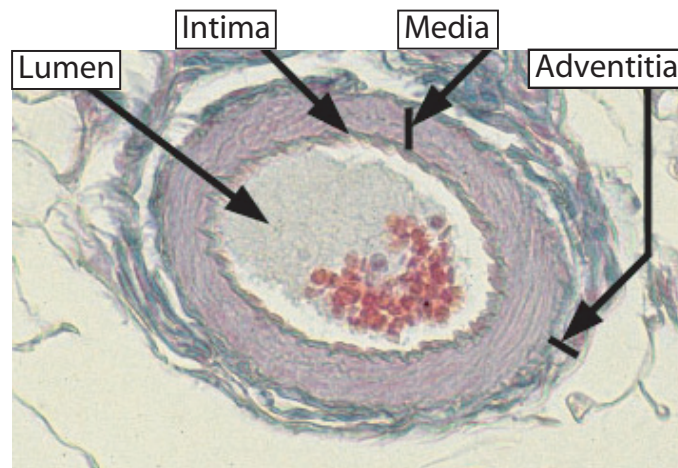


Figure 1.1: Human coronary artery. The blood travels through the lumen, in the center. The intima, media and adventitia make up the three main layers of the artery wall. *Photos courtesy of Cormack [12].*

which the blood travels is referred to as the lumen, and the outer diameter of the artery ranges from 1 cm to 0.50 mm. The innermost layer of the artery is the intima and is the thinnest of the three layers. A healthy intima is only a few cell layers in thickness (10-50 μm) and, due to its size, is hard to distinguish from the other layers using ultrasound. The intima is constructed of elastic tissue and endothelium cells. The middle layer of the artery is the media and, when healthy, ranges from 125 to 350 μm in thickness. The adventitia is the outer layer of the artery and has a thickness of 100-500 μm . In diseased arteries, plaque deposits form within the intimal layer, thickening the layer and making it more reflective to the ultrasound pulse. The medial layer will shrink and will vary from 16 to 190 μm in thickness [13, 23, 24, 35, 36].

The composition of the artery differs based on its type and position within the body. Due to the proximity to the highest systolic pressure from the heart, the arteries closest to the heart are the most elastic and become more muscular with increasing distance from the heart. The femoral artery is larger, more muscular and therefore has a higher percentage of collagen. The carotid artery is thinner and more elastic, containing a higher percentage of elastin. The individual roles of the elastin and collagen with respect to the scattering and echogenicity of the artery layers is unclear [20, 23, 24, 35] and will not be addressed in this study.

1.1.1 Plaque types

The presence of stable plaque is fairly common in most adults, especially in developed countries. The steps leading to the formation of plaque are thought to be related to the concentration of high and low-density cholesterol (HDL, LDL) in the blood. Plaques form when lipids (cholesterol and cholesterol esters) are deposited on the artery wall. When the plaque is homogeneous it is said to be stable. However, vulnerable plaque is thought to be formed when the lipid concentration is high enough to form pools. Macrophages, which are responsible for cellular breakdown and disposal, attempt to break down the lipid pools and in the process creates a fibrous, calcified cap over the lipid pool. Where the fibrous cap is thin the plaque is unstable and becomes susceptible to rupture: the cap deteriorates and breaks open, releasing a mixture of the lipids and related by-products of the macrophage breakdown into the blood stream. Such a mixture can act as a coagulant, which can block the blood vessel and trigger a heart attack or stroke [13]. The difference between the two types of plaque is shown in Fig. 1.2. The vulnerable plaque is distinguished by the concentration of the lipids under the thin fibrous cap, whereas the stable plaque appears to be homogeneous throughout. Thus far, the only way to accurately differentiate between stable and unstable plaque is through histology. Therefore there is a need to develop an imaging modality that can distinguish between plaque types so that the appropriate treatment can be applied.

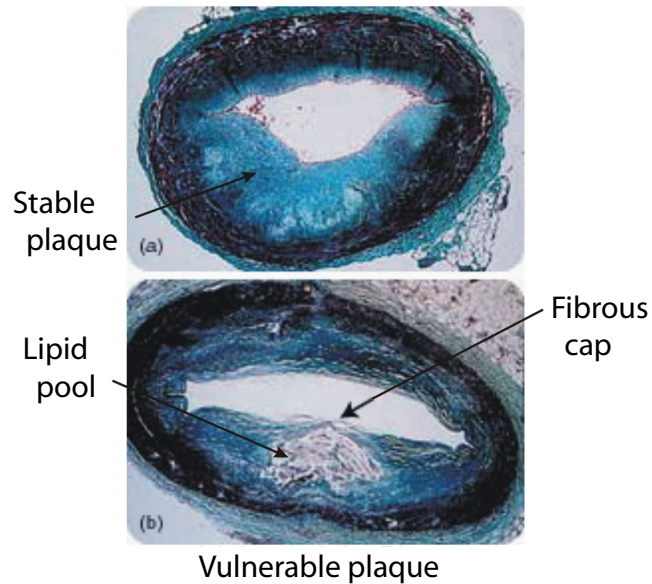


Figure 1.2: Histological comparison of (a) stable and (b) unstable plaque. The stable plaque consists of a large fibrous structure on the inside of the artery. The unstable plaque is distinguished by a lipid pool covered by a thin fibrous cap. *Photos courtesy of CIMIT.*

1.2 Detection techniques

There are a number of modalities used to inspect the artery wall for the detection of plaque. The current ‘gold standard’ in the medical community for detection of plaque is coronary angiography. Coronary angiography uses contrast agents to aid X-ray imaging in the examination of the blood flow and a measurement of the arterial diameter is obtained from a two-dimensional silhouette. Different regions of the blood vessel are compared, where the more narrow regions suggest a thickening of the artery wall and the presence of plaque. The drawbacks to coronary angiography are the success rate and the information about the plaque which is provided by the technique. Studies have shown that angiography under-

estimates the presence of plaque and the composition of the plaque cannot be determined [18, 39].

Another modality which has been investigated is coronary angiography, which uses fiber optics to optically image the artery wall. This modality provides an excellent picture of the surface of the plaque but since light cannot effectively penetrate the plaque an accurate risk assessment cannot be provided. In addition the operation of the measurement requires that the lumen be blocked and flushed with saline solution to obtain a clear picture. Several complications can arise when the bloodstream is blocked for this procedure, including coronary rupture, dissection and thrombosis [39, 63].

A newer experimental modality is optical coherence tomography (OCT). OCT is an imaging modality capable of obtaining cross-sectional images of coronary vessels at a resolution of approximately $10\ \mu\text{m}$. The method is based on low-coherence interferometry, a technique where the beam from some continuous-wave light source, such as an infrared low-coherence diode or laser, is split in half. Half the beam travels to and from the sample and half is sent to a reference mirror, and the coherence of the two beams can be provide time-of-flight information about the sample structure. Thus, an image of the plaque can be created by mapping the backscattered light as a function of the delay time in the reflection. The resolution of the image is good and studies have shown success with identification of plaque indicators. However, the modality suffers from scattering of the light by the blood, which requires a similar flushing technique to angiography. The technique also has a slow data acquisition rate which does not allow long segments of the artery to be scanned. One

tradeoff of the high resolution is a low penetration depth (2 mm) into the artery [4, 29, 32].

IVUS systems are the only clinically-approved modality which interact mechanically with the artery wall. The basic system consists of a side-looking ultrasound probe which is mounted to the end of a catheter which can be inserted into the blood vessel. The probe operates in pulse-echo mode, as it sends an ultrasound pulse in the radial direction and receives backscattered signals from the structures within the arterial walls. Penetration of the pulse into the wall depends on the frequency of the probe and position of the probe relative to the artery wall. The wavelength decreases with an increase in frequency, which improves the resolution of the system and allows smaller structures to be detected. However, the tradeoff is that absorption in both blood and tissue increases with increase in frequency. Therefore the depth of penetration of the ultrasound into the tissue decreases with frequency [15, 39].

Figure 1.3 shows an image of a cylindrical tissue-mimicking phantom taken with a Boston Scientific Galaxy IVUS system. The probe consisted of a 40 MHz single-element unfocused transducer (3F). The transducer is rotated at 30 Hz and returns a real-time image of the artery wall. The bright ring in the center is the reflection from the thin sheath which surrounded the probe. The dark regions out to approximately 2.5 mm is the lumen of the phantom that was filled with water. The phantom shown here was gelatin and agar-based with carborundum particles. The tissue phantom appears as speckle and for this phantom the IVUS system could see approximately 6 mm into the phantom.

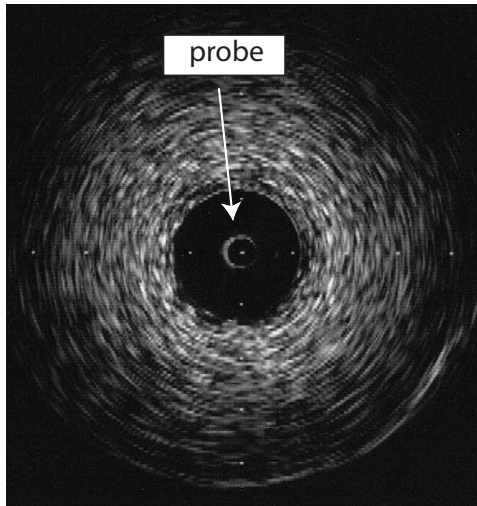


Figure 1.3: IVUS image of a tissue-mimicking phantom. The bright ring in the center of the phantom is the sheath which contained the transducer. The white markers are at 2 mm spacing. The ultrasound pulse penetrated approximately 6 mm through the phantom.

1.2.1 IVUS measurements

Many studies have been performed to investigate the feasibility of using IVUS to detect plaque types as well as the individual layers of the artery. In two separate studies, Lockwood et al [35, 36] used a SAM and an IVUS system to make *in vitro* measurements of healthy and diseased femoral and carotid arteries over a 35-65 MHz range in the radial and axial orientation. The measurements were analyzed for the attenuation, sound speed and backscatter coefficient and histology was performed to examine the results. The sound speed and attenuation results were averaged since the measurement setup did not allow for analysis of individual layers but the backscatter coefficient was determined for the healthy and fibrous intima, as well as for the media and adventitia. The backscatter coefficient, which will be described in greater detail in Sec. 1.3.1, is a measurement of how much of

the signal is scattered by the material. The scattering was determined to be dependent of the layer, and the healthy and thickened intimal layers displayed a wide variation. The results from the SAM and IVUS systems were in good agreement. In particular, the adventitia was observed to have the highest level of scattering among the tissue layers, and the measurements in the radial orientation resulted in higher backscatter than the axial.

Urbani et al [65] used a 7.5 MHz IVUS system to perform *in vivo* measurements in carotid arteries. The measurements were analyzed for identification of fatty, fibrous, calcified and intraluminal thrombotic sites using the integrated backscatter index (IBC), the integrated amplitude of the rectified radiofrequency signal. The IBC, which is measured in decibels, is determined from the ratio of the backscatter signal from the sample and a reference signal. The patients were undergoing carotid thromboendarterectomy, so histology was performed to match the results with pathology. The fatty, fibrous and calcified regions had distinct values for the IBC while the intraluminal thrombotic regions were similar in value to the fatty sites. Spencer et al [59] performed *in vitro* measurements on coronary arteries using an IVUS system with a 17-42 MHz range. Histology confirmed the detection of loose fibrotic tissue, dense fibrotic tissue and calcified regions using the maximum power and spectral slope of the signal (normalized for the IVUS system characteristics in the frequency-domain) as indicators of the region. Bridal et al [5] used the attenuation, attenuation slope and integrated backscatter to identify *in vitro* healthy and diseased tissue in the aortae while Saijo et al [57] relied on the attenuation slope and the sound speed to differentiate between healthy, calcified, fibrotic and fatty sites on the intima in conjunc-

Table 1.1: Literature results for the backscatter coefficient $[(\text{m Sr})^{-1}]$ of the human artery

Group	Artery	Frequency [MHz]	Diseased intima	Media	Adventitia
Lockwood (1991)	Femoral	50	7.0	20	80
Lockwood (1991)	Carotid	50	80	400	200
Machado (2001)	Carotid	50	20	4.0	20

tion with histology. The integrated backscatter, also referred to as the apparent integrated backscatter (i.e., not corrected for attenuation effects of the signal), is the square of the pressure response in the frequency domain, corrected for the characteristics of the transducer, yielding a power spectrum.

While techniques such as the power and spectral slope of the signal have been shown to identify different constituents of the tissue, backscatter measurements have the advantage of identifying not only the constituents on the intima surface but the individual layers of the arteries as well. The literature values for the backscatter coefficients of the tissue layers are compiled in Table 1.1. The literature results of the average attenuation and average sound speed of the artery are compiled in Table 1.2. Further reporting on properties comes from Greenleaf et al [22], as compiled by Goss et al [21], D’Astous et al [14], and Machado et al [38]. Hence, we decided to focus on setting up the data acquisition and analysis for the SAM to measure the backscatter coefficient.

1.3 Measurements for SAM

The ultimate goal for the SAM is to measure all the relevant acoustic properties for differentiating between stable and vulnerable and thus provide a physical basis for delineating plaque types using IVUS. This goal was beyond the scope of this thesis but the components necessary to make those measurements have been implemented in the SAM. First, the measurements of the impedance, attenuation and sound speed were validated both with the time causal model and literature values. The focal region and angle which the transducer can be tilted in respect to the flat sample were examined by comparing the change of the impedance, attenuation and sound speed over a range of distances and angles from the transducer. Secondly we measured the backscatter coefficient. A third goal was the development and characterization of a set of recipes for tissue phantoms which could provide control over the acoustic properties depending on the constituents of the recipe. These phantoms were designed for characterization by the SAM but also for use in an IVUS system.

Table 1.2: Literature results for the human artery (healthy)

Group	Tissue	Frequency [MHz]	α [dB/cm]	c [m/s]
Greenleaf, 1974	Aorta	10	6.1	1501
D'Astous, 1986	Breast	5	5.0	–
Lockwood, 1991	Femoral	30	40	1579-1628
Lockwood, 1991	Carotid	30	40	1579-1628
Bridal, 1997	Carotid	37.5	52-76	–

1.3.1 The backscatter coefficient

The BC is used to characterize the way in which a material scatters energy from a sound wave. The BC is defined as the differential scattering cross section per unit volume at a scattering angle of 180° . The differential backscatter cross-section, which is equivalent to an intensity reflection coefficient for a single scatterer, is a measurement of the power scattered by an object as a function of the unit solid angle [52]. The units for the BC are $(\text{m Sr})^{-1}$, where the Steradian is the unit of solid angle measurement. The BC characterizes the presence of subwavelength scatterers in a medium, which are too small to be resolved independently but still generate an echo signal [7, 10, 41].

There has been much work and development in the area of characterizing the BC, resulting in several formulations on how to accurately measure and report the BC. Early work on the subject concentrated on underwater applications, and a seminal paper by Faran in 1951 [19] describes theory and measurements on the scattering of longitudinal and shear waves based on the elastic properties of the scatterers. Faran used isotropic cylinders and spheres as the scatterers and the Faran theory has been used as a basis for much of the work on scattering since it provides a theoretical model for the distribution in angle of pressure for a wave reflected from a scatterer. Sigelmann and Reid [58] looked at the backscatter from an ensemble of scatterers, and came up with a method for determining the pressure and backscatter coefficient from multiple scatterers. Their measurement of the backscatter coefficient was determined from the ratio of the power scattered from the sample to the power reflected from a standard planar reflector, based on a pulse-echo system. This

method is referred to as the substitution method, since the calibration for the transducer, the electronics and miscellaneous effects of the system is accounted for ‘by substitution’ of the sample by a flat, highly-reflecting reference plate.

While the AIUM recommended the Sigelmann-Reid substitution method for determining the backscatter coefficient, the theory assumes a uniform pressure response from a flat transducer. Much of the research for scattering employs a focused or beamformed transducer, so correcting for the transducer effects has been subject of much debate [7, 41]. The more tightly focused the transducer, the greater the diffraction effects on the beam, so accounting for the diffraction is an important part of the theory if the backscatter is to be determined from the bulk parameters. Hence, other groups have used the Sigelmann and Reid method as a basis for the backscatter coefficient but have adapted it to different setups and developed advanced formulations.

The Madsen model [41] differs from the Sigelmann and Reid formulation in respect to the area of the volume of the sample which is interrogated, as well as the time gating applied to the received signal. The method is adapted for both narrowband and broadband pulses and agrees well with the Faran model but not as well for the Sigelmann and Reid values of the backscatter coefficient. This formulation also uses a planar reflector for the reference signal. The Madsen formulation was tested for multiple scatterers using well-characterized phantoms [10] and results matched up well with the Faran theoretical model.

Yao, Zagzebski and Madsen [69] have a reference phantom technique for array transducer setups, which allow larger regions to be scanned. The novel component of Yao’s

analysis is the use of a well-characterized tissue phantom for the reference signal, instead of a planar reflector. Analysis of the backscatter coefficient of the reference phantom comes from a theoretical analysis from the Faran formulation. The reference phantom technique has since been used in other labs [43, 53].

An additional tool in looking at the backscatter coefficient is a correlation model such as the one developed by Insana and Hall [31] since the model yields an approximate value for the backscatter coefficient and the scatterer size. The model is based on knowledge of the scatterers (diameter, longitudinal sound speed, Poisson's ratio, number density) and uses two form factors to determine the scattering as a function of frequency. The first form factor is derived from the Faran scattering theory and the second models the scatterers as rigid spheres.

A formulation for the measurement of the absolute backscatter coefficient for the case of spherical transducers has been developed by Chen et al [8]. The Chen model explicitly accounts for the diffraction for the flat disk and spherically focused transducer cases. For a flat transducer the Madsen formulation is recovered when the gating restrictions on the signal are lifted. The Sigelmann and Reid formulation is recovered for the flat transducer case. The diffraction correction was validated by Machado and Foster [37] and has been used in numerous studies since its publication [24, 45, 44, 53, 17]. In this work the Chen method was used to determine the backscatter coefficient and a full description of the Chen method is presented in Section 2.3.

1.3.2 Tissue Phantom

The past two decades have seen much progress in the development of tissue mimicking phantoms for ultrasonic use, particularly for the low megahertz range. Most phantoms use an agar or gelatin base with a fine scattering particles to simulate the attenuation and backscatter of tissue.

Four sources were used in the development of the SAM phantoms and the principal component used in the recipes are presented in Table 1.3. Madsen et al. [40] developed an ultrasound phantom which mimicked the attenuation and sound speed properties of human tissue. The recipe was based on gelatin, graphite powder, alcohol and water. The attenuation was controlled by the graphite concentration and the sound speed was varied by the concentration of alcohol. Madsen reported a variation in the attenuation of 0.2-1.5 dB/cm at 1 MHz and a range of 1520-1650 m/s for the sound speed. Burlew et al. [6] built upon the Madsen phantom recipe but used agar in place of gelatin in order for the phantom to be more stable and better able to withstand higher temperatures. Again attenuation could be controlled with the graphite concentration and sound speed with the propanol concentration.

Table 1.3: Phantom Recipes by Percent Concentration

Group	Gelatin	Agar	Scatterer	Propanol	Water
Madsen	12-15	0	4.9-18.7	0-21	63.6-75
Ryan	15-30	0	2	0	68-83
Burlew	0	3	1.4-16.5	0-20	70.4-87
de Korte	8	1-3	0.5-2	0	87-90.5

Ryan and Foster [56] developed phantoms for use in an IVUS system. The recipe was tuned to produce either hard or soft tissue phantoms, which was controlled by the gelatin and water concentration. Silica (SiO_2) particles were used for the scattering. The soft (i.e., less stiff) phantom ranged in sound speed from 1532-1558 m/s and the hard (i.e., less compressible) phantom ranged from 1586-1614 m/s. Over a 29-55 MHz range, the attenuation ranged from 19-48 dB/cm and 39-91 dB/cm for the soft and hard phantoms, respectively. The backscatter coefficient ranged from approximately 1-6 $(\text{m Sr})^{-1}$ for the soft material and 0.4-3 $(\text{m Sr})^{-1}$ for the hard material over the 29-55 MHz range. ¹

The main issues relating to the acoustics behind the identification of atherosclerotic plaques have been described, as pertains to using an IVUS system as a diagnostic tool. The phase velocity, impedance, attenuation and backscatter coefficient have been shown to be identifying properties of human tissue and tissue plaques, so the challenge remains to develop a laboratory tool such as the SAM which can measure such properties for verification with IVUS measurements. The development of the SAM includes the derivation of the necessary acoustic theory behind the measurements as well as validation of the measurements against published values. In order to test the ability of the SAM to measure materials acoustically similar to human tissue, a set of tissue-mimicking phantom recipes was developed, and the effect of the respective concentration of the ingredients on the acoustic properties was

¹de Korte et al [33] developed a phantom for use in the IVUS which was multilayered to achieve the effect of lesions in the tissue. Varying concentrations of agar, gelatin and water were used to make soft and hard layers within the phantom. Carborundum (SiC) particles were used to mimic the scattering and attenuation. These phantoms were measured for elastic properties, but the acoustic properties were unreported.

studied. Finally, an initial feasibility study on *in vitro* human arteries was conducted. The acoustic theory is presented in Ch. 2 and the experimental setup and validation of the phase velocity, impedance and attenuation measurements are presented in Ch. 3. The tissue phantom study is presented in Ch. 4 and the tissue study on *in vitro* human arteries is shown in Ch. 5.

Chapter 2

Theory of Measurements

The SAM is an experimental instrument designed to measure the phase velocity, impedance, attenuation and backscatter coefficient of a homogeneous material. The system consists of a focused ultrasound transducer operating in pulse-echo mode which is placed in a water bath and scanned in a horizontal plane over the sample. The analysis used to recover the acoustic properties of the sample assumed that the waves passing through the sample could be approximated as plane waves. This approximation required the sample volume to be in the focal region and have parallel planar surfaces perpendicular to the propagation path.

In this chapter the model used to extract the material properties from the acoustic measurement is described. The validity of the plane wave approximation was tested by varying sample position and angle throughout the near and far field regions of the transducer and is presented in Section 3.5.

2.1 Pulse Measurements

The following analysis for the phase velocity and sound attenuation stems from a plane-wave analysis of the three pulses shown in Fig. 2.1. The sample was measured by transmitting a

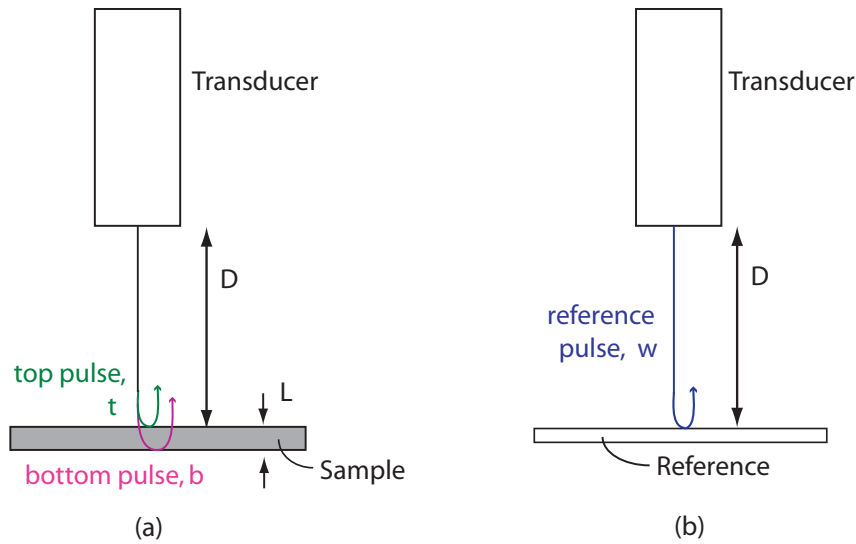


Figure 2.1: The measurement for the phase velocity and attenuation: (a) the sample measurement consisted of a pulse reflected from the top surface and a pulse reflected from the bottom surface of the sample. (b) The reference measurement consisted of a pulse reflected from the top surface of the reference material. The top surfaces of the sample and the reference were positioned a distance D from the transducer surface.

pulse and measuring the echoes from the top and bottom surfaces: the first measurement was of the reflection off the top of the sample, $p_t(t)$, and the second measurement, $p_b(t)$, was of the reflection from the interface of the bottom of the sample and its backing (either water or glass). A second pulse $p_w(t)$, shown in Fig. 2.1(b), was a measurement of the reflection from the top surface of a reference material. A glass slide was used as the reference material. As long as the positioning of the sample and the water path were the same, only one reference data set was required and could be used for the analysis of all the samples. The parameter

Table 2.1: Coefficients for speed of sound in water [16]

i	k
0	1402.387
1	5.037
2	-5.808×10^{-2}
3	3.34×10^{-4}
4	-1.478×10^{-6}
5	3.146×10^{-9}

D was the distance to the top of the reference and sample and L was the thickness of the sample; these metrics were measured prior to the analysis.

The speed of sound in water fluctuates depending on the temperature and can be determined from a fifth order fit [16]

$$c_{water} = \sum k_i T^i \quad (2.1)$$

where T is the temperature in $^{\circ}C$ and the coefficient k_i is determined from Table 2.1.

For a laboratory temperature of $23^{\circ} \pm 3^{\circ} C$, the sound speed of water was determined to be 1491 ± 8 m/s, a deviation of $< 1\%$. Due to this small variation, the sound speed used in our analysis was taken to be 1491 m/s. This sound speed corresponds to a density of 1000 kg/m^3 and a specific acoustic impedance of 1.49 MRayls. The specific acoustic impedance of the reference medium was based on the manufacturer's value of the density and the sound speed, which was measured using a through-transmission setup, presented in Section 3.2. All other properties were assumed to be unknown.

The pulses were acquired in the time domain and analyzed in the frequency domain. The attenuation and dispersion in the phase velocity were frequency-dependent properties

for the samples measured with the SAM, so the pulses were transformed to the frequency domain for the analysis. In order to go from the time domain to the frequency domain, a Fourier transform, denoted as \mathcal{F}_{-i} , was performed on each pulse, resulting in $P_t(f)$, $P_b(f)$ and $P_w(f)$.

$$\mathcal{F}_{-i}[p_t(t)] = P_t(f) = A_t(f)e^{i\theta_t(f)} \quad (2.2)$$

The amplitude of the pulse was $A_t(f)$ and $\theta_t(f)$ was the phase of the wave. Practically, the operation was implemented in MATLAB by performing a fast Fourier transform (FFT) after a Hamming window was applied to the signal in the time domain.

For the measurement of the reflection from the top surface, the pulse was emitted by the transducer and propagated through the water until it was incident on the front surface of the sample. We assumed the pulse was a plane wave at the proximal interface and that it had a complex pressure amplitude $P_0(f)$. The plane wave assumption allowed us to simplify our expression for the impedance, and it should be noted that hereafter the term ‘impedance’ will refer to the ‘specific acoustic impedance’. This pressure accounted for the electrical excitation pulse, the transducer impulse response and propagation through the water to the sample. The propagation included attenuation and diffraction effects of the pulse. At the interface the signal was partially reflected and partially transmitted; the amplitude of the pulse which was reflected was the plane wave pressure-amplitude reflection coefficient, R . The reflection coefficient for a plane wave normally incident on a plane surface is given by

$$R_{ij} = \frac{Z_j - Z_i}{Z_i + Z_j} \quad (2.3)$$

where Z is the impedance and i refers to the first medium and j refers to the second medium.

The acoustical impedance is defined in terms of the density ρ and the phase velocity $c_i(f)$:

$$Z_i(f) = \rho_i c_i(f) \quad (2.4)$$

After reflecting off the sample the pulse propagated back to the transducer through the water. The reflection off the top surface of the sample was

$$P_t(f) = P_0(f)R_{ws}E(f) \quad (2.5)$$

where w and s indicated the water and sample mediums, respectively. $E(f)$ represents the echo response of the pulse from the sample to the transducer, which includes the electrical conversion of the echo from a pressure to a voltage.

The path which the pulse took to reflect off the back of the sample was slightly longer since there were more boundaries. As in the case for $p_t(t)$, the transducer emitted a pulse which traveled through the water to the top surface of the sample. At the top surface of the sample the pulse was partially transmitted into the sample with the pressure transmission coefficient, T_{ws} . For a normally incident pulse, the transmission coefficient was:

$$T_{ij} = \frac{2Z_j}{Z_i + Z_j} \quad (2.6)$$

The pulse continued traveling away from the transducer through the sample until it reached the back surface of the sample. At this interface the pulse was again partially reflected and partially transmitted through the surface. The reflection back through the sample, R_{sr} , can be determined from Eq. 2.3 and the amplitude depended on the impedance of the backing material. Glass was used as the backing for the phantom samples, but water was the backing medium for all of the other samples. Since the medium changed, the backing

medium was referred to as r , the reference medium. Reversing direction, the pulse traveled back through the sample and encountered the interface of the top surface and the water again. The amplitude of the pulse transmitted through the top surface of the sample was T_{sw} . The signal was received by the transducer after it propagated by the distance D through the water to the transducer surface. The reflection of the pulse off the back of the sample was

$$P_b(f) = P_0(f)T_{ws}R_{sr}e^{ik_s(f)-\alpha_s(f)2L}T_{sw}E(f) \quad (2.7)$$

The wave number $k_s(f)$ and attenuation $\alpha_s(f)$ were the same traveling down and back through the sample.

The measurement from the reference medium was similar to the measurement of the reflection off the top surface of the sample, so the only difference in the equation was the reflection coefficient. The top surface of the reference was placed in the same position as the sample's top surface, so that the surface was a distance D from the transducer surface. The pulse was emitted from the transducer and propagated through the water until it encountered the top surface of the reference. The pulse was partially reflected back towards the transducer and traveled the same distance back to the transducer. The amplitude of the reflection was R_{wg} , where g was the glass reference medium.

$$P_w(f) = P_0(f)R_{wg}E(f) \quad (2.8)$$

2.1.1 Phase Velocity

With the three pulses defined, the phase velocity, attenuation and impedance can be determined. Since the reflection and transmission coefficients are real, the phase velocity can be recovered from the phase angles of the top and bottom pulses. The difference in phase angles is recovered by taking the complex argument of Eqs. 2.5 and 2.7. The difference in the phase angles of the top and bottom pulses is

$$\theta_t(f) - \theta_b(f) = 2k_s(f)L \quad (2.9)$$

The wave number $k(f)$ contains the phase velocity $c_s(f)$

$$k_s(f) = \frac{2\pi f}{c_s(f)} \quad (2.10)$$

so combining Eqs. 2.9 and 2.10 provides the phase velocity:

$$c_s(f) = \frac{4\pi fL}{\theta_t(f) - \theta_b(f)} \quad (2.11)$$

An important consideration in the calculation of the phase velocity is the impedance of the reference medium which backs the sample. If $Z_r < Z_s$ then there is a 180° phase shift which is introduced; to accommodate the phase shift a factor of π is subtracted from $\theta_b(f)$.

Note that the phase spectrum returned by the FFT algorithm is restricted to a range of $-\pi$ to π but for the materials measured in the SAM, the phase difference should decrease with frequency. In order to properly recover the phase velocity in Eq. 2.11 a routine must be employed to ‘unwrap’ the phase over the frequency range. A phase unwrap function exists in MATLAB which unwraps the phase based on a tolerance for the jump, normally

by intervals of π . However, this function did not work for the SAM since the phase jumped by multiple intervals so a separate routine was written to unwrap the phase (see Appendix A). The routine was implemented by inspecting θ over the frequency range and every time the angle at the next frequency increased by $\pi/2$ over the current value 2π was subtracted from θ over the rest of the frequency range. The phase velocity for the samples measured with the SAM, due to slight dispersion effects, should be nearly linear with frequency, so the phase should decrease smoothly with frequency. Fig. 2.2 illustrates the difference between the MATLAB and SAM unwrapping routines; the two routines were used to unwrap the

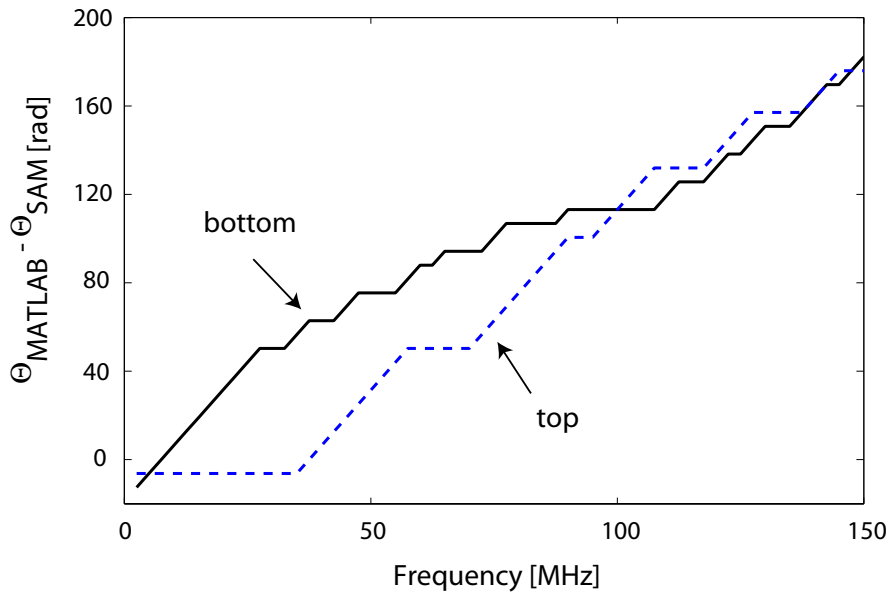


Figure 2.2: The respective difference in the phase angle of the top and bottom surface echoes treated by the MATLAB and SAM unwrapping routines: the slopes should be flat, and the increases show where the MATLAB routine did not correct for the unwrapping.

phase angle of the reflection from the top and bottom surfaces for the same data set and the respective difference of the two results was plotted. If both routines unwrapped the phase

properly the slope would be flat, and the lines increase whenever the MATLAB routine did not unwrap the phase correctly.

2.1.2 Specific Acoustic Impedance

The impedance of the test sample was found from the amplitude of the top pulse since the impedance of the sample was contained in the expression for the reflection coefficient. The pressure amplitude $P_0(f)$ and the exponential terms in Eqs. 2.5 and 2.8 were the same, so dividing the magnitude of the two expressions provided a ratio of the reflection coefficients:

$$\frac{|P_t(f)|}{|P_w(f)|} = \frac{R_{ws}(f)}{R_{wg}} \quad (2.12)$$

The reflection coefficient for the glass reference R_{wg} was known, so $R_{ws}(f)$ could be isolated and the impedance Z_s of the sample was

$$R_{ws}(f) = R_{wg} \frac{|P_t(f)|}{|P_w(f)|} \quad (2.13)$$

$$R_{ws}(f) = \frac{Z_s - Z_w}{Z_w + Z_s} \quad (2.14)$$

$$Z_s(f) = Z_w \frac{1 - R_{ws}(f)}{1 + R_{ws}(f)} \quad (2.15)$$

2.1.3 Attenuation

We derived the expression for the attenuation as

$$\alpha_s(f) = \frac{1}{2L} \ln \left(\frac{|P_t| |T_{ws} R_{sr} T_{sw}|}{|P_b| |R_{ws}|} \right) \quad (2.16)$$

The attenuation could be determined by taking the ratio of the top and bottom pulses and taking the real part of the exponential. With the impedance of the sample solved, the

transmission and reflection coefficients were determined from Eqs. 2.6 and 2.3, respectively.

$$\frac{|P_b|}{|P_t|} = \frac{T_{ws}R_{sr}T_{sw}e^{-2\alpha_s L}}{R_{ws}} \quad (2.17)$$

The calculation of R_{sr} changed depending on the sample. The formulation in Eq. 2.3 holds true for all cases where the impedance in medium j was greater than medium i , and was used when glass backed the phantoms. However, a 180° phase shift was introduced when $Z_i > Z_j$, so R_{ij} changed by a negative sign:

$$R_{ij} = \frac{Z_i - Z_j}{Z_i + Z_j} \quad (2.18)$$

This situation arose when water was used as the backing of the sample, as was the case for the polyethylene samples, since the impedance of polyethylene is higher than that of water.

2.2 Time Causal Model

In the experimental measurements the phase speed and attenuation were measured independently, however causality requires that phase speed and attenuation are not independent properties but are connected. The causality requirement is that every action must be preceded by its cause, and is often expressed in the frequency domain using the Kramers-Kronig relations. In this work we use a formulation derived by Szabo [61] in the time domain. Szabo showed that for a medium where the attenuation follows the power law $\alpha = \alpha_1 f^y$ and for $y \neq 1$, causality requires that the phase speed is

$$\frac{1}{c(\omega)} = \frac{1}{c(\omega_0)} + \alpha_1 \tan \frac{\pi y}{2} [|\omega|^{(y-1)} - |\omega_0|^{(y-1)}] \quad (2.19)$$

where ω_0 is the center frequency. In the event that $y = 1$, the phase velocity is

$$\frac{1}{c(\omega)} = \frac{1}{c(\omega_0)} - \frac{2\alpha_1(\ln |\omega| - \ln |\omega_0|)}{\pi} \quad (2.20)$$

These relationships were derived in the time-domain but were transformed and applied in the frequency-domain and has been shown to be analogous to the Kramers-Kronig relations in the frequency domain [61].

For all our measurements we assumed that the attenuation can be adequately modelled by a power law:

$$\alpha(f) = \alpha_1 |f|^y \quad (2.21)$$

The unknown variables, the attenuation coefficient α_1 and the power law exponent y , are solved by employing the MATLAB minimization function, *fminsearch*, that fits the two terms to a least squares error routine using the calculated attenuation values. The time causal model was applied to all of the materials studied and was used to validate the phase velocity and attenuation measurements.

2.3 Backscatter Coefficient

Once the phase velocity and attenuation are known, the backscatter coefficient (BC) can be determined, for materials with scattering properties. The BC characterizes the energy scattered in a material by measuring the differential backscatter cross-section of the scatterer per unit volume. The BC is of particular interest in tissue studies since it provides a statistical measurement of the scattering, which can provide a measure of the microstruc-

ture of the tissue. As discussed in Sec. 1.3.1, multiple formulations have been developed to describe the backscatter within a material. The Faran theory is useful for examining the scattering from a single sphere or cylinder and can be also used a basis for looking at multiple scatterers. Roberjot et al [54] measured a commercial phantom for the backscatter coefficient over a broad range of frequencies (2-60 MHz) in one of the few published results of high frequency (> 15 MHz) characterization of tissue phantoms for the backscatter coefficient. In order to validate their results, Roberjot compared experimental results with the Faran model and found good agreement. We had hoped to measure and compare our results to literature results and the model using an identical phantom but were unable to obtain the phantom in time to perform the measurements. Instead, we will present the model as a basis for single-particle scattering and future work if an identical phantom is obtained.

Faran's theory considers the farfield radiation of a single spherical elastic scatterer that has been insonified by a monochromatic plane wave. His expression for the pressure field radiated by a spherical scatter is

$$|P_s(\omega)| = \frac{P_0}{k_3 r} \left| \sum_{n=0}^{\infty} (2n+1) \sin \eta_n \exp(-i\eta_n) P_n(\cos \theta) \right| \quad (2.22)$$

where P_0 is the pressure amplitude from the transducer, a is the radius of the scatterer, k_3 is the wave number in the medium, r is the distance from the transducer to the scatterer, the summation is over all the spherical harmonics, η_n is related to the phase shift of the n th scattered harmonic, and P_n is the Legendre polynomial where θ is the angle between the source and the scattered wave. For the purposes of determining the backscatter coefficient only the scattered energy arriving to the source is needed, so for a pulse-echo setup, $\theta = 180^\circ$

and $\cos \theta = -1$.

The phase shift is given by

$$\tan \eta_n = \tan \delta_n(x_3) \frac{\tan \Phi_n + \tan \alpha_n(x_3)}{\tan \Phi_n + \tan \beta_n(x_3)} \quad (2.23)$$

where $x_i = k_i a$, $k_i = \omega/c_i$ is the wave number, $i = 1, 2, 3$, with c_1 and c_2 the longitudinal and shear wave speeds of the particle and c_3 the speed of sound in the surrounding medium.

The angle Φ_n comes from the boundary impedance:

$$\tan \Phi_n = -(\rho_3/\rho_1) \tan \zeta_n(x_1, \sigma) \quad (2.24)$$

The parameters ρ_3 and ρ_1 refer to the density of the medium and the scatterer, respectively.

The scattering phase angle $\tan \zeta_n(x_1, \sigma)$ is defined as:

$$\tan \zeta_n(x_1, \sigma) = -\frac{x_2^2}{2} \frac{\frac{\tan \alpha_n(x_1)}{\tan \alpha_n(x_1)+1} - \frac{n^2+n}{n^2+n-1-\frac{1}{2}x_2^2+\tan \alpha_n(x_2)}}{\frac{n^2+n-\frac{1}{2}x_2^2+2 \tan \alpha_n(x_1)}{\tan \alpha_n(x_1)+1} - \frac{(n^2+n)[\tan \alpha_n(x_2)+1]}{n^2+n-1-\frac{1}{2}x_2^2+\tan \alpha_n(x_2)}} \quad (2.25)$$

The intermediate angles needed to define the phase shift of the wave η_n and the scattering phase angle ζ_n are defined in terms of the spherical Bessel and Neumann functions $j_n(x_i)$ and $n_n(x_i)$ respectively, and are given as

$$\begin{aligned} \delta_n(x_i) &= \tan^{-1} [-j_n(x_i)/n_n(x_i)], \\ \alpha_n(x_i) &= \tan^{-1} [-x_i j_n'(x_i)/j_n(x_i)], \\ \beta_n(x_i) &= \tan^{-1} [-x_i n_n'(x_i)/n_n(x_i)] \end{aligned} \quad (2.26)$$

The scattering amplitude function $\Phi_s(\omega)$ is given by

$$\Phi_s(\omega, a) = \frac{r \cdot P_s(\omega, a)}{P_0(\omega)} \quad (2.27)$$

Table 2.2: Roberjot phantom properties

Material	Diameter [μm]	Density [kg/m^3]	Poisson's ratio	Longitudinal velocity [m/s]	No. density [beads/ m^3]
bead	82	2500	0.16	5400	10^{10}
bead	4	2500	0.16	5400	1.27×10^{15}
medium	–	1000	–	1541	–

where r accounts for the spherical spreading of the scattered wave. The differential backscatter cross-section is given by

$$\sigma_d(\omega) = |\Phi_s|^2 \quad (2.28)$$

The theoretical backscatter coefficient $\eta_{th}(\omega)$ for an ensemble of scatterers is found by multiplying the differential backscatter cross section by the number of particles per unit volume N_s :

$$\eta_{th}(\omega) = N_s \sigma_d \quad (2.29)$$

Therefore, based on the knowledge of the elastic parameters of the scatterers and their surrounding medium, the backscatter coefficient can be determined. We show an example by using the parameters employed by Roberjot [54] for a medium with scatterers that are either $4 \mu\text{m}$, $82 \mu\text{m}$ or a mixture of the two diameters. For the $4 \mu\text{m}$ diameter beads only the backscatter coefficient displays a power law dependence on the frequency of f^4 throughout the entire frequency range; this is classic behavior for the case of scattering from particles that are much smaller than a wavelength and is referred to as Rayleigh scattering. The larger $82 \mu\text{m}$ diameter beads exhibit a similar power law dependence, but only for a lower range, of frequencies, where $k_3 a \ll 1$. From approximately 6-25 MHz ($k_3 a = 0.3$) the backscatter

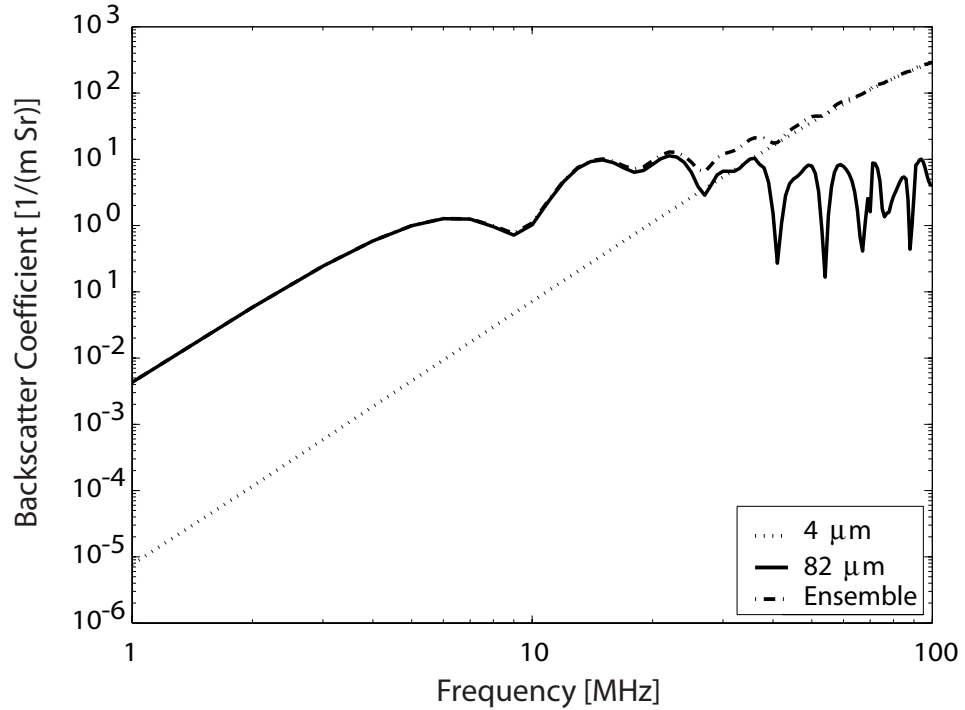


Figure 2.3: The theoretical backscatter coefficient for the $4 \mu\text{m}$, $82 \mu\text{m}$ diameter beads (dotted and solid lines, respectively) and for the combined effect of the two beads, shown in the dashed-dotted line. The bead density was 1.27×10^{15} beads/ m^3 for the $4 \mu\text{m}$ diameter beads and was 10^{10} beads/ m^3 for the larger $82 \mu\text{m}$ diameter beads.

coefficient for the larger bead exhibits multiple oscillations due to the interaction of the surface waves with the reflected wave. Above 25 MHz the internal resonances dominate the response from the larger beads. Note that the beads still scatter strongly just no longer as well as the backward direction. For a medium with both beads the backscatter coefficient is given by the sum of the two individual backscatter coefficients. The backscatter coefficient for the ensemble follows the curve of the larger bead until 20 MHz, where the backscatter coefficient for the two beads converge, and after 50 MHz, increases with an f^4 dependence, as the backscattering from the smaller objects dominates. It is important to note the effect of

the number density of the beads: Eq. 2.29 shows that the theoretical backscatter coefficient is linearly-dependent on the number density, so the 10^5 beads/m³ difference between the two bead populations increases the theoretical backscatter coefficient for the smaller beads to the same level as the larger beads in the 20-40 MHz range.

The analysis used in the SAM was adapted from the theory for the BC in the case of a spherically-focused transducer by Chen et al. [8]. The pertinent expressions are reproduced here; for the full treatment of the derivation, see the paper by Chen et al.

The measurement consists of the signal captured from the reflected wave off a sample, which contains some amount of scattering particles, and the reflected signal off a known reference surface (in this study glass was used as the reference material). Scattering inside a material can be seen in the signal after the reflection from the top surface, as shown in Fig. 2.4. The sample on the left is HDPE, which has no scatterers, while the sample on the right is a phantom which has 10% silica scattering particles. Since the HDPE has a higher amplitude the voltage scale was different for the two measurements, so the apparent clipping of the signal in the water and in the phantom is due to the digitization of the signal; in addition, the plot was set to the same scale as the phantom signal for comparison purposes. The amplitude of the noise appears to be slightly different in the two measurements. This difference can be attributed to the difference in the quantization level of the two measurements as well as the effect of the water on the phantom. The water caused the phantom to swell over time, and in addition, the water became slightly ‘dirty’ from the presence of the phantom, increasing the apparent level of the noise as the acoustic

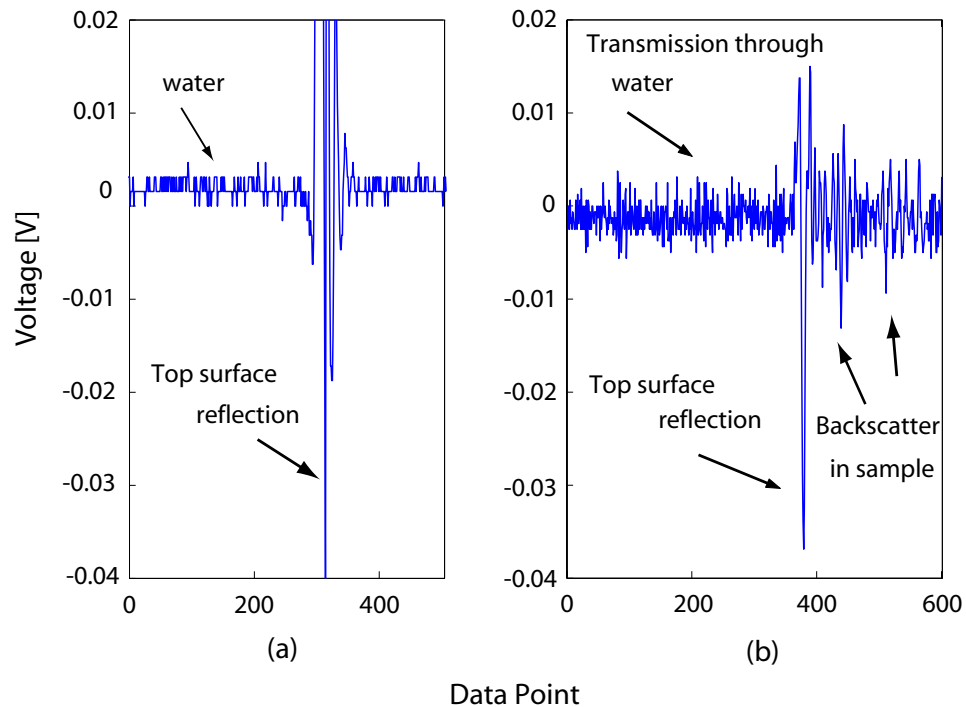


Figure 2.4: Comparing scattering in two samples: (a) HDPE has no scattering particles. The pulse travels through water until the 300th data point, approximately, at which point it reaches the top surface of the sample. After the interface the signal travels through the sample. (b) Tissue phantom with 10% silica particles. The scatterers inside the phantom reflect the wave, causing a higher signal inside the phantom. The noise level for the two figures (the signal from the beginning of the window up to the surface reflection signal) appears differently since the measurements were taken with different voltage settings, resulting in different quantizations of the signals.

pulse propagates through the water. The water was changed daily, and effect of the ‘dirty’ water on the measurements was found to be negligible.

Both samples show a reflection from the front surface approximately 2.5 cycles long. Following the interface echo the HDPE shows no further echoes, however the tissue phantom continues to generate echo signals due to the scattering from the silica particles. The scattered signal decays in time as the propagating wave is attenuated through the sample.

In order to capture the backscatter, the signal should be windowed to capture the reflection off the scatterers, avoiding the impedance mismatches at the front and back surfaces of the sample. The attenuation of the sample needs to be accounted for as do the diffraction effects of the transducer.

The BC can be determined from the pressure scattered from an ensemble of scatterers but for a real measurement all the system characteristics need to be accounted for as well. These characteristics are present in the diffraction, transmission loss and attenuation of the signal, and are accounted for by knowing the transducer parameters and using a measurement from a reference surface. The analysis assumes the phase velocity, attenuation and impedance of the sample are known, and therefore relies on the analysis in Sections 2.1.1 - 2.1.3.

The basic expression for the backscatter coefficient $\eta(\omega)$ is given as

$$\eta(\omega) = \frac{\langle |V_s(r; \omega)|^2 \rangle}{|V_{ref}(2r; \omega)|^2} \cdot \frac{|D_{ref}(2r; \omega)|^2}{l \cdot D_s(r; \omega)} \cdot \frac{1}{\xi^4 \cdot A_s} \quad (2.30)$$

where $V_s(r; \omega)$ is the Fourier transform of the measured backscatter signal from the sample, $V_{ref}(2r; \omega)$ is the spectra of the reflection from a reference material, D_{ref} accounts for the diffraction from the transducer, D_s accounts for the diffraction from the sample measurement, l is the effective thickness of the sample, ξ accounts for the transmission coefficients at the sample-water interface, and A_s accounts for the attenuation in the sample. The diffraction correction terms account for the diffraction effects in the sample and reference surfaces. The $D_{ref}(2r; \omega)$ term is the acoustic coupling function and corrects for the diffraction introduced from the transducer surface to the reference surface and back to

the transducer.

The time gating used for isolating the measurement of $V_s(r; \omega)$ is based on the region of the sample which is analyzed for the backscatter coefficient. From the inspection of the backscatter signals shown in Fig. 2.4(b), the optimal region is just after the reflection from the water-sample boundary, where the amplitude of the echoes from the scattering particles is greatest. The signal from the particles decreases with distance due to attenuation of the pulse, so the extent of the region should be based on the amplitude of the backscatter. In the case of a focused transducer, the center of the selected sample volume should be placed at the focal length, r . The $\langle \rangle$ symbols denote the spatial average of the captured sample signal per frequency across the sample.

For the case of a pulse-echo setup, the pressure measured from a focused transducer from a perfectly reflective surface will be the same as the pressure measured by an identical receive transducer positioned coaxially at a distance twice the focal length from the transmit transducer. Therefore, to account for the pulse-echo setup the measurement of the reference surface, $V_{ref}(2r; \omega)$, stipulates that the roundtrip distance of the pulse be twice the focal length, or a distance r from the transducer.

For the case of a reference surface placed at the focus of a high gain spherically focused transducer, the diffraction correction from the reference surface is:

$$|D_{ref}(2r; \omega)|^2 = \exp \left[-(2/\pi)(G_p/\pi)^{-1/2} \right] \quad (2.31)$$

The term G_p , the pressure gain factor for the transducer, is defined as

$$G_p = \frac{ka^2}{2r} \quad (2.32)$$

where a is the radius of the active element. The spherically focused transducer (PI75-1-R0.50, Panametrics Corp., Waltham MA.) currently used in the SAM has an element diameter of 3.16 mm (0.125 in.) and a focal length of 11.91 mm (0.469 in.). The expression in Eq. 2.31 is valid for values of $G_p > \pi$ and for the SAM transducer the gain varies from 4.55 to 15.91 for the 10-35 MHz range used in the analysis. A more complicated expression exists for the diffraction correction of a transducer with $G_p < \pi$ but was not necessary for our measurements.

The length of the sample which is analyzed for the backscatter is referred to as the effective sample length, l ,

$$l = \frac{c_s(\tau - \tau_p)}{2} \quad (2.33)$$

where c_s is the speed of sound in the sample, τ is the duration of the receive gate and τ_p is the duration of the transmitted pulse.

The term D_s is the diffraction correction function for the backscatter measurement and is defined as the volume integral of the diffraction of the transducer over the sample volume to be analyzed. However, by assuming that the sample is measured at the focal point and that the transducer operates at a high frequency ($ka \gg 1$, where a is the element radius), D_s simplifies to

$$D_s(r; \omega) = \frac{\pi a^2}{r^2} E_\infty \quad (2.34)$$

The parameter E_∞ is a constant, 0.46, and is related to the cross-section of the beam from the transducer used to measure the backscatter.

The attenuation correction coefficient A_s is

$$A_s(\bar{r}; \omega) \cong \exp[-4\alpha(\omega)(\bar{r} - r)] \cdot \frac{\exp[2\alpha\tau_p c_s] - \exp[-2\alpha\tau_p c_s]}{4\alpha\tau_p c_s} \cdot \frac{\exp[2\alpha l] - \exp[-2\alpha l]}{4\alpha l} \quad (2.35)$$

where \bar{r} is the the distance from the transducer to the middle of the sample and $\alpha(\omega)$ is the attenuation of the sample. In cases where $\alpha l \ll 1$ the last two terms approach unity and can be ignored, but the conditions of the SAM dictate that the full expression be used. The expression assumes the sample and the reference are positioned at the focal length. There are a number of methods used to correct for the attenuation in the backscatter signal, and Eq. 2.35 agrees with the formulation recommended by the AIUM, by Sigelmann and Reid [8].

The final effect accounted for in the Chen analysis is the transmission coefficient at the water-sample interface:

$$\xi^4 = \left(\frac{2\sqrt{Z_s \cdot Z_w}}{Z_s + Z_w} \right)^4 = \frac{16(Z_s/Z_w)^2}{(1 + Z_s/Z_w)^4} \quad (2.36)$$

Here Z_w is the acoustical impedance of water and Z_s is the impedance of the sample.

For the configuration used in our SAM, the final expression for the backscatter coefficient, $\eta(\omega)$, is

$$\eta(\omega) = \frac{\langle |V_s(r; \omega)|^2 \rangle}{|V_{ref}(2r; \omega)|^2} \cdot \frac{r^2 \exp[-(2/\pi)(G_p/\pi)^{-1/2}]}{\pi l a^2 E_\infty} \cdot \frac{4\alpha\tau_p c_s \cdot 4\alpha l \cdot \exp[4\alpha(\omega)(\bar{r} - r)]}{\xi^4 [\exp[2\alpha\tau_p c_s] - \exp[-2\alpha\tau_p c_s]] \cdot [\exp[2\alpha l] - \exp[-2\alpha l]]} \quad (2.37)$$

where V_s is the measured scattered signal, V_{ref} is the measured reference signal, and α , c_s and Z_s are calculated from the measurements outlined in Sections 2.1.1 - 2.1.3. All other variables are determined independently.

Chapter 3

Experiment and Validation

3.1 Experimental Setup

Two different setups were used for the SAM, depending on the scan type. The scans, a point-to-point scan and a continuous-motion scan, are described in detail in a following paragraph (see Scanning Methods). The block diagram for the point-to-point scan is shown in Fig. 3.1 and the block diagram for the continuous-motion scan is shown in Fig. 3.2. The main difference between the scans is the triggering source, so the basic setup was similar for the two scans. The sample was positioned on the sample table, which was submersed in water and connected to the top of the tank by a stage which could be manually controlled in the vertical (Z) direction. The transducer was positioned over the sample and pulsed in the downward vertical direction. The transducer was connected to the tank by a three-dimensional positioning system which was mounted to the top of the tank. The transducer

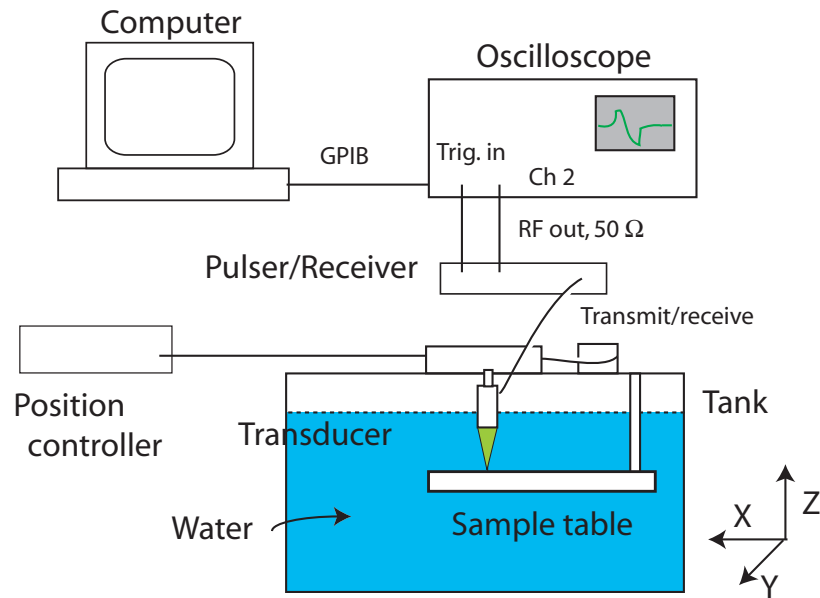


Figure 3.1: The block diagram for the SAM setup for the point-to-point scan configuration.

was excited by the pulser/receiver, which sent the received echo signal to the oscilloscope for display. Finally, the oscilloscope transferred the data to the computer via GPIB for storage.

Transducer The transducer was a spherically-focused PVDF transducer (Model PI75-1-R0.050, G.E. Panametrics Corp., Waltham, MA). The diameter of the element was 3.18 mm (0.125 in) and the specified focal length was 11.91 mm (4.69 in). The center frequency was specified at 53 MHz with the -6 dB bandwidth from 29.2 to 76.6 MHz. The transducer was submerged in a tank filled with distilled water and was directed down over a table suspended from the top of the tank.

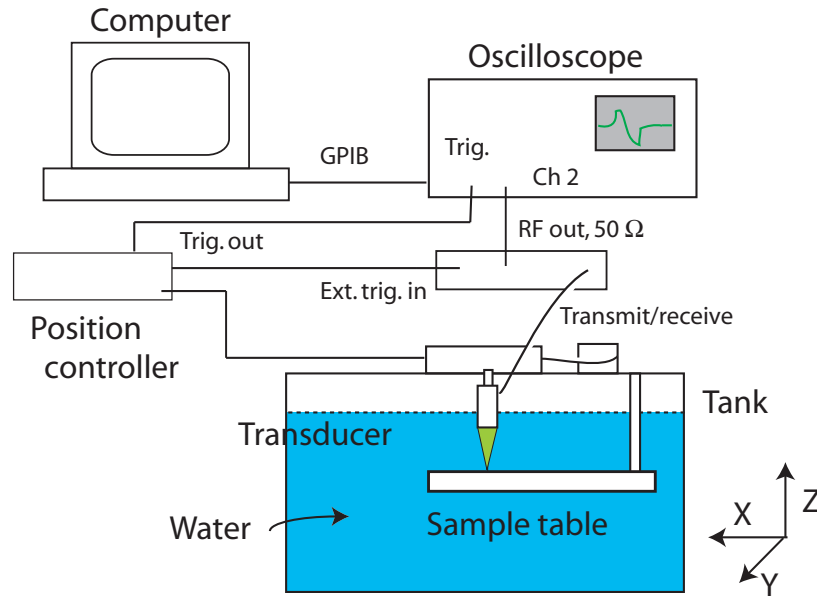


Figure 3.2: The block diagram for the SAM setup for the continuous-motion scan configuration.

Sample Table The sample was placed on a table, shown in Fig. 3.3, which could be adjusted for pitch, roll and height. The table was mounted to a rigid platform via three springs, so that the table surface could be leveled. The table had a groove machined on one side for sample position registration, while the other side was flat, for irregular sample geometries. The grooved side was particularly useful when working with the phantoms, which were mounted on glass slides, allowing the phantom to be removed and returned to the same location. The table was built for a maximum angular range of $\pm 15^\circ$, which was needed for the angle measurements. The platform was connected to two manual translation stages which were mounted to the top of the tank, for translation in the horizontal and vertical directions. Samples that were positively buoyant were weighed down for the measurement by

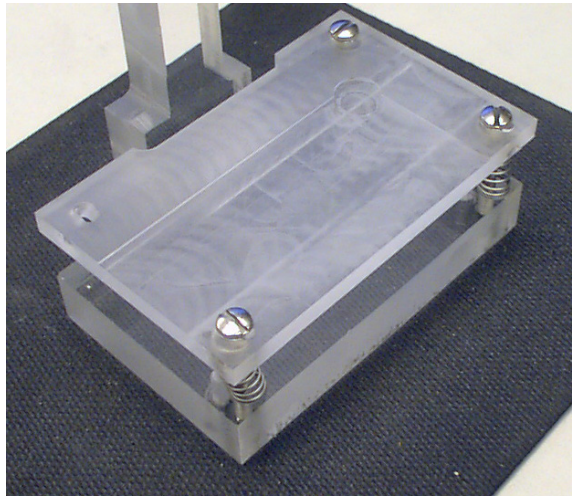


Figure 3.3: The sample table for the SAM setup. The table was removed from the tank for clarity.

a stainless steel washer. In order to allow for a water backing, these samples were positioned on a stainless steel flat with a hole stamped in the middle. The hole and the washer were aligned to provide an acoustical window. The phantoms, as long as they remained fixed to the glass slide, did not have this problem.

The table was leveled by placing a flat glass slide on the table, and then by scanning the transducer along each axis and adjusting the screws so that the arrival time of the pulse was uniform across the surface.

Positioning System The transducer was mounted onto a three-axis translation stage. For translation in the vertical Z direction, a manual actuator was used. The two horizontal axes were controlled by motorized actuators (850G, Newport Co., Irvine, CA) for movement in the X-Y plane. Each actuator had a travel distance of 30 mm with a $0.05 \mu\text{m}$ resolution. The actuators were controlled by a controller/driver (Universal Motion Controller/Driver,

Model ESP300, Newport Co.), which could be controlled directly through a GPIB interface. The driver could be operated under direct control from the computer, or autonomously by an internal program, depending on the scan type. Both modes were used in this work. The driver was set under direct control of the MATLAB scan program (see Appendix) for the point-to-point scan. The internal programming capability of the controller took advantage of the 16 input/output lines which were configured to trigger the pulser/receiver and the oscilloscope when the continuous-motion scan was run. The speed of the actuators was variable and was set to the highest level of 0.5 which corresponded to a speed of about 0.04 mm/s.

Pulser-Receiver The transducer was connected to a 200 MHz pulser/receiver (200 MHz Computer Controlled Pulser/Receiver, Model 5900PR, Panametrics), used in pulse-echo mode. When the pulser/receiver was triggered it sends a voltage pulse to the transducer which converts the signal to a surface vibration which excited the ultrasound pulse. When an acoustic pressure perturbation was incident on the transducer it was converted to a voltage which was sent to the pulser/receiver. The pulser/receiver then processed (described below) the signal and sent it to the oscilloscope, where it was digitized and displayed.

The pulser had an internal trigger, as well as external triggering capability. The pulse repetition frequency was set at 2 kHz when triggered internally, and set to the External-BNC trigger option when the pulser was triggered by the motion controller. On transmit, the damping was set at 50 Ω . The energy setting for the pulse varied for the measurement type: for the impedance measurements, the energy was set to 1 μJ and for all other measurements

the energy was set to $8 \mu\text{J}$. The reasoning behind these different settings will be discussed in Section 3.4. For receive mode, the gain was set to 26 dB (the minimum setting). The received signals were attenuated by 12 dB for the impedance measurements (corresponding to the lower pulse energy setting) and by 19 dB for all other measurements (corresponding to the higher pulse energy setting). The received signal filtering capability was not employed, as the high pass filter was set to the minimum setting (1 kHz) and the low pass filter was set to the highest frequency, 200 MHz. The pulser/receiver was interfaced by MATLAB via RS-232, which was used for switching the triggering, energy and attenuation settings in the course of a scan.

Oscilloscope The signal was displayed, digitized and collected on a 500 MHz oscilloscope (LC334A, LeCroy Corp.). The measured signal consisted of 1000 data points and was sampled at 500 MS/s. The oscilloscope was triggered either by the pulser/receiver or the positioner, depending on the type of scan (see the Scanning Methods paragraph). The received echo signal was transferred from the pulser/receiver via a coaxial cable and after it was digitized it was sent to the computer via GPIB. All other settings were controlled in real time by MATLAB and were set depending on the size of the signal. The oscilloscope had a vertical resolution of 8 bits, and the signals were windowed to minimize the number of points. Multiple voltage scales and time delays were set for the sample scans, since the front and back reflections had different time delays and voltage amplitudes.

The oscilloscope had a sequence mode, which was used in the continuous-motion scans. For this mode, MATLAB sent the oscilloscope the number of datasets and points to collect.

Once the oscilloscope received that number of data sets the entire sequence was sent over GPIB to the computer.

Computer The data was collected on a personal computer (Dimension 8100, Dell Computer Corp.). MATLAB was used to control the driver, pulser and oscilloscope, and was used in the data analysis as well.

Scanning Methods We used two scanning modes: point-to-point and continuous-motion. Both followed a raster scan pattern over the sample, shown in Fig. 3.4. The transducer beam width was calculated at the focal length (11.9 mm) for the range of frequencies which the measurements were analyzed over, 10-35 MHz. For a sound speed of 1491 m/s in water, the corresponding range of wavelengths for this frequency range is 42.6-149 μm . The width of the beam, D , can be determined from [51]

$$D = 1.22 \frac{r_0 \lambda}{a} \quad (3.1)$$

where r_0 is the focal length and a is the radius of the active element. The beam width was calculated to be 0.39-1.40 mm for the range of frequencies which we analyzed in the SAM. The beam width was also measured, using tip of a fiber optic [11], and the beam width was determined to be 0.25 mm.

Therefore, in order to adequately cover the surface of the sample, we used a step size of 0.2 mm and scanned a 2 x 2 mm grid over the sample. Thus, eleven data points were collected in a scan line, resulting in 121 data points for a scan. There were 1000 points per waveform for both scans.

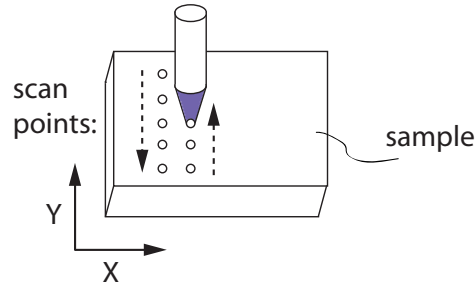


Figure 3.4: The SAM raster scan pattern for the reflection off the surface.

For the point-to-point scan the transducer moved the distance of the step size along the Y-axis and recorded one or more signals which were then downloaded to the computer. The oscilloscope was set in time-averaging mode and averaged the first 500 signals. The oscilloscope was triggered by the pulser/receiver, which was set to a pulse repetition frequency of 2 kHz. Since the measurement consisted of the top and bottom surface reflections, the oscilloscope was windowed twice at each position to maximize the signal for each surface reflection, and the computer recorded the waveform from the oscilloscope following each window setting change. After the top and bottom surface reflections were measured at a particular location, the transducer moved to the next location for the next set of measurements and continued in this fashion to the end of the scan line. Following each translation step there was a slight pause in the MATLAB scan program to ensure synchronization of the translation, the waveform capture and the window setting change, and to avoid mechanical vibration of the transducer following the translation. Once the transducer reached the end of the scan line (i.e., a total translation of 2 mm), the transducer followed the raster pattern

by moving along the X-axis to the next scan line and continued back in the opposite direction. The advantage of the point-to-point scan was that it allowed time averaging of the signal and windowing and collection of multiple signals at each position; the disadvantage was that the scan took a long time since transducer had to stop at every position.

The continuous-motion scan exploited the programmable capability of the motion controller. The MATLAB code generated a one-dimensional scan routine which was written to the positioner. The routine instructed the position controller to move the transducer at a constant speed across the sample and to produce a trigger pulse at a given spatial step. The controller triggered both the pulser/receiver and the oscilloscope, as each was connected to a separate input/output pin on the controller; these pins could be independently set to a high or low level voltage setting. As the transducer moved at a constant speed over the sample, the position controller triggered the pulser/receiver at each spatial step to send an ultrasound pulse.

Since the transducer moved continuously, the window settings had to remain constant for a scan line and only one surface reflection could be measured per line. After each scan line the oscilloscope was triggered to change the window in order to capture the reflection from the other surface, and that particular line was scanned again, in the same direction. The GPIB connection between the oscilloscope and computer was not fast enough to download each waveform at this speed so the oscilloscope was operated in a sequence storage mode. In the sequence mode the data for each position was stored by the oscilloscope for the expected number of positions in the scan line, set by the MATLAB scan program prior to

the scan. At the end of each line, as the transducer returned to the beginning of the next line, the entire sequence of data was transferred to the computer, which would segment the data into separate data sets.

For the continuous-motion scan to be feasible, the ultrasound pulse had to travel fast enough in order to send and receive the pulse without loss of signal while the positioner was moving. The time required for the pulse to travel the roundtrip distance of 22 mm (twice the focal length) through water ($c_w = 1491$ m/s) was 18.1 μ s. At the maximum setting, the speed of the positioner was measured to be 4×10^{-5} m/s, so the positioner travelled 0.6 nm during the time the pulse travelled to the surface and back. The diameter of the beam at the focal length was measured to be 200 μ m, so the loss of signal was deemed to be negligible.

The disadvantage to this method was that due to the trigger mechanism, only one signal could be recorded at a location, so that time-averaging of the signal was not possible. However, for a typical 121-point scan, the continuous motion took 8 1/2 min, while the point-to-point scan took 18 1/2 min for the same scan. This saving in time was particularly useful in the case of the phantoms, which were prone to absorbing water over the course of a scan.

Thickness Measurement The thickness of the sample was determined one of two ways: for most samples, eight measurements of the thickness were taken with a pair of calipers (Model #500-174, Mitutoyo) and averaged before the scan. This method worked fine for the polyethylene samples, since they were machined and of uniform thickness. Although the

tissue varied in thickness, calipers were also used and an average value over eight locations was taken to measure the thickness. The second method was used for the phantoms, which were not uniform and were constructed on a glass slide. Once the phantom was scanned, the phantom and its slide were removed and replaced by a clean, identical glass slide. Thus, this second slide was at the same position as the underlying phantom slide. The reflection off the second slide was windowed and captured. Knowing the speed of sound in water, the time of travel to the slide, and the time of arrival to the top surface of the sample at every data point, half the difference between the two arrival times was multiplied by the water sound speed, yielding the thickness of the phantom at every data point. This method was preferred, since it did not assume a uniform thickness, but was only possible if the sample was mounted to a glass slide with no water layer in between and if the sample table was levelled prior to the scan. The first method could still be used as a spot check in this case.

3.2 Glass Reference Measurement

The acoustical impedance of the glass reference was required in the analysis. Using Eq. 2.4, the impedance was determined by multiplying the sound speed by the density. The density was obtained from the manufacturer and the sound speed was measured using a through-transmission setup [66]. The results from the measurements are listed in Table 3.1. The setup measured the time of travel through the sample, and based on the thickness of the sample, the sound speed is determined. The pulse was sent and collected with a 10 MHz longitudinal transducer using a pulse repetition frequency of 1 kHz. Three samples were

Table 3.1: Sound speed of the glass reference

Sample	Time[μs]	Speed [km/s]
1	0.361	5.48
2	0.362	5.44
3	0.361	5.48
1	0.362	5.44
2	0.366	5.33
3	0.365	5.36
2	0.363	5.41
3	0.365	5.36

used, and the thickness was measured using a digital caliper. The thickness was measured to be 0.98 mm. The speed was averaged to be 5.41 km/s and the impedance was calculated to be 13 MRayls.

3.3 Validation of the Phase Velocity and Attenuation

The analysis of the attenuation and phase velocity and their measurements from the SAM were validated using materials of documented properties. The impedance did not undergo a similar validation since it is involved in the calculation of the attenuation and similar published results were not available for comparison purposes. The results for the impedance, attenuation and phase velocity are presented in Sections 3.3.2 and 3.3.4 along with the causality effects accounted for by the time causal model. The results from the SAM are then compared with documented results in Section 3.3.3.

There were a number of limitations on finding a proper material to validate the SAM: it

had to have been measured and documented by other researchers for comparison purposes, preferably at or near the 15-35 MHz range, and it had to have parallel, planar surfaces and a thickness less than 2 mm in order to conform to the setup of the SAM. Two materials which fit these criteria were used: high-density polyethylene (HDPE) and low-density polyethylene (LDPE). He and Zheng [27] measured the phase velocity and attenuation for both HDPE and LDPE at 1-5 MHz and Wu [68] has similar measurements at 2.2-7.6 MHz. Polyethylene is a commercially available product and can be found in sheet form. When referred to collectively, the Wu and He and Zheng results will be referred to as the WHZ results. Two types of HDPE of varying thickness were measured. The thicker sample (Natural, King Plastic Corp.) was listed at 0.955 g/cm^3 for the density and measured at 1.54 mm for the thickness. The other HDPE (Cat. #111653, Laird Plastics) was listed at 0.94 g/cm^3 and measured to be 0.83 mm thick. LDPE (Cat. #111601, Laird Plastics) is more lossy (higher attenuation) and had to be ordered at a smaller thickness, 0.03 in (measured to be 0.73 mm). The density for the LDPE was listed at 0.92 g/cm^3 .

Since the polyethylene samples did not contain any scatterers they were analyzed for impedance, attenuation and phase velocity but not the backscatter coefficient. The frequency range over which the samples were analyzed depended on how attenuative the material was, and ultimately, on how the strength of the reflection from the back surface. Attenuation increases with distance, so a thicker sample of the same attenuation will have a smaller back reflection and result in a loss of signal at the higher frequencies. The thicker King Plastic (KP) HDPE sample and the LDPE were analyzed from 10-35 MHz, since the

signal approached the level of the noise at frequencies above 35 MHz. The thinner Laird Plastic (LP) HDPE sample was analyzed over a larger range, from 10-45 MHz.

Examining the HDPE response in the time and frequency domain helps provide a picture of the regions in which the signal can be analyzed. The time waveforms for the reflections from the top and bottom surfaces of the KP HDPE sample are shown in Fig. 3.5. The pulse traveled through the water until approximately $15.42 \mu\text{s}$ when it encountered

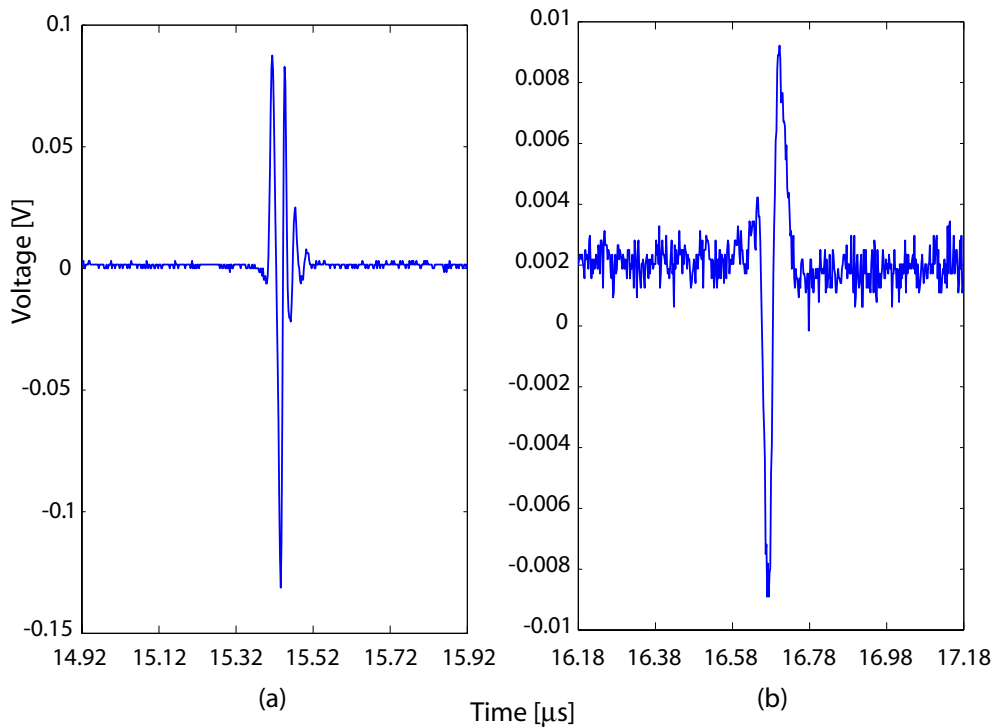


Figure 3.5: Time waveforms for the KP HDPE surfaces: (a) reflection from the top surface; (b) reflection from the bottom surface. Note the difference in the amplitude scale.

the top surface and was partially reflected back to the transducer. The rest of the pulse passed through the top surface and traveled through the sample until it was incident on the bottom surface at approximately $16.68 \mu\text{s}$, as shown in Fig. 3.5(b). The reflection

from the top surface has a larger amplitude than the reflection from the bottom due to the attenuation in the signal from the HDPE. The bottom pulse reveals a slight voltage offset and that the amplitude of the noise is approximately 2 mV peak-to-peak.

The frequency spectra for the top and bottom reflections is shown in Fig. 3.6. The

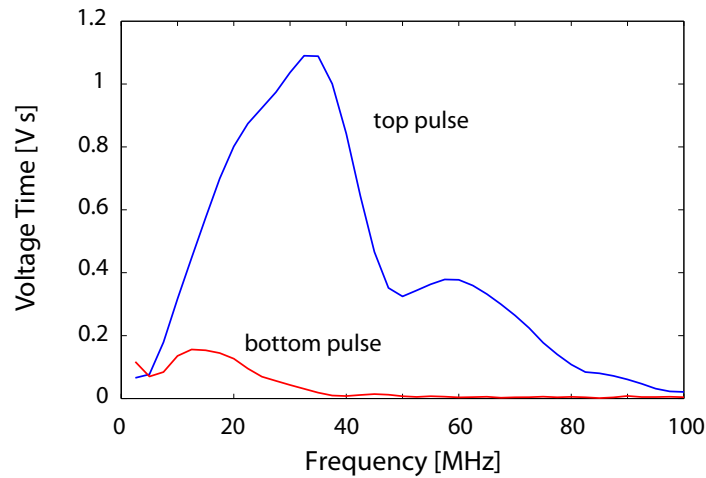


Figure 3.6: Frequency spectra for the KP HDPE surfaces for a pulser energy of $8\mu\text{J}$.

frequency spectra gives an impression of the transducer response, along with the attenuation in the sample. Figure 3.6 shows a -6 dB bandwidth for the top pulse from approximately 13-42 MHz, so it is expected that the data at the frequency limits (10, 35 MHz) will be more noisy and thus have a higher standard deviation. The -6 dB bandwidth for the bottom pulse was shorter, from approximately 5-20 MHz. As in the time domain, the top pulse had a higher amplitude. Below 5 MHz the pulses were at the level of the noise but the two pulses exhibited different frequency responses at the higher frequencies. The top pulse had a steep slope starting at 5 MHz until it peaked around 32.5-35 MHz where it declined steeply to 47.5 MHz. At 50 MHz the amplitude increased with a more shallow slope and

peaked at 60 MHz, where it declined at approximately the same slope down to the noise level. The peak of the bottom pulse was more rounded and at a lower frequency, at 15 MHz. The amplitude decreased gradually to 40 MHz, where there was a slight rise in amplitude similar to the second peak of the top pulse before the amplitude approached zero again at 50 MHz. Comparing the two peaks it is apparent that the frequency response drops sharply after 35 MHz and indeed, the results were not coherent in the frequencies above 35 MHz. An example of the attenuation for the KP HDPE over a 0-100 MHz range is shown in Fig.

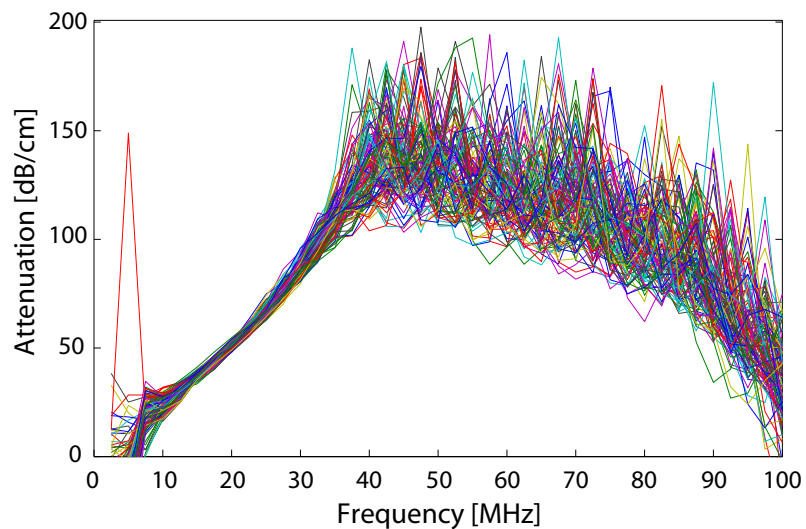


Figure 3.7: Attenuation for the KP HDPE sample. All of the data points are plotted over the 0-100 MHz range. The data is in the noise region below 10 MHz and above 40 MHz.

3.7. The attenuation below 10 MHz and above 40 MHz was lost in the additional signal from the electrical noise, so the data for the KP HDPE was analyzed from 15-35 MHz in order to ensure that the frequency spectra was not corrupted by noise.

3.3.1 Uncertainty

In order to evaluate the response from the SAM the uncertainty from the system was measured. Each component of the SAM has a resolution error as well as a contribution to the noise in the signal. The system uncertainty is an indicator of how much the measurements are affected by all the components of the SAM. The uncertainty of the measurement, σ_m depends on the uncertainty in the sample σ_s and the uncertainty from the SAM, σ_{SAM} :

$$\sigma_m = \sqrt{\sigma_s^2 + \sigma_{SAM}^2} \quad (3.2)$$

The uncertainty of the measurement can be measured by determining the standard deviation of the results at multiple locations across the sample, while the uncertainty of the system can be measured by determining the mean and standard deviation of the results at one location on the sample. The KP HDPE sample was measured for the phase velocity and attenuation at six locations on the sample. The impedance was not analyzed since it is involved in the calculation of the attenuation. Thirty measurements, each consisting of a 500 point time average of the signal, were made at each location and the standard deviation and mean were determined for the phase velocity and attenuation. The mean was determined to have a Gaussian distribution. The results at the six locations varied by a maximum of 5%, indicating that the response of the SAM was relatively constant. Due to the level of the noise and the lower energy of the transducer at its frequency limits, it was predicted that the uncertainty would be highest at 35 MHz, where the energy of the pulses dropped off steeply.

The phase velocity is plotted in Fig. 3.8 with the system uncertainty. The mean phase

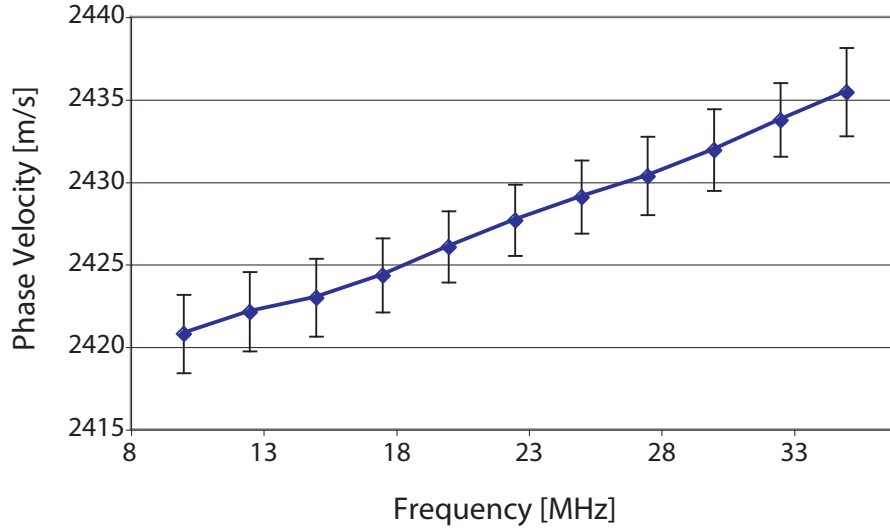


Figure 3.8: Mean phase velocity for the KP HDPE with the standard deviation of the system.

velocity increased from 2420.77-2435.43 m/s and the mean of the standard deviation of the system increased from 2.4-2.7 m/s from 10-35 MHz.

The mean impedance of the KP HDPE is shown in Fig. 3.9. The mean attenuation increased from 23.4-112.7 dB/cm from 10-35 MHz. The mean standard deviation was higher at the lowest and highest frequencies: σ_{SAM} was 1.7 dB/cm at 10 MHz, 1.3 dB/cm at 25 MHz and 4.9 dB/cm at 35 MHz.

3.3.2 HDPE results

The acoustical impedance for the HDPE samples is shown in Fig. 3.10. The slopes for the two samples were similar and were in accordance with our expectations from Eq. 2.15, with the impedance increasing with frequency. The KP sample had a higher impedance

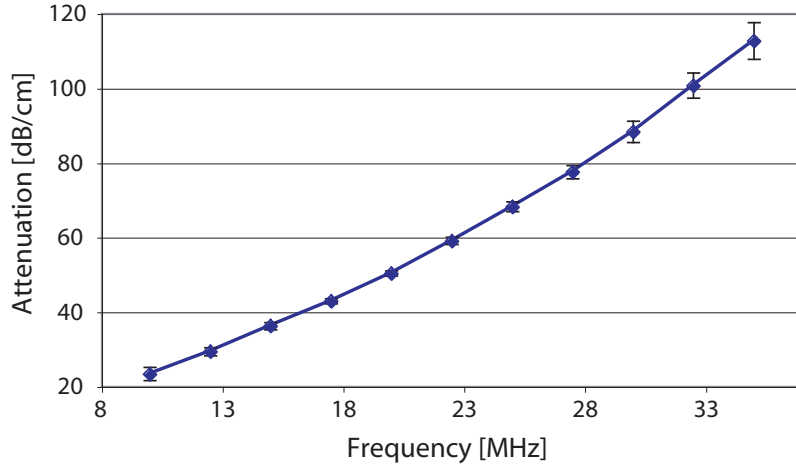


Figure 3.9: Mean attenuation for the KP HDPE with the standard deviation of the system. The system uncertainty was highest at the higher frequencies.

than the LP sample, increasing from 2.33 to 2.42 MRayls over the frequency range. The standard deviation decreased slightly from 0.11 to 0.09 MRayls over the frequency range. The LP sample increased from 2.25 to 2.37 MRayls, and decreased in standard deviation from 0.08 to 0.02 MRayls. This lower standard deviation at the lower frequencies matched our expectations, since the LP was thinner than the KP so the reflection from the bottom surface did not get as attenuated.

The attenuation results for the HDPE samples measured with the SAM are shown in Fig. 3.11. Again, the error bars show the standard deviation for the data across the sample. The LP sample had a slightly higher attenuation than the KP sample throughout the frequency range, increasing from 25 to 119 dB/cm. The standard deviation for the LP was highest at the frequency limits, where the data was noisiest, as demonstrated in

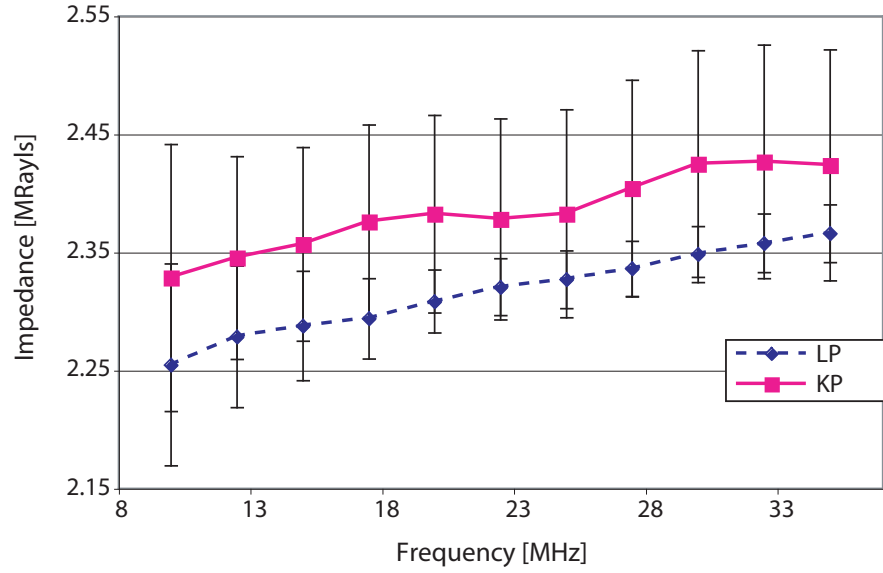


Figure 3.10: Impedance for KP and LP HDPE samples. The slope was similar for both samples.

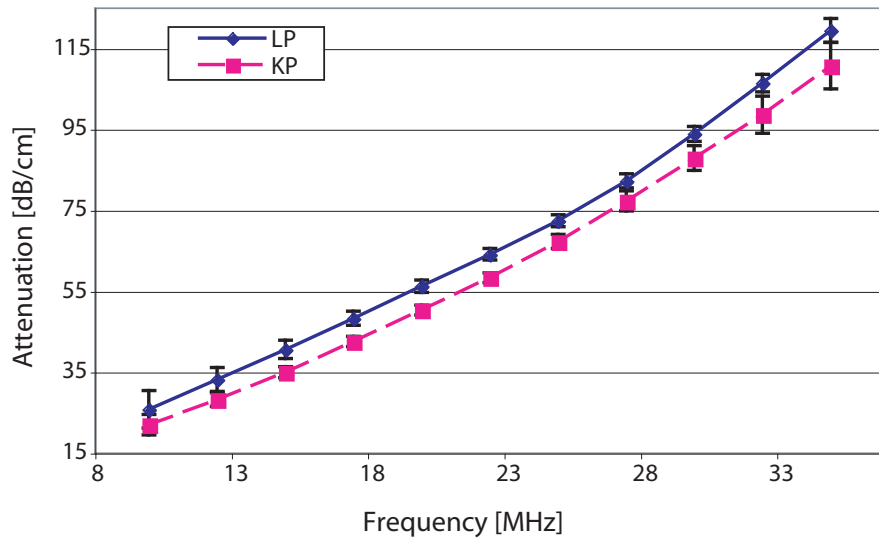


Figure 3.11: HDPE Attenuation results from the SAM. The LP had a slightly higher attenuation. The error bars are the standard deviation from the data.

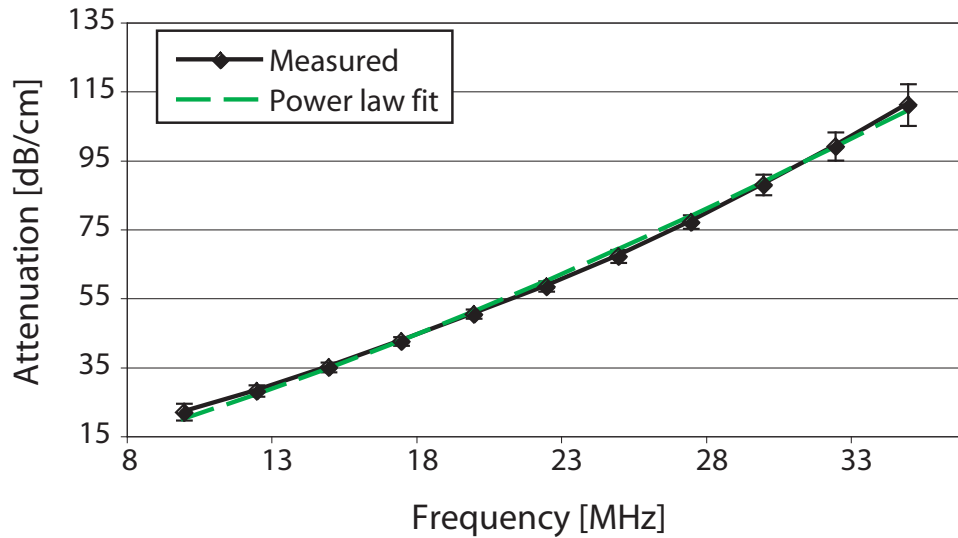


Figure 3.12: Measured attenuation and power law fit of the measured data for the KP HDPE. The fit is within the standard deviation of the measurement.

Fig. 3.6. Accordingly, the lower and higher frequencies had the highest standard deviation, ranging from 1.5 dB/cm in the middle frequencies to 2.3 at 35 MHz and 4.7 dB/cm at 10 MHz. The attenuation for the KP was lower than the LP sample, increasing from 21.8-110.6 dB/cm. The standard deviation was higher than the uncertainty of the system, and was 2.5 dB/cm at 10 MHz, 1.7 dB/cm around 20 MHz, and 5.6 dB/cm at 35 MHz. Using Eq. 2.21, the attenuation was fit a power law, which provided a y value of 1.26 for the LP sample and 1.35 for the KP sample.

The power law fit for the attenuation is shown in Fig. 3.12. The power law fit remains within the standard deviation of the measurement throughout the frequency range, but it is evident that the fit is low at the frequency limits and higher than the measured attenuation near the center frequency.

With α_1 and y determined from the power law fit, the time causal model could be

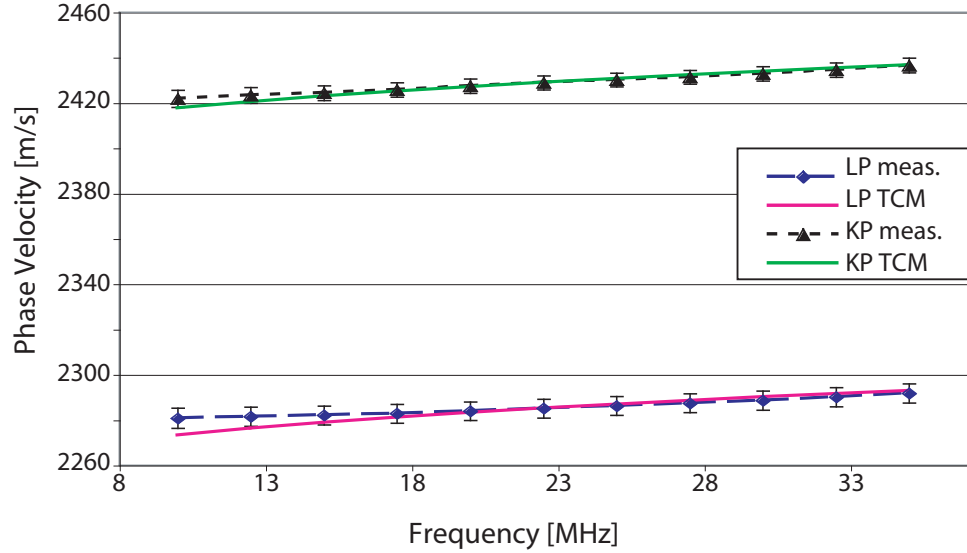


Figure 3.13: Phase velocity results for the HDPE. The thicker KP sample had a higher sound speed than the LP sample but the slopes were similar. The TCM predicted lower dispersion at the lower frequencies for both samples. The larger error bars indicate the standard deviation of the measurement and the smaller error bars are the standard error.

applied to the phase velocity results, presented in Fig. 3.13. The KP sample is the higher solid line and shows some dispersion, increasing from 2421 to 2436 m/s over the 10-35 MHz range. There are two sets of error bars plotted for each sample. The larger error bars are σ_m , the standard deviation of the measurement, and were highest at the frequency limits, approximately 3.2 m/s at 15 and 35 MHz and 2.4 m/s at 25 MHz. As expected from Eq. 3.2, the standard deviation of the measurement was higher than the standard deviation of the system. The smaller error bars show the standard error, σ_{sd} , which represents the confidence in the standard deviation, based on the number of data points N in the measurement.

$$\sigma_{sd} = \frac{\sigma_m}{\sqrt{N}} \quad (3.3)$$

The standard error for the KP sample was relatively constant, around 0.3 m/s, which

indicates a high confidence in the results due to its low value. The time causal model falls within the standard deviation but predicts a lower dispersion in the phase velocity below 15 MHz. The LP sample had a lower phase velocity, ranging from 2280-2291 m/s over the 10-35 MHz range. The standard deviation was similar to the KP sample, staying around 4.2 m/s over the frequency range while the standard error was even at about 0.4 m/s. The time causal model for the LP sample predicts lower dispersion in the phase velocity below 20 MHz. Since the standard error is low and the distribution of the mean is Gaussian, we will use the standard deviation to represent the spread for the rest of the results. The standard deviation is plotted for each set of results as the set of error bars displayed in the remaining figures.

3.3.3 HDPE Comparison

The HDPE measured with the SAM was compared with the WHZ results. The WHZ results were obtained by reading the measured values from their plots and there was an uncertainty of ± 0.2 dB/cm in the attenuation values and ± 0.8 m/s in the phase velocity values. The WHZ results were taken over a lower frequency range and had to be extrapolated to the SAM's higher 10-35 MHz range. The extrapolated values for the attenuation were determined by fitting the data to a power law using the least-squares error routine used for the SAM attenuation analysis. The extrapolated values for the phase velocity were then determined by applying the attenuation coefficient and power law from the attenuation fit to the TCM over the higher frequency range. The same methods were used to extrapolate

the SAM phase velocity and attenuation results to the 1-7 MHz range and in this fashion, the three studies were plotted and compared.

The comparison of the WHZ results and the SAM results for the HDPE attenuation is shown for both frequency ranges of measurements. The low frequency values (1-7 MHz) are plotted in Fig. 3.14. For the lower frequency range, the SAM attenuation extrapolations

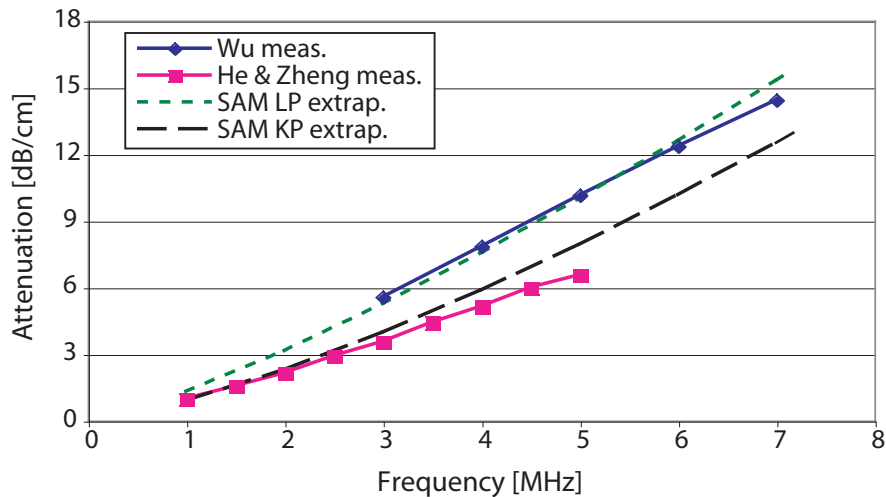


Figure 3.14: Comparison of the HDPE attenuation values between the referenced results and the SAM over the 1-7 MHz range. The four studies fall within the same range and but the WHZ results exhibit a lower power law than the SAM results.

seem to be in good agreement with the WHZ results. The measured attenuation of LP and KP fall in between those of Wu and He and Zheng. However, at the higher frequency range, in Fig. 3.15, the extrapolated WHZ data is not in such good agreement with the measured SAM data. This discrepancy is because the SAM power law is higher for both the KP and LP samples (1.35 and 1.26, respectively) which results in higher attenuation when compared to the WHZ results. The power law values from the fit of the WHZ results are indeed lower: for the Wu sample $y = 1.11$ and for the He and Zheng sample $y = 1.20$. It

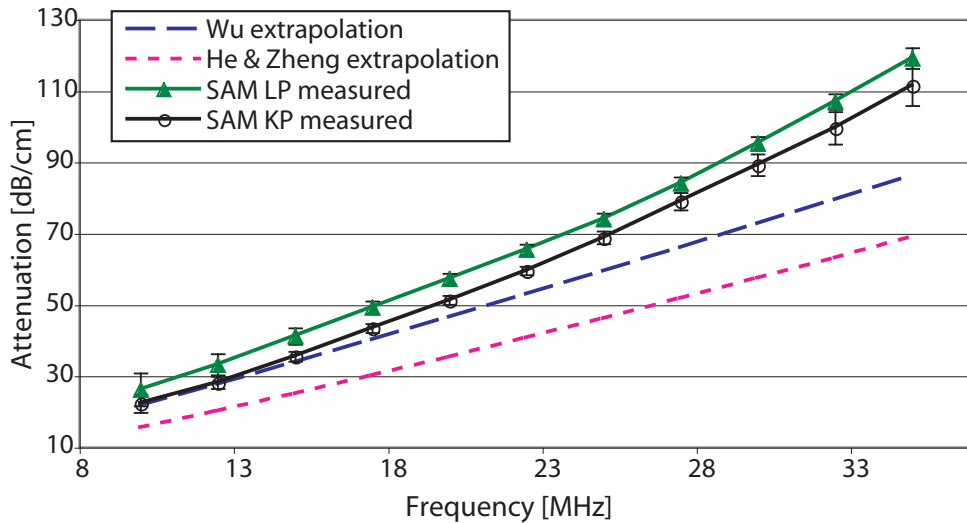


Figure 3.15: Comparison of the HDPE attenuation values between the referenced results and the SAM over the 10-35 MHz range. The SAM results have a higher attenuation at the higher frequencies because of the higher power law values.

should be noted that the power law fit is not perfect and it is clear that there is a jump in value from the SAM fits in the lower frequency range to the respective measured values in the higher frequency range. The combination of the fitting parameters, the extrapolation of the data to the higher frequency range and the method used to obtain the WHZ attenuation results could provide for the difference in the results in the higher frequency range.

The phase velocity values for the HDPE were plotted over two frequency ranges in order to better see the measured versus fit data for the study comparison: Fig. 3.16 shows the phase velocity over a 1-7 MHz range and Fig. 3.17 is plotted over 10-35 MHz. The attenuation parameters from the referenced results were applied to the time causal model and plotted with the WHZ phase velocity results. The two plots show a large spread in the data. In Fig. 3.17 we see that He and Zheng measured a sound speed approximately

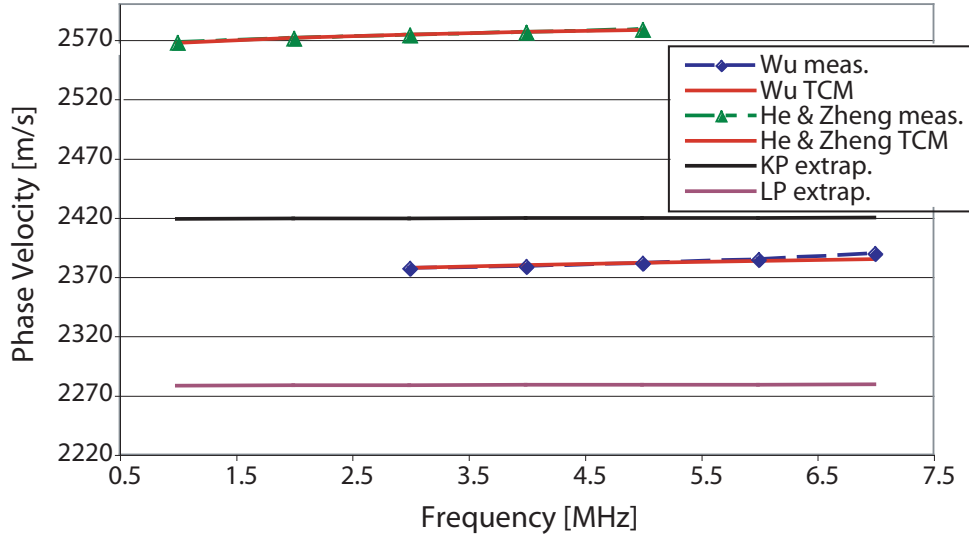


Figure 3.16: Comparison of the HDPE phase velocity values from the referenced results and the extrapolated results from the SAM. None of the results agree but exhibit similar slopes.

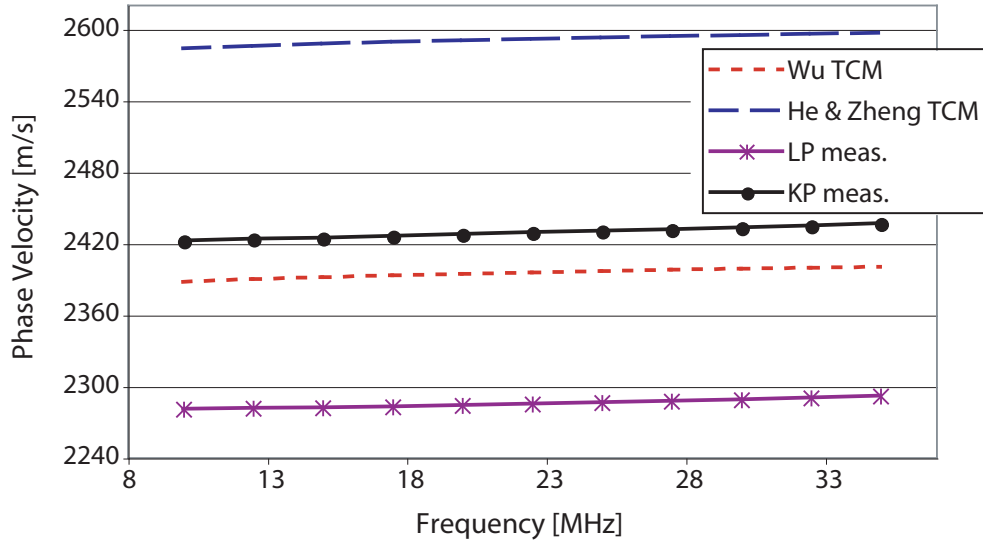


Figure 3.17: Comparison of the HDPE phase velocity values from the SAM and the extrapolated WHZ results. The WHZ extrapolated results both exhibited a slightly lower slope than the SAM results.

Table 3.2: Comparison of manufacturer and measured values for HDPE density at 25 MHz

Sample	ρ_{man} [g/cm ³]	ρ_{SAM} [g/cm ³]
LP	0.94	1.01
KP	0.955	0.98

200 m/s faster than the Wu while the SAM extrapolated results are also lower than the He and Zheng results. Comparing the four results at 4 MHz, He and Zheng measured a sound speed of 2575.8 m/s and Wu measured 2378.2 m/s. The LP phase velocity extrapolation at 4 MHz was 2278 m/s, the lowest among the four studies, while the KP extrapolation was 2418.2 m/s. While there is a large spread in values, each study used samples from different manufacturers, which could explain the variation. However, the slopes for the results are similar. The time causal model for the WHZ results predicts a lower slope for the phase velocity for both studies and the slope for the SAM extrapolations fell in between the two slopes of the WHZ results and TCM.

From the phase velocity and impedance the density can be determined and compared to the manufacturer's values. The manufacturer value and the measured result for the density are shown in Table 3.2. The measured density was higher for both samples, with an approximate 7% difference for the LP sample and approximate 3% difference for the KP sample. The similarity of the densities serves as an additional validation for the phase velocity and impedance measurements.

3.3.4 LDPE results

The impedance of the LDPE measured in the SAM is shown in Fig. 3.18. The LDPE had a

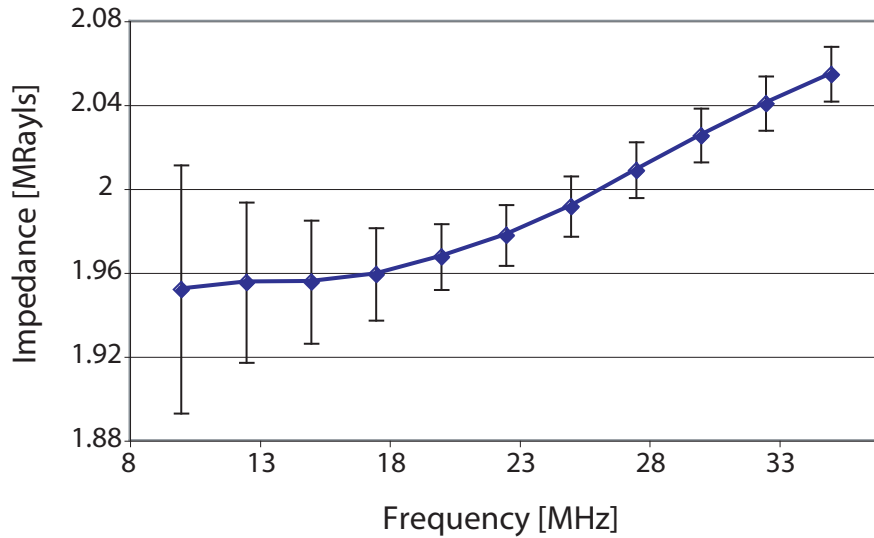


Figure 3.18: SAM LDPE impedance results. The LDPE had a lower impedance than both HDPE samples.

lower impedance than the HDPE samples but exhibited the same general trend, increasing with frequency. From 10-35 MHz the impedance increased from 1.95 to 2.05 MRayls. The standard deviation was larger at the lower frequencies, decreasing from 0.06 to 0.01 MRayls.

The attenuation for the LDPE measured in the SAM is plotted in Fig. 3.19. As was expected from the low amplitude signal from the back surface of the sample, the attenuation for the LDPE was quite high, increasing from 52.08 to 222.33 dB/cm with a power law of 1.21. The standard deviation was 6.8 dB/cm at 10 MHz, 4.7 dB/cm at 25 MHz and 13.9 dB/cm at 35 MHz.

The phase velocity is plotted in Fig. 3.20 with the time causal model. The phase velocity was lower than HDPE but the slope is similar, increasing from 2032.51 to 2059.5 m/s. The dispersion predicted by the time causal model was within the standard error bars but predicted lower phase velocities below 20 MHz. The standard deviation decreased from

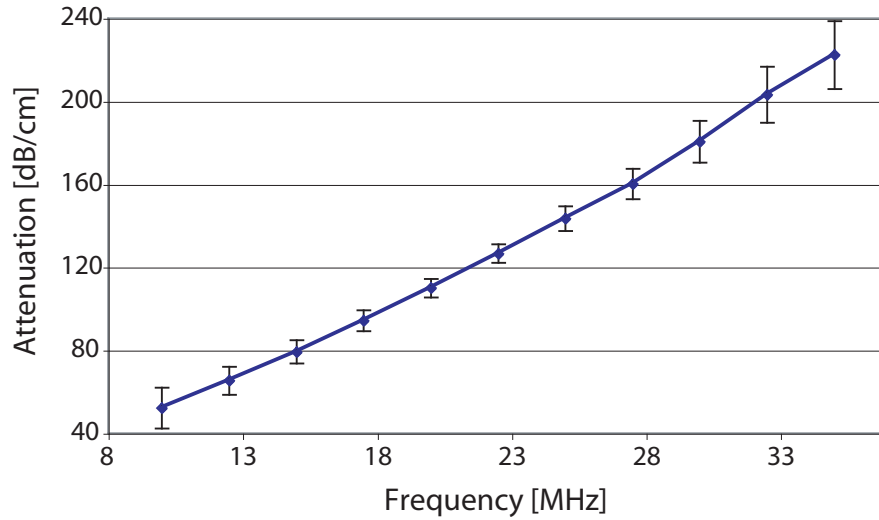


Figure 3.19: SAM LDPE attenuation results. The LDPE had a higher attenuation than both HDPE samples.

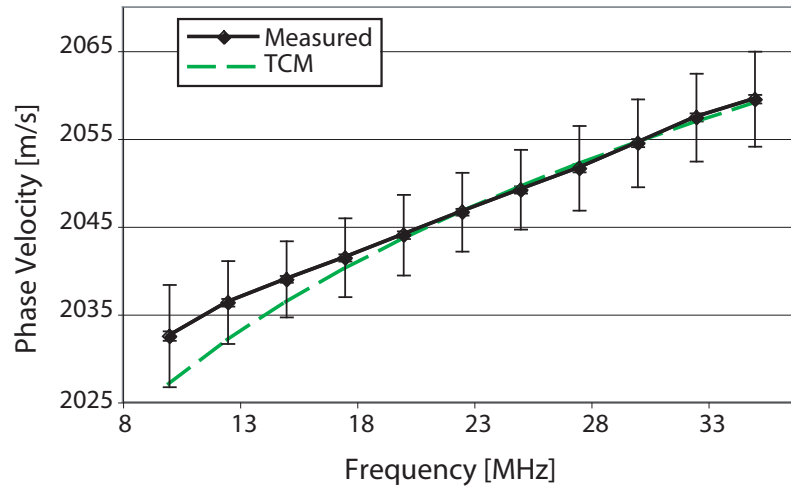


Figure 3.20: LDPE Phase velocity measured by the SAM. The time causal model is within the standard error bars everywhere except the higher frequencies.

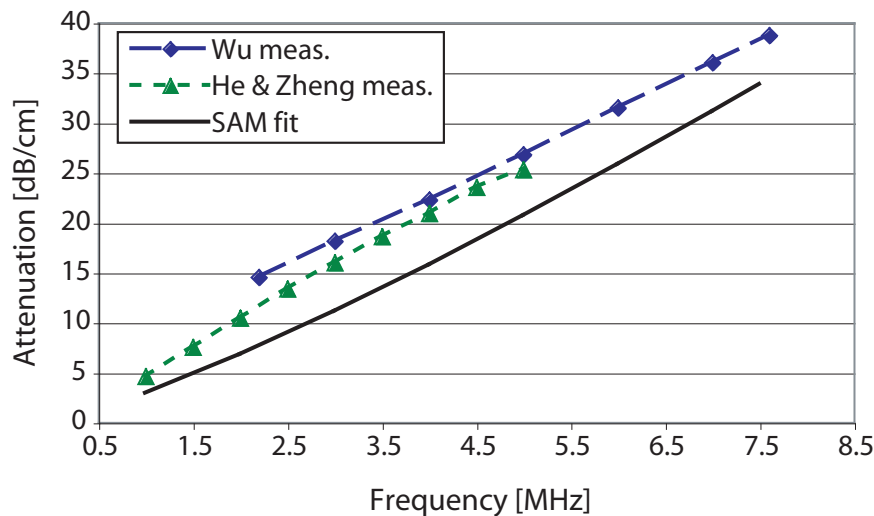


Figure 3.21: Comparison of the WHZ attenuation results with the SAM extrapolation for LDPE. The three studies fell within the same range.

5.33 m/s at 10 MHz to 4.24 m/s at 25 MHz and increased to 5.38 m/s at 35 MHz.

3.3.5 LDPE comparison

The extrapolation of the SAM results for the LDPE over the lower frequency range is shown with the WHZ results in Fig. 3.21. The three results fell in the same range for the lower frequencies. Wu had the highest attenuation, increasing from 14.5 to 38.8 dB/cm with a power law of $y = 0.82$ while the SAM extrapolation had the lowest attenuation, increasing from 3.4 to 33.2 dB/cm over 1-7 MHz. He and Zheng's results fell in the middle, increasing almost linearly from 4.7 to 23.3 dB/cm with a power law of $y = 0.99$.

When the WHZ results were extrapolated to the higher frequency range, in Fig. 3.22, the difference in power laws became more apparent, resulting in a larger spread of the

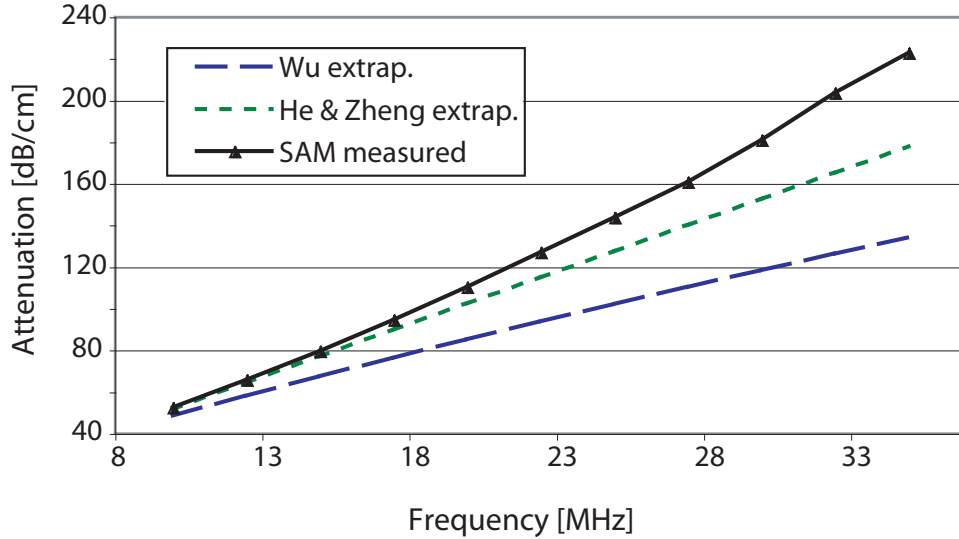


Figure 3.22: Comparison of the SAM attenuation measurements with the WHZ extrapolations for LDPE. The SAM results were higher than the WHZ extrapolations because the SAM LDPE had a higher power law.

attenuation. The SAM results had the highest power law so the SAM LDPE had the highest attenuation. The Wu measurements had the lowest power law and therefore had the lowest attenuation at the higher frequencies, while the He and Zheng extrapolated results fell in the middle of the three studies.

The phase velocity for the SAM and the WHZ results is plotted over two frequency ranges as well. The lower frequency range is shown in Fig. 3.23. The LDPE results for the three studies are similar to the HDPE results. There is a large difference in value between the WHZ results, with the Wu sample approximately 500 m/s higher than the He and Zheng sample, while the SAM extrapolation was similar to the He and Zheng result. As in the case of the HDPE as well, the WHZ measurements show a slightly higher dispersion than the corresponding TCM. WHZ also show more dispersion than the extrapolated SAM data

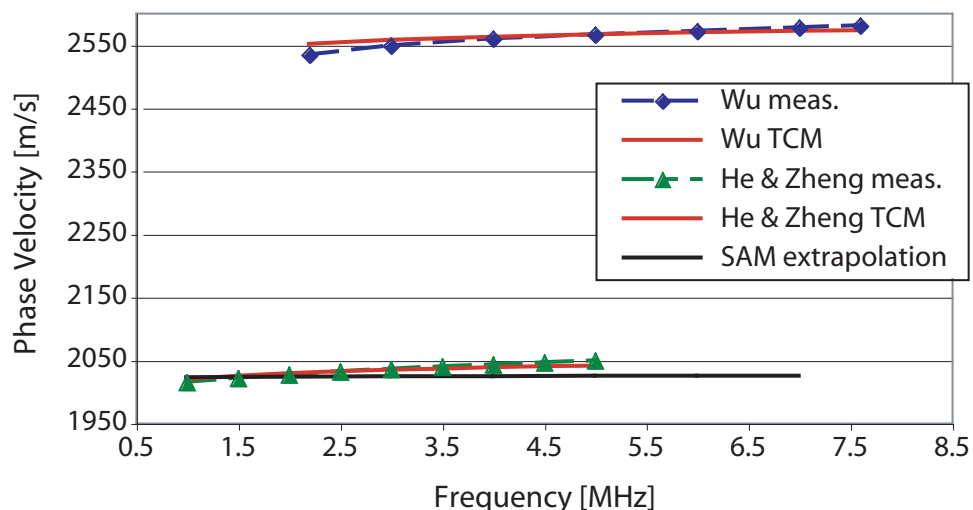


Figure 3.23: Comparison of the phase velocity of the WHZ results with the extrapolated results from the SAM for LDPE. The slopes are similar but there is a large spread in the results.

and this can be seen clearly in Fig. 3.24. The extrapolation of the WHZ phase velocity from the TCM exhibited a lower slope than the SAM results, resulting in similar values for the phase velocity between the He and Zheng extrapolation and the SAM results at the higher frequencies.

The density was calculated and compared to the manufacturer value for LDPE as well. At 25 MHz, the density was measured to be 0.90 g/cm^3 , compared with the manufacturer's value of 0.92 g/cm^3 ; this represents approximately 2% difference in the densities.

The SAM HDPE and LDPE results for the phase velocity and the attenuation compare favorably with the results published by Wu and He and Zheng. There is some spread in both of the phase velocity and attenuation values, but there is also a large spread within the WHZ results and this spread could be due to the different samples used for the studies. The time causal model shows that the slope for the phase velocity is appropriate. The

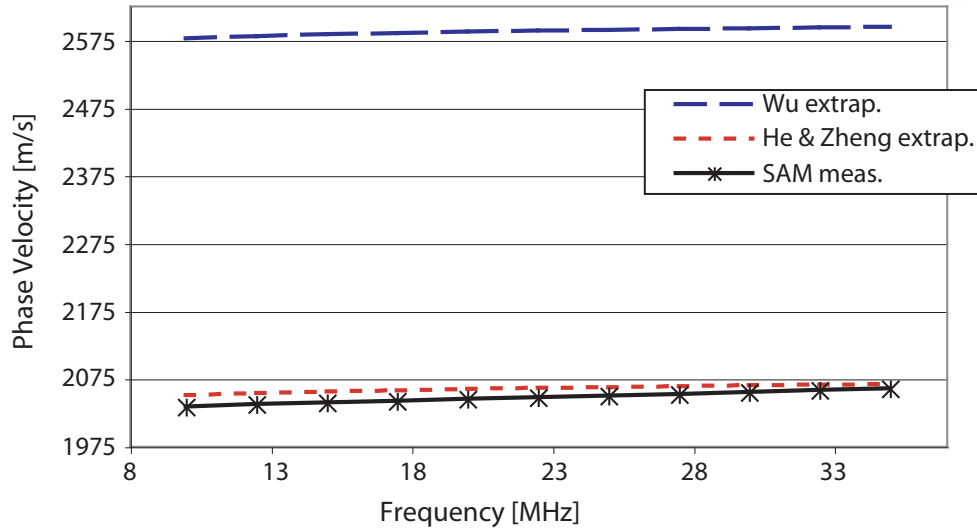


Figure 3.24: Comparison of the LDPE phase velocity results from the SAM and the extrapolated results from the referenced results. The SAM measurement is similar to the He and Zheng results but exhibits a steeper slope.

impedance and phase velocity were verified by matching up closely with the manufacturer values for the density for all three samples.

3.4 Impedance Measurements

The amplitude of the transmitted signal was varied using the energy setting on the pulser-receiver. The effect of the energy setting on measurements of impedance, attenuation and phase velocity was made for the different energy settings. The attenuation and sound speed measurements were insensitive to the energy level but the impedance did show some variation. The use of higher energy levels in the pulse was motivated by a desire to increase the signal-to-noise (SNR) ratio. The HDPE samples, particularly for the thickness of the samples used in this study, had a relatively high SNR ratio, but the high attenuation of the

LDPE samples and thickness of the tissue meant that the reflection from the back surface was close to the level of the noise. By increasing the energy of the pulse we hoped to increase the amplitude of the echo from the back surface.

To examine the role of the energy level HDPE was measured and the energy settings were varied from 1 to 8 μJ for the HDPE and the reference slide. To prevent clipping of the echo from the reference it was necessary to adjust the receive attenuation, as shown in Table 3.3. The receive gain was left at the lowest setting, 26 dB.

Table 3.3: Pulsar/Receiver settings

Transmit Energy [μJ]	Receive Attenuation [dB]
1	12
2	14
4	17
8	19

Figure 3.25 shows the impedance as a function of frequency for the four energy levels. For the lowest energy level, $E = 1 \mu\text{J}$, the slope of the impedance had a steady increase with the frequency as expected from the fact that $Z(f) = \rho \cdot c(f)$ and the phase speed increases with frequency. At 2 μJ the impedance started out lower but had a peak around 42 MHz. The higher energy levels, 4 and 8 μJ , showed similar responses but peaked at lower frequencies, around 37.5 and 30 MHz, respectively.

One possible reason for the peak is that increasing the energy into the transducer increases the amplitude of the lower frequencies. Figure 3.26 shows the magnitude of the frequency spectra of the glass reference which exhibits a more rounded and even distribu-

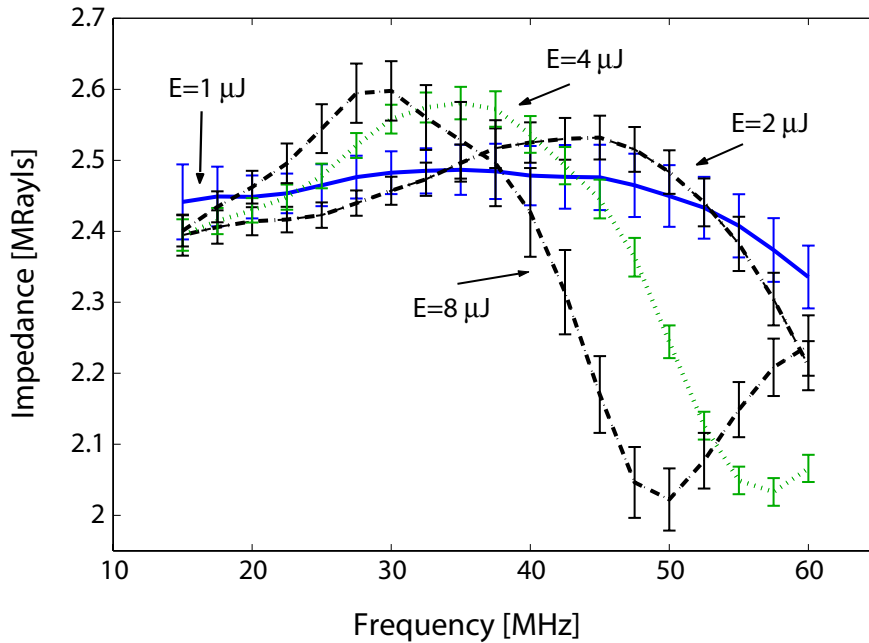


Figure 3.25: Initial experimental results for the HDPE impedance at multiple energy levels. ‘E’ indicates the energy.

tion for $E = 1 \mu\text{J}$ while the higher energy levels show peaks that are consistent with the peaks in the impedance. However this effect should be compensated for by the reference measurement from the glass.

Figure 3.27 shows that the frequency spectra of the reflection from the top surface of HDPE for the multiple energy levels is slightly different from the response for the glass reference. The response at the first energy level is similar but the peaks of the higher energy levels appear smoother and more rounded for the HDPE than for the glass. In particular, the slope for $E = 8 \mu\text{J}$ for the glass reference has a dip around 30 MHz which is not apparent for the HDPE response. Equation 2.14 shows that the impedance is partially determined from the ratio of the magnitude of the glass and HDPE spectra, so the difference in the

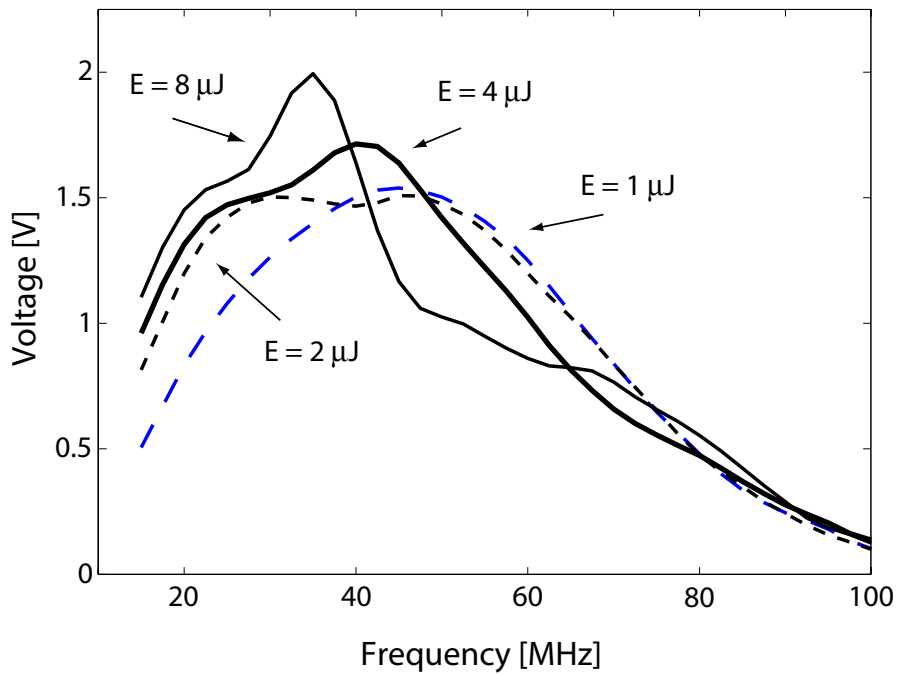


Figure 3.26: Spectra of echoes from the glass reference at multiple energy levels.

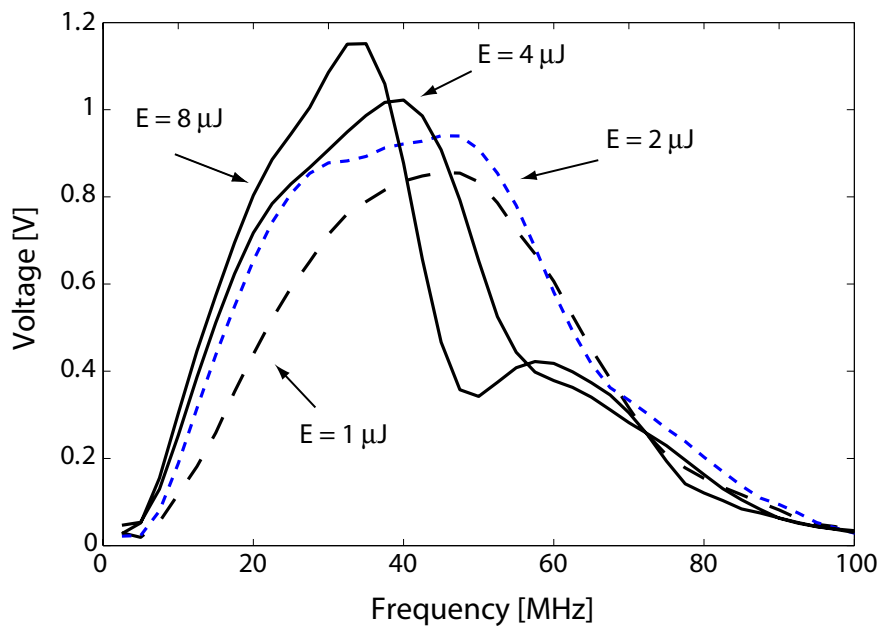


Figure 3.27: Spectra of echoes from the top surface of HDPE at multiple energy levels.

response from the glass and the HDPE will have an impact on the impedance.

The distance from the transducer to the sample surface was investigated to see if the discrepancies were due to differences in diffraction of pulses with different frequency content. The sample was measured 1 mm before and after the focal length in an effort to investigate the possible effects of diffraction on the pulse. The focal length of the transducer is listed as 11.91 mm, so the sample and glass were measured at 11 and 13 mm. The impedance response for the 11 mm distance was similar to the impedance for the focal length. Figure 3.28 shows that the impedance values across the energy levels are in somewhat better agreement when the sample was imaged at 13 mm but the results were not significantly better than at the focal length. Sample distances of 14 and 15 mm showed similar results to the results at 13 mm. Since there were no significant differences with sample distance, diffraction was ruled out as an explanation to the difference in impedances.

The effect of the energy setting was examined for the attenuation and phase velocity measurements as well. Figures 3.29 and 3.30 show that both the attenuation and phase velocity are independent of the energy setting. The attenuation for the four energy settings is in close agreement throughout the lower frequency range and varies by 5 dB/cm at 35 MHz but all four results overlap by their standard deviations. The phase velocity plot shows some variation between energy levels but there is no clear trend with energy level. All the curves show a similar slope but the absolute values vary by up to 4 m/s. However, for both the attenuation and phase velocity, the highest energy level had the lowest standard deviation at the higher frequencies and was in close agreement with the 1 μ J measurements.

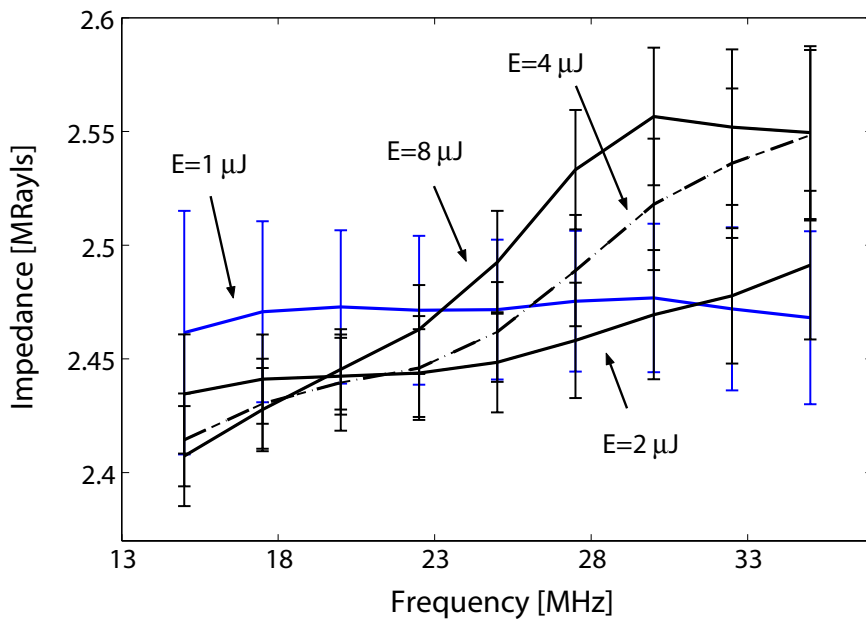


Figure 3.28: HDPE impedance at 13 mm.

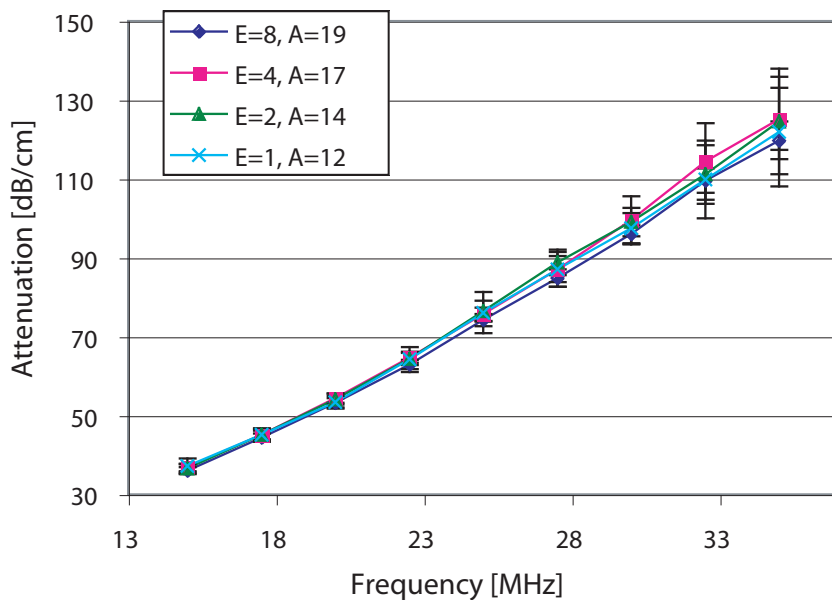


Figure 3.29: HDPE attenuation for each energy level, measured at a transducer-sample distance of 12 mm. The four results overlap their respective standard deviations.

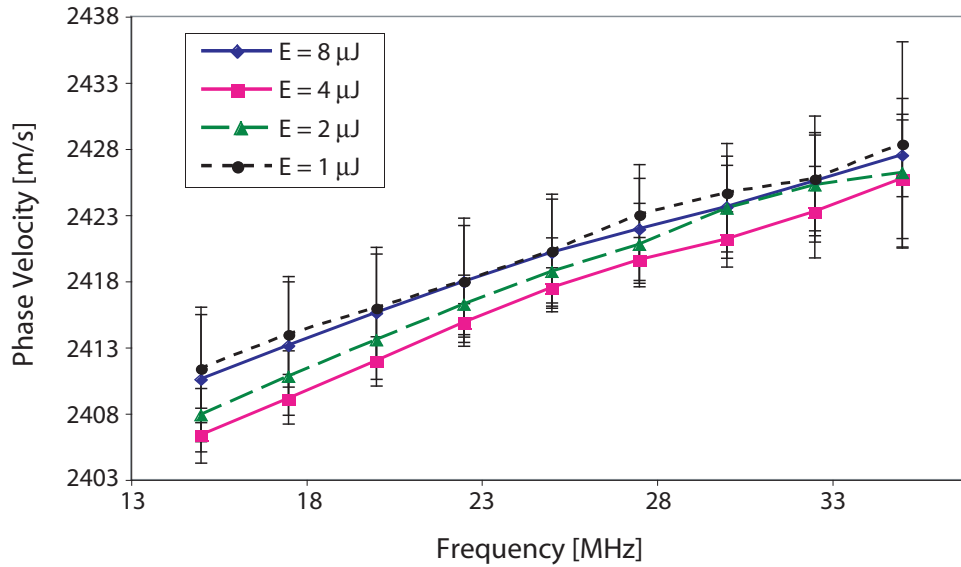


Figure 3.30: HDPE phase velocity for each energy level, measured at a transducer-sample distance of 12 mm. The four results are similar but vary by approximately 4 m/s. The phase velocity for $E = 8 \mu\text{J}$ has the smallest standard deviation at the higher frequencies.

The low standard deviation makes sense since the signal to noise ratio through 35 MHz is improved with the higher energy setting. Therefore, the attenuation and sound speed for all the measurements were both measured using the higher energy level, $8 \mu\text{J}$.

The discrepancy of the impedance changing with the energy is still unresolved. While changing the focal length brings some agreement, there is still a basic difference in the slope of the impedance between the expected $1 \mu\text{J}$ curve and the curves found in the 2, 4 and $8 \mu\text{J}$ settings. However, the discrepancy between the energy settings was less than 5%. Higher energy levels are not necessary to collect the required data to back out the impedance, so the reported impedance values were taken on the $1 \mu\text{J}$ energy setting.

3.5 Focal Region

The placement of the sample within the focal region was tested in order to examine the allowable range for the sample size. In order to assume plane waves, the sample cannot be too thick: a large thickness would position part of the sample outside of the focal region, where the waves are not planar. The alternate limit, on the minimum thickness, dictates that the sample merely be thick enough so that the reflections off the front and back surfaces are distinguishable from each other, approximately 0.3 mm. Additionally, mapping the focal region provided an optimal position for placement of the sample for the rest of the measurements.

The focal length of the SAM's transducer was listed at 11.91 mm, so the measurements centered around 12 mm. The procedure for measuring the focal region consisted of examining the reflection and propagation characteristics of the KP HDPE and the glass reference at 0.5 mm steps for distances ranging from 9 to 15 mm between the transducer and top surface of the sample. Recalling from Sec. 3.3, the thickness of the KP HDPE sample was 1.54 mm. From these measurements, the phase velocity, attenuation and impedance were determined and the optimal region for sample position was based on these results. We expected the measurements of the phase velocity, attenuation and impedance to be relatively constant throughout the focal region. The distance was set by adjusting the vertical micrometer on the table and was measured by moving the cursor on the oscilloscope to the time setting corresponding to the specified distance, based on the sound speed of water.

The magnitude of the spectra for the echo from the top surface of the HDPE at 9.5,

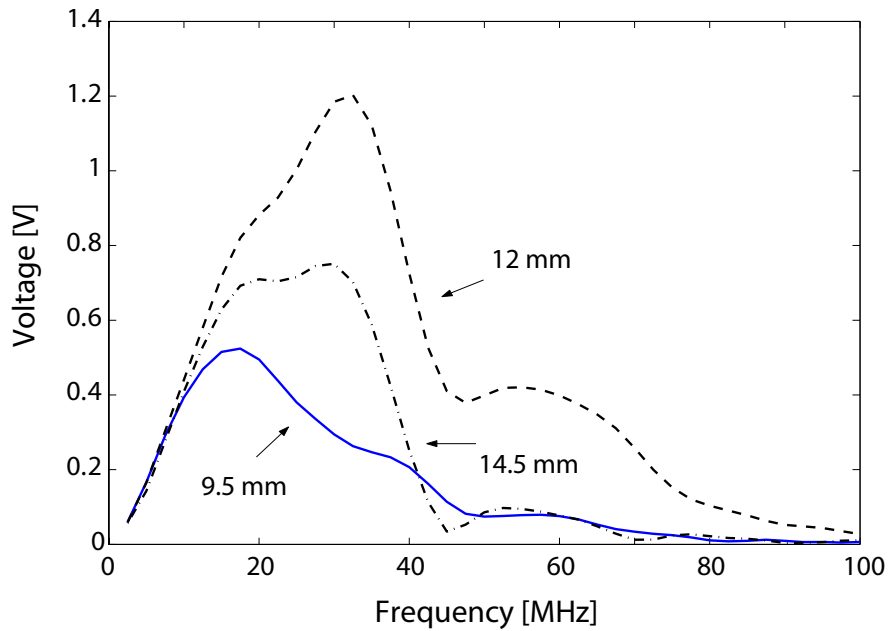


Figure 3.31: Frequency spectra of the echo from the top surface of HDPE placed at 9.5, 12 and 14.5 mm from the transducer.

12 and 14.5 mm are shown in Fig. 3.31. The extreme distances, 9 and 15 mm, were clearly outside of the focal region, and their respective frequency spectra plots were quite different from those near the 12 mm, the listed focal length. Instead of the steady increase in slope up to 35 MHz typically demonstrated in the 12 mm frequency spectra plots, the plot for the 9 mm distance peaked at 17.5 and 37.5 MHz, with a sharp valley at 27.5 MHz. The 15 mm plot of the frequency spectra showed a plateau at 20 MHz and decreased sharply at 30 MHz. Based on the frequency spectra plots, the near and far field distances produced results which were quite different from the rest of the distances.

The results for the phase velocity at 25 MHz are shown in Fig. 3.32. The phase velocity remained relatively constant from 11 to 12.5 mm, around 2420 m/s. With the exception of

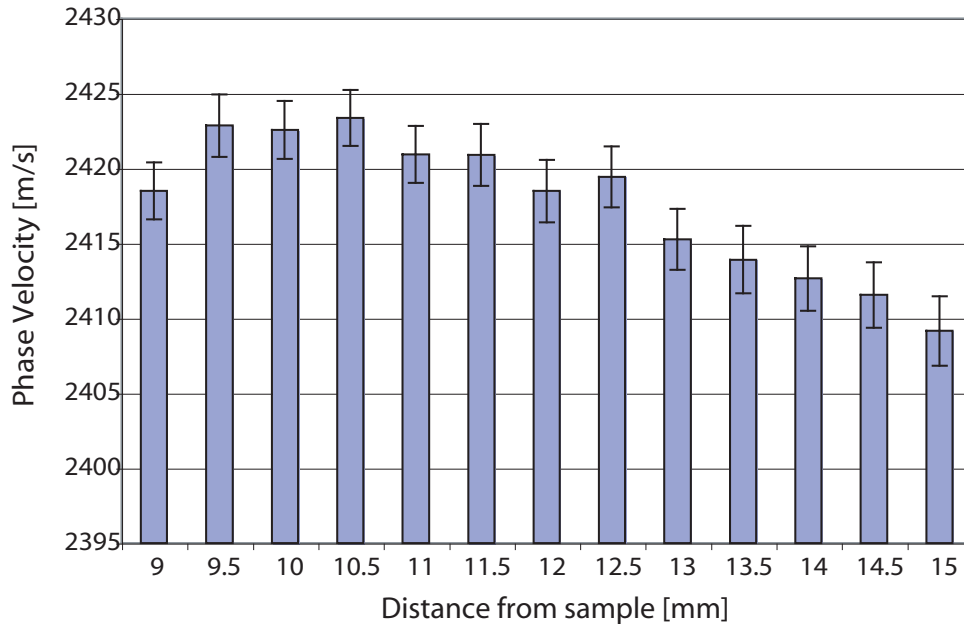


Figure 3.32: HDPE phase velocity at 25 MHz as a function of transducer-sample distance. The phase velocity decreased as the sample was placed farther from the transducer.

9 mm, the near field (9.5-10.5 mm) was higher, around 2422 m/s, and the far field (13-15 mm) was lower than the focal region, decreasing steadily to 2409 m/s. The phase velocity measurements did not provide a clear focal region, although the 11-12.5 mm region, which included the specified focal length, remained relatively constant.

The attenuation at 15, 25 and 35 MHz is shown in Fig. 3.33. The attenuation increased as the sample was placed farther from the transducer. This trend was expected because of how the geometric focusing of the pulse affects the reflection from the front and back surfaces in the near and far field regions. The energy increases as the pulse focuses, so in the near field the energy will be higher at the back surface. Recalling from Eq. 2.21 that the attenuation is determined partially from the ratio of the signal from the top and bottom

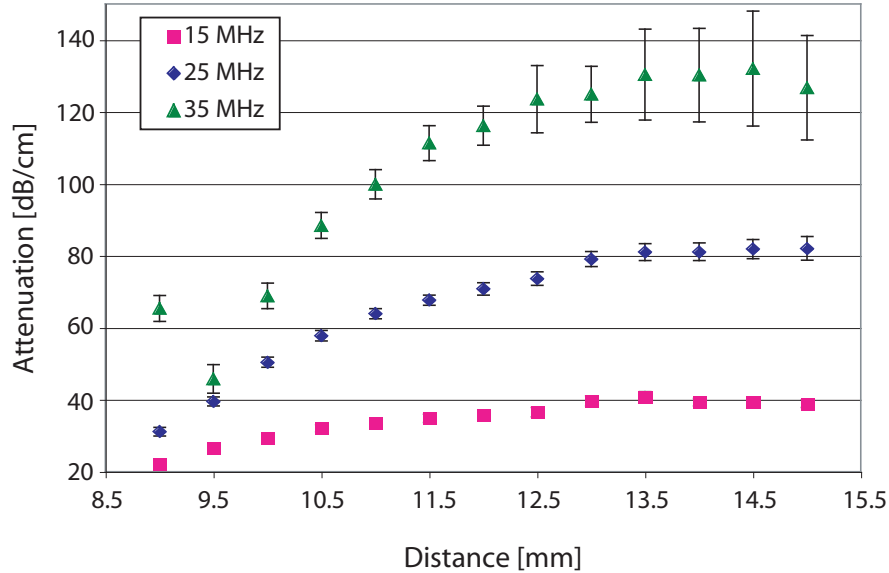


Figure 3.33: HDPE attenuation at 15, 25 and 35 MHz as a function of the sample-transducer distance.

surfaces, a stronger reflection from the back surface will make the attenuation appear to be smaller. The opposite occurs in the far field: as the pulse widens and spreads out, the energy will be higher at the front surface and the reflection from the back surface will appear more attenuated. For a sample thickness smaller than the depth of the focal region, the energy throughout the focal region should be similar at each surface so the attenuation should stay constant. There does not appear to be a clear focal region in Fig. 3.33, as the attenuation increased steadily until approximately 13 mm. The high attenuation at 9 mm from the transducer indicates that the attenuation does not follow the expected power law.

Some further insight is provided by Fig. 3.34, which shows the attenuation for each position at 15, 25 and 35 MHz, normalized by the attenuation of the HDPE 12 mm from the transducer. The plot reveals a high slope from 9 to 11 mm but is relatively flat from

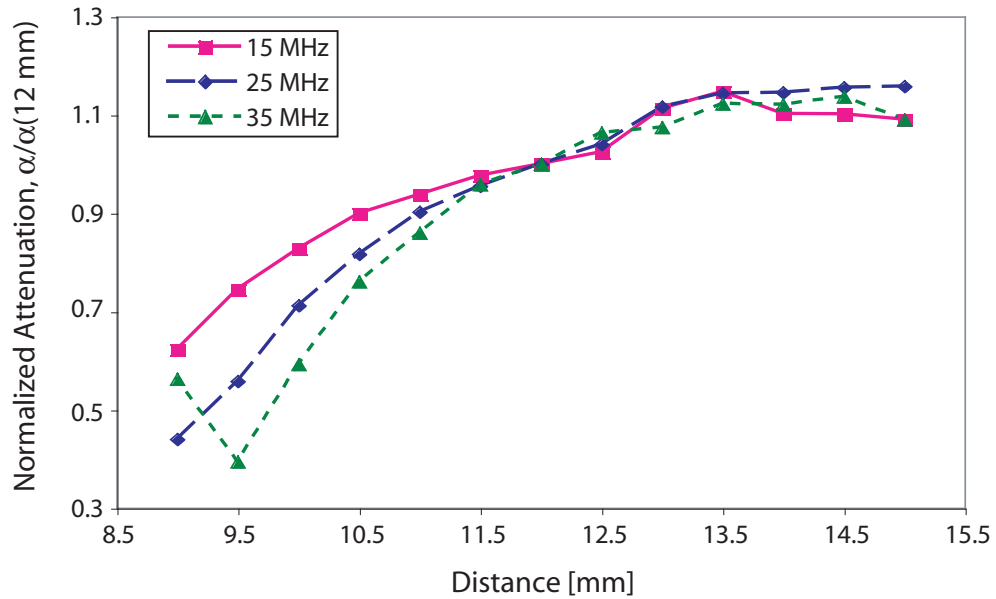


Figure 3.34: HDPE attenuation at 15, 25 and 35 MHz as a function of the sample-transducer distance normalized by the attenuation at the focal length.

11 to 12.5 mm. The normalized attenuation increases sharply from 12.5 to 13 mm where it decreases for the 15 and 35 MHz frequencies. Therefore, the flat region from 11-12.5 mm indicates a focal region.

Out of the three property measurements, the impedance plot displayed in Fig. 3.35 displays the best guideline for choosing the optimal sample position. Disregarding the 9 mm measurement, the impedance increased steadily from 2.26 MRayls at 9.5 mm and peaked sharply at 2.45 MRayls at 12 mm. Past 12 mm the impedance fell off less steeply. The peak in the impedance corresponded with the nominal focal length, where the pulse should have the highest energy. The standard deviation stayed relatively constant at 0.02 MRays from 10-15 mm.

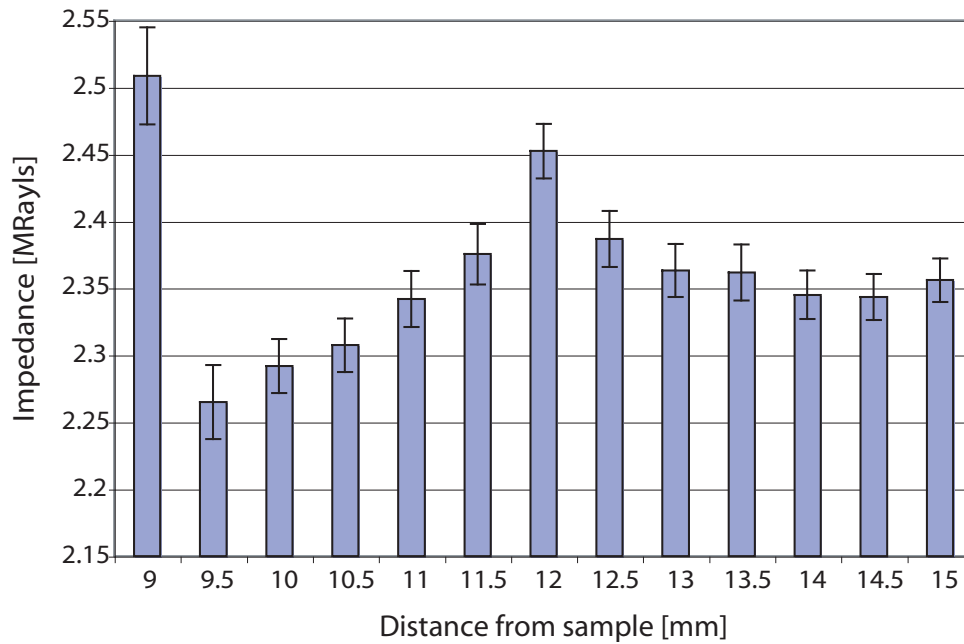


Figure 3.35: HDPE impedance at 25 MHz per distance. The impedance peaks at the focal length.

An additional visualization of the focal region can be provided by examining the frequency spectra over the range of distances. Figure 3.36 shows the reflection from the glass reference for the 10, 20 and 35 MHz frequencies, normalized by the magnitude at 12 mm. The ratio of the pressures at the three frequencies is relatively constant from 11.5-12.5 mm and feature an increase in the near field and a decrease in the far field. A similar plot for the reflection from the top surface of HDPE agrees with Fig. 3.36. The results at 9 mm are ignored since the data does not follow the expected power law, indicating that the distance is out of the focal region.

All three property measurements indicated a region where the results remained locally constant. The phase velocity remained constant from 11.5-12.5 mm and the attenuation

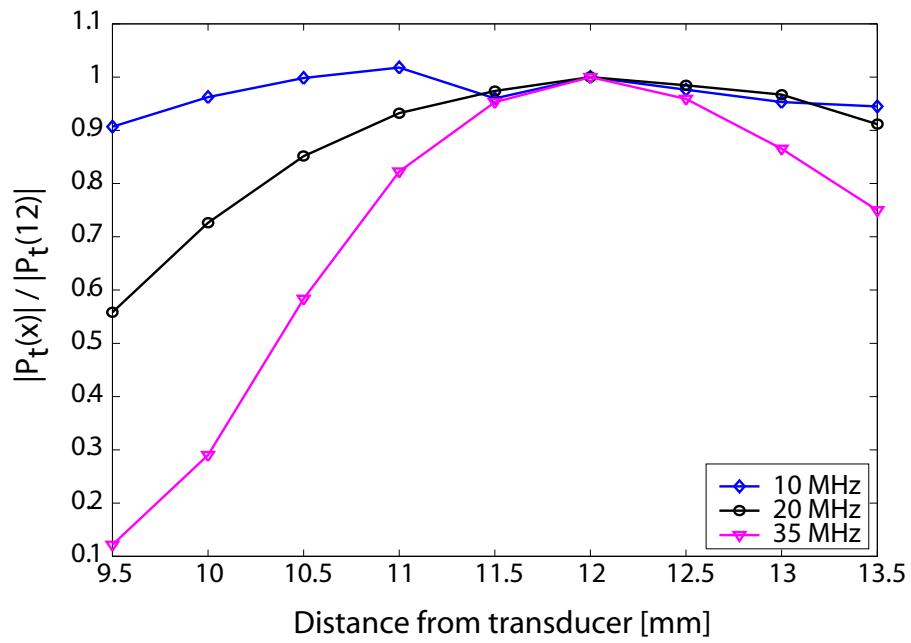


Figure 3.36: The pressure of the glass reference at the 10, 20 and 35 MHz frequencies as a function of transducer-sample length, normalized by the response at 12 mm.

appeared to stay flat from 11.5-12.5 mm. The impedance, which relates the reflection from the top surface to the reference echo, illustrates the focal region the most clearly. There was a clear peak at the nominal focal length and the impedance showed little variation from 11.5-13.5 mm. The plot of the frequency spectra for glass also supports a focal region from 11.5-12.5 mm. However, the lower frequencies show little variation at the larger distances, which suggests that for thicker samples the measurements should be analyzed over a lower frequency range.

The measurements for the SAM depend on the reflections from both the front and back surfaces, so the optimum position for the sample was chosen to be 11.5 mm, in order to bridge the 12 mm peak shown in the impedance plot. The 11.5 mm sample position, which corresponds to a time delay of $15.426 \mu\text{s}$ on the oscilloscope, was used for all of the measurements. The spectra of the reflection from the reference at 11.5 mm is presented in Fig. 3.37. The impact of the thickness of the sample on the measurements was not formally studied. The phantom molds (four, total) were designed to produce thicknesses ranging from 1-1.5 mm, but the nature of the phantoms was such that in actuality they exceeded the designed thickness and ranged anywhere from 1.2-2 mm. Among the phantom results, the impact of thickness was inconclusive, so samples up to 2 mm, the depth of the focal region, can be assumed to support the plane wave approximation.

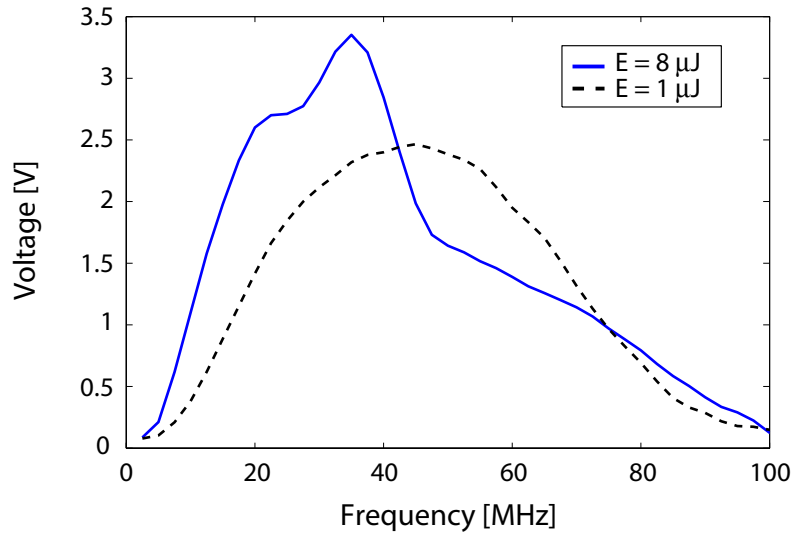


Figure 3.37: Frequency spectra from the reference at the 11.5 mm focal length.

3.6 Insonification Angle

It was important to explore how the angle of the transducer affected the measurements in the SAM, since the analysis is based on the assumption that the sound source is parallel to the sample surface. The effect of the angle becomes particularly important when working with *in vitro* tissue conditions, where the surface will rarely be flat. In order to determine the effect of the insonification angle on the measurement of the material properties, the reference data and analysis corresponded to normal incidence conditions. Refraction of the pulse was not accounted for under similar reasoning.

The table which the sample was measured on, shown in Fig. 3.3, was designed to be tilted over a range of $\pm 15^\circ$. The table was tilted by adjusting the length of the screws relative to the rigid platform. The mounting holes for the screws were angled to allow sufficient

rotation. A glass slide was placed on the table and the table height was adjusted to the focal length of 11.5 mm. The distance was set by moving the cursor on the oscilloscope to $t_1 = 15.426 \mu\text{s}$, the time the pulse takes to travel the roundtrip distance of 23 mm through water. With the surface positioned 11.5 mm from the transducer, the transducer was scanned some distance y along the y -axis, typically 6 mm. Due to the tilt the glass will have a new pulse-echo time $t_2(y)$ at the new position. The difference in the distance to the sample is given by $0.5c_2(t_1 - t_2(y))$. The angle in degrees was then determined by

$$\theta_{table} = \frac{180}{\pi} \tan^{-1} \left(\frac{c_{water} \cdot (|t_1 - t_2(y)|)}{2y} \right) \quad (3.4)$$

The effect of the insonification angle on the acoustic properties was determined using KP HDPE. The angle was varied by 0.5° increments until the signal from the back surface became too small after 5° . Considering the spot size of the beam at the focal length, measured at $200 \mu\text{m}$ [11], an angle of 5° causes the transducer to miss about 36% of the reflected signal.

The phase velocity at 25 MHz is plotted against the angle in Fig. 3.38. The normal incidence measurement had the highest value and the phase velocity decreased as the angle increased, with an overall drop in phase velocity of approximately 12 m/s. We expected the phase velocity to decrease since the distance which the pulse traveled increased with the angle but the sample thickness used in the analysis remained constant. However, the phase velocity remained relatively constant through 2.5° , staying within the standard deviation of the normal incidence phase velocity. Additionally, the standard deviation increased significantly for angles greater than 2.5° and the data was quite noisy past 30 MHz. After

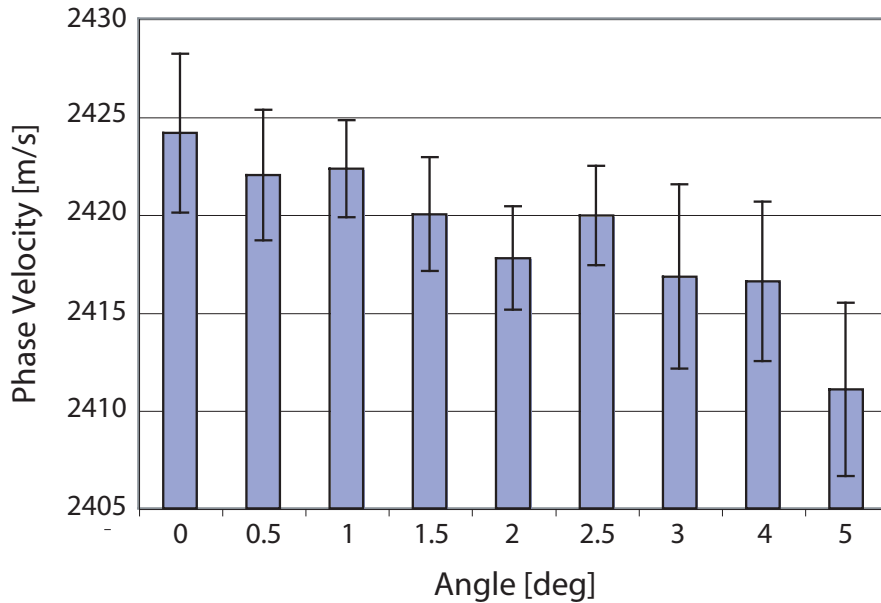


Figure 3.38: HDPE phase velocity as a function of angle of incidence relative to the normal at 25 MHz. The phase velocity decreased as the angle increased.

2.5° the time causal model did not match up well with the phase velocity.

The attenuation at 25 MHz for the range of angles is displayed in Fig. 3.39. The attenuation stayed constant for $\theta < 1.5^\circ$ and showed a monotonic increase with angle. The standard deviation of the measurement was relatively constant through 3° , after which it increases monotonically. Through 2.5° the deviation in the attenuation was within two standard deviations.

The impedance at 25 MHz is displayed in Fig. 3.40. The impedance remained relatively constant for $\theta < 3^\circ$, after which it decreased with the angle. The standard deviation was constant over the range of angles.

Based on these measurements the analysis appears to be valid for a variation of the

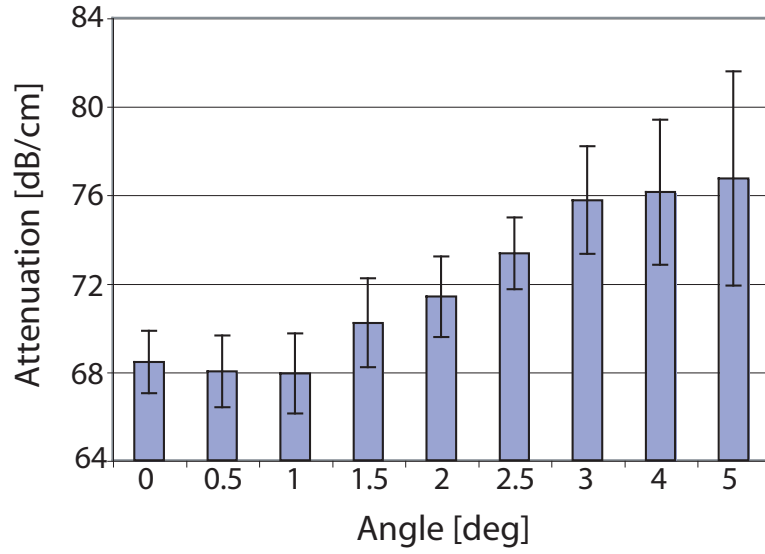


Figure 3.39: HDPE attenuation at 25 MHz as a function of angle of incidence relative to the normal.

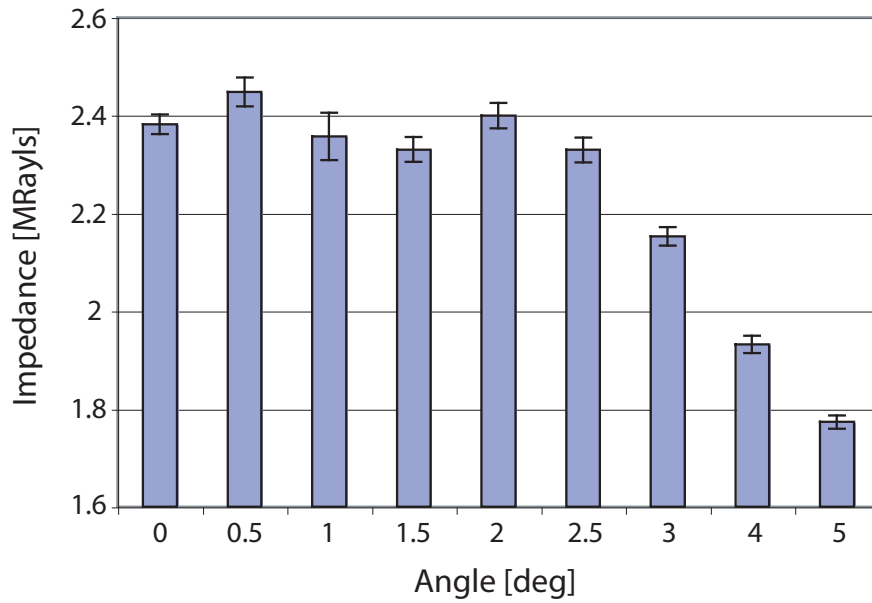


Figure 3.40: HDPE impedance at 25 MHz as a function of angle of incidence relative to the normal.

insonification angle up to 2.5° . The impedance seems to support a variation in angle up to 3° but the phase velocity and attenuation limit the range to $\pm 2.5^\circ$.

Chapter 4

Tissue Phantoms

In this chapter we present measurements of the acoustic properties of tissue mimicking phantoms with the SAM. The phantoms were chosen such that their acoustical properties would mimic those of blood vessels that are imaged with IVUS systems. Tissue-mimicking phantoms are widely used for research and commercial testing. The SAM was used to determine how each component of the recipe affected the acoustic properties of the phantom.

4.1 Phantom Recipe

A number of tissue recipes were examined for the SAM since physically and acoustically, the SAM phantoms had to satisfy a number of requirements. The phantoms had to have parallel, planar surfaces, and be between 1-2 mm in thickness. Acoustically, the phantom had to have phase velocity, attenuation and backscatter properties similar to human tissue. The recipes used in the SAM were adapted from documented recipes [40, 6, 33, 56] and were

varied to produce a range in the acoustic properties. The result was a set of recipes which yielded independent control over the impedance, attenuation, phase velocity, backscatter coefficient.

The phantoms were constructed from varying amounts of gelatin, agar, methyl paraben, silica, propanol and distilled water, and each ingredient played a key role in the properties of the phantom. The gelatin (Type A: from porcine skin, G-2625, Sigma-Aldrich Chemical Co.), was responsible for the stiffness in the phantom, and acted as a binder so that the phantom acted as a solid, homogeneous matrix. The agar (Agar-agar powder, A7002, Sigma-Aldrich Chemical Co.), which contributed to the stiffness as well, increased the melting point of the solid, which can be particularly important in cases when these phantoms are imaged at body temperature conditions of 37° C. The methyl paraben acted as a preservative. Propanol (n-Propanol, EW-88056, Cole-Parmer Instrument Co.) has been shown to increase sound speed. It was also noticed that propanol made dissolving the solid ingredients easier and that its contribution led to fewer bubbles in the degassing procedure. Distilled water was necessary for dissolving the rest of the ingredients.

Selecting a proper scatterer was important, since in the case of the SAM phantoms, the backscatter and attenuation depend on the size and type of scatterers. Over the course of the phantom development, several different scattering materials were considered. Diameter and settling rate were the driving factors in selecting a proper scatterer. Rayleigh scattering dictates that a scatterer diameter should be no larger than one-eighth the wavelength. For a top frequency of 35 MHz and a sound speed of 1550 m/s for human arteries the

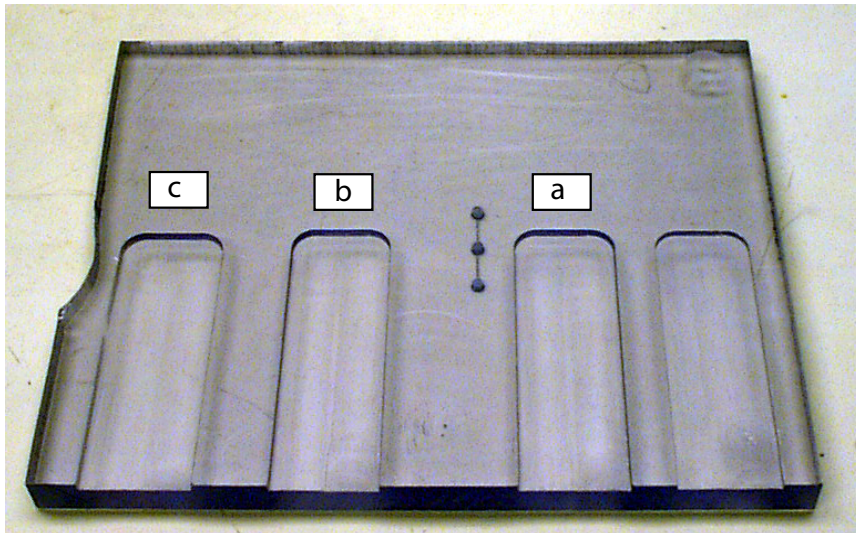


Figure 4.1: Molds used to construct the phantoms. The thickness varied, decreasing from left to right.

diameter should be no larger than $5.5 \mu\text{m}$. Graphite is a popular scatterer in the low MHz frequency range but was dismissed because a small enough diameter could not be located. Carborundum (SiC) was tested but was difficult to work with due to the fast settling rate of the particles; it was necessary to do snap freezing to prevent the carborundum from settling, resulting in an inhomogeneous phantom otherwise. Silicon dioxide (SiO_2 , S5631, Sigma-Aldrich Chemical Co.) was selected and proved easy to work with while providing decent attenuation and scattering properties. The particle diameter was listed as varying between $0.5\text{-}10\mu\text{m}$ with approximately 80% of the particles between $1\text{-}5 \mu\text{m}$ in diameter.

The phantoms were constructed in three molds of varying thickness, shown in Fig. 4.1. The phantoms were constructed on a glass slide, which provided two advantages: the rigid backing of the slide prevented the phantom from sagging and the high impedance of the glass provided a strong reflection from the back surface of the phantom. Therefore, the

molds were machined to the footprint of a glass slide (2.54 x 7.62 cm) and to thicknesses varying from 2.20, 2.30, 2.60 mm, taking into account the thickness of the slide (0.98 mm). As shown in Fig. 4.1, the molds were referred to as *a*, *b* and *c*, respectively, for phantom identification in the measurements. The mold on the far right proved to be too thin to produce a workable phantom so only the three thickest molds were used. So, before the phantoms were poured into the mold, a single slide was placed in each mold and the liquid phantom was poured onto the glass slide. An acrylic sheet with a similar footprint to that of the mold was used to cover the phantoms for the duration of the setting to prevent the phantoms from drying out. Once the phantom set it naturally adhered to the slide and the phantom/slide couple could easily be removed from the mold.

4.2 Construction Protocol

Table 4.1 gives the basic recipe used in phantom construction, based on a total mass of 100 g. The actual concentrations were adjusted depending on the desired outcome.

Table 4.1: Basic phantom recipe, by percent weight

Silica	Gelatin	Agar	Methyl Paraben	Propanol	Water
6	15	4	0.2	2	72.8

The water and propanol are mixed and then degassed, and all of the dry ingredients, with the exception of the silica, are weighed and set aside. After degassing for 20 mins, about 20 g of the water/propanol mixture should be set aside and covered, to prevent evaporation. This amount will be used to mix in with the silica particles later in the process, in order to create

a liquid/silica slurry. The liquid to scatterer ratio for the slurry should be approximately 3:1. The water/propanol mixture is heated to 30° C and the gelatin is mixed in. While care should be taken throughout the entire process to avoid the introduction of bubbles, bubbles are inevitable in several of these steps, especially when adding the gelatin. The gelatin bloom rating indicates the relative length of the polymer chains, and 175 bloom gelatin was used in the phantoms. The gelatin particles tend to bind together when first wetted, so this step of the procedure can be the most difficult. Gelatin should be added at a colder temperature (30° C) and, once in solution, will contain several bubbles. The bubbles should not be a concern but any remaining particle clumps should be broken up and dissolved. In recipes employing smaller amounts of water and propanol, adding the gelatin can be difficult. Once the gelatin has been dissolved, the mixture is heated to 90° C, and should be stirred occasionally to avoid burning of the mixture. At 90° C, the melting point of agar, the agar is mixed in, along with the methyl paraben. The higher the temperature, the easier the agar will dissolve. At this stage, there should be few bubbles in the mixture, but it is possible there will be some on the surface. The mixture should be removed from heat (for the short duration of the next step; for greater periods of time, the mixture should be kept at a minimum of 30° C), and the remaining water that had been set aside should be mixed with the silica particles. Since the silica is a scatterer, it will not fully dissolve, hence the need to make a slurry of the particles. In order to prevent settling, the slurry should be stirred well enough to ensure a uniform concentration; the propensity of the silica particles to settle is the main reason why this step is left towards the end of the process.

The slurry is then mixed into the rest of the mixture and the entire mixture is poured into a degassing flask with a magnetic stir bar. For the degassing step the mixture was heated at a temperature of 30° C, and was degassed at a negative pressure of one atmosphere for approximately 30 mins. By the end of the degassing there should not be any visible bubbles.

Once the phantom is fully degassed it is poured into the mold, with the glass slides in place, and is allowed to sit for about 20 s to allow any bubbles introduced in the pouring to rise to the surface of the still-warm phantom. Next the acrylic sheet is placed over and clamped to the mold. Once the mold is clamped down it is placed in a freezer for five minutes and then transferred to a refrigerator to set. After four hours the phantom should be workable and should appear as a white opaque rubbery material. Since they are constructed on the glass slide, the phantoms are removed from the mold by sliding out the glass slide with the phantom mounted on top.

One of the problems with the phantoms is that they swell when submerged in water. The swelling not only changes the thickness over time but also deteriorates the surface reflection quality. There are methods to address this problem: one is to enclose the phantom in a thin, near acoustically-transparent material such as Saran Wrap [6] or a plastic membrane [40, 56], a second method is to treat the phantom surface chemically [56] and a third is to store the phantom in oil. We wanted to avoid introducing an extra layer into the measurement, so 50% concentration glutaraldehyde was used to treat the surface [56]. The phantom is submerged in glutaraldehyde for no longer than five minutes and then rinsed in distilled water; it was noticed that longer submersion times caused the phantom

to curl at the corners and separate from the glass slide. Glutaraldehyde cross-links the surface and acts as a stabilizer; this process is visible by a change in color, from white to a yellowy-orange color. The glutaraldehyde was used to treat the phantoms in the silica variation studies but not for the propanol or gelatin variation studies. It was determined, by comparing results with and without the glutaraldehyde treatment, that the treatment did not affect the surface acoustic properties.

For the measurements carried out here the phantoms remained attached to the glass slide, but after prolonged water submersion the phantom could become detached. This attachment was verified either by looking at the bottom of the phantom, to check for air bubbles, or by looking at the signal reflected from the back of the phantom. The response should initially be a sharp, high voltage, since glass has a high impedance mismatch with the phantom material. If there is a small signal preceding this high signal, it can be assumed there is water in between the phantom and the glass slide. When the phantom became detached from the glass it was discarded.

4.3 Phantom Scan

The phantoms were always poured into the molds in the same order, starting with the a mold, then the b and c molds; this order corresponded with the thickness of the molds, where a was the thinnest, followed by b and c . The scans were performed in the same order. The glutaraldehyde treatment prevented most of the swelling, but some swelling still occurred when the phantom was immersed in water. By plotting a surface contour plot of

the arrival time of the pulse to the top surface of the phantom it was possible to track the swelling of the phantom over time. There was a clear trend of a decreasing arrival time with respect to the sequence of the raster scan. The bulk of the swelling appeared to take place during the first five minutes of water immersion, so the phantoms were immersed in water for five minutes after the glutaraldehyde treatment. Therefore, after the phantoms were removed from refrigeration and once the cover of the mold was removed, the *a* phantom was soaked in the glutaraldehyde, rinsed, and immersed in water and scanned. The *b* and *c* phantoms followed in the same order. For the majority of the experiments, the thickness measurements of the phantoms corresponded with the thickness of the molds, and a surface contour plot of the arrival time of the pulse to the top surface of the phantom showed a marked improvement when compared to the phantoms without the glutaraldehyde treatment.

The procedure for the phantom scan was slightly different from the scan procedure for the polyethylene materials. The phantoms were constructed on a uniform, rectangular glass slide, so the phantoms were fit in the right-angle groove in the table for the scan. The groove made it possible to remove the phantom and return it to the same location. This capability allowed us to measure the thickness of the phantom more accurately (described in full detail in the 'Thickness Measurements' paragraph in Sec. 3.1): once the phantom was first scanned for the phase velocity and attenuation measurements, the phantom was removed and replaced by an identical clean spare glass slide. The slide was measured for the time of arrival data, which was saved with the rest of the scan data. The spare slide was

then replaced by the phantom, which was next scanned for the backscatter measurements, using the point-by-point scan.

4.4 Results

The concentration of each of the phantom ingredients was varied in order to examine the resulting effect on the material acoustic properties. The literature reports [6, 40] that the scattering particle content should have a direct effect on the attenuation and backscatter coefficient but not the phase velocity. The propanol was reported to change the phase velocity. We examined the effect of the concentration of gelatin and agar on the properties as well.

For each recipe at least two batches were made using molds *a-c*. Occasionally however a glass slide would break upon removal from the mold so some of the batches only had two surviving phantoms.

The phantoms were tested with a glass backing and therefore the reflection from the back surface $p_b(t)$ had a higher amplitude than was the case for the water backed polyethylene samples. We found that the frequency band with adequate signal-to-noise ratio was 15-40 MHz for the phantom measurements.

4.4.1 Base recipe

The base recipe shown in Table 4.1 was thoroughly characterized for the impedance, attenuation, phase velocity and backscatter coefficient and the time causal model was used

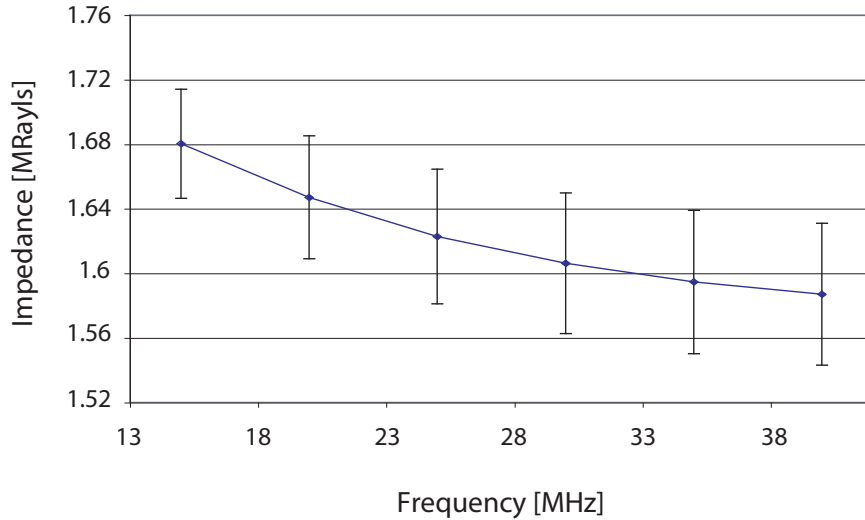


Figure 4.2: Specific acoustic impedance for the base phantom recipe.

to validate the dispersion in the phase velocity. The impedance results are displayed in Fig. 4.2. The impedance decreased from 1.68 to 1.59 MRayls and the standard deviation increased from 0.03 to 0.04 MRayls over the 15-40 MHz range. From the $Z(f) = \rho c(f)$ relationship we expected the impedance to increase with frequency since we expected the sound speed to increase slightly with frequency due to dispersion effects. The density should remain constant with frequency. The impedance for the basic recipe was slightly high compared to the literature value of 1.55 MRayls for tissue [35].

The attenuation of the base recipe is shown in Fig. 4.3. The attenuation increased from 18.19 to 65.77 dB/cm with a standard deviation which increased from 0.7 to 2.1 dB/cm over the 15-40 MHz range, following the expected power law of $n = 1$ [36, 40]. The literature values for attenuation in tissue at 25 MHz are approximately 33 dB/cm [35], so the attenuation in the base recipe is appropriate for human arterial tissue.

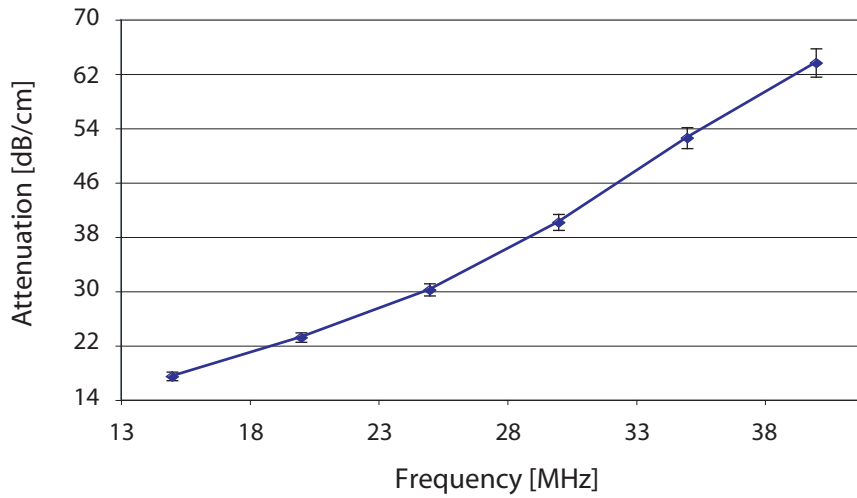


Figure 4.3: Attenuation for the base phantom recipe.

Figure 4.4 displays the phase velocity for the base recipe. The phase velocity exhibited some dispersion, increasing from 1368.1 to 1370 m/s and the standard deviation decreased from 7.7 to 2.5 m/s over the 15-40 MHz range. The time causal model prediction was very similar to the measured results and was within the standard error of the measurement.

The backscatter coefficient of the base recipe is presented in Fig. 4.5. The plot reveals a trend similar to the expected f^4 slope. The backscatter coefficient increased from 3 to 39 $\times 10^{-3}$ (mm Sr) $^{-1}$, which was low compared to the literature value of 0.4 (mm Sr) $^{-1}$ for the femoral artery at 30 MHz [36].

4.4.2 Silica variation

The effect of the silica content was studied by measuring three concentrations of the silica: 2, 6 and 10%. The recipe is presented in Table 4.2.

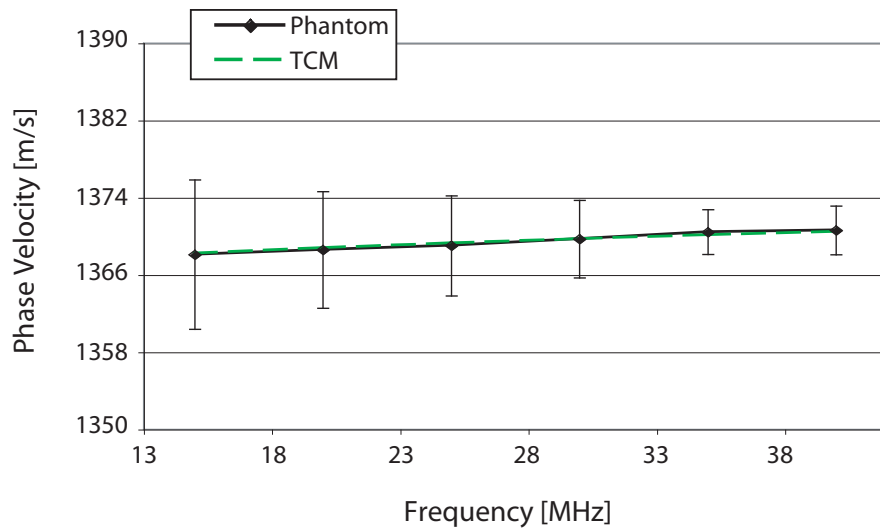


Figure 4.4: Phase velocity for the base phantom recipe. The time causal model matched the measured results.

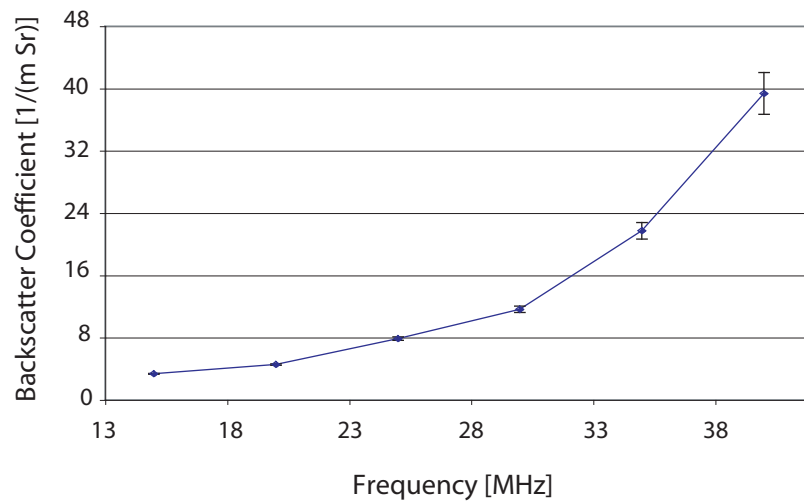


Figure 4.5: Backscatter coefficient for the base phantom recipe.

Table 4.2: Phantom recipes for silica studies, by percent weight

Silica	Gelatin	Agar	Methyl Paraben	Propanol	Water
2	15	4	0.2	2	76.8
6	15	4	0.2	2	72.8
10	15	4	0.2	2	68.8

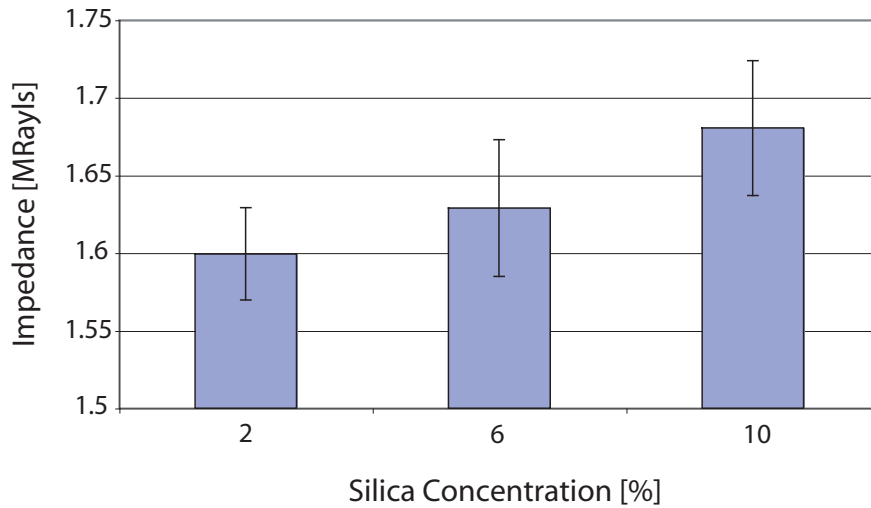


Figure 4.6: Specific acoustic impedance for the three silica concentrations at 25 MHz.

Figure 4.6 shows the mean impedance for the three silica concentrations at 25 MHz. We expected that the silica concentration would chiefly affect the attenuation and backscatter coefficient results, but the silica content had an impact on the impedance as well. The impedance was 1.60, 1.63 and 1.68 MRayls at 25 MHz for the 2, 6 and 10% silica concentrations, respectively. The standard deviation varied from 0.03-0.04 MRayls but showed no correlation with silica content.

The attenuation results for the 2% silica phantom at 25 MHz are presented in Fig. 4.7. The standard deviation of the attenuation across the sample is plotted, along with

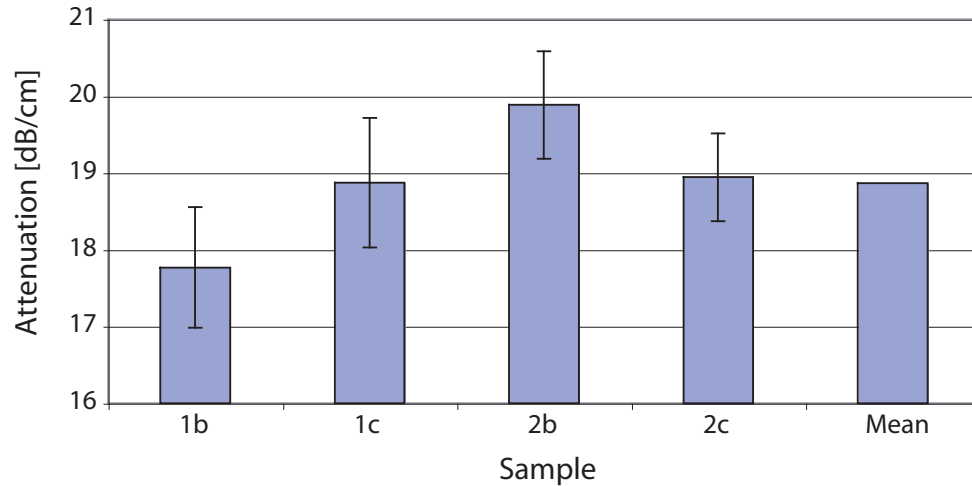


Figure 4.7: Attenuation for the 2% silica phantoms at 25 MHz.

the mean of the four sets of results. The samples ranged from 17.77-19.88 dB/cm with a mean attenuation of 18.87 dB/cm and a relatively constant standard deviation around 0.7 dB/cm.

The attenuation results for the 6% silica phantoms at 25 MHz are shown in Fig. 4.8.

The first batch had a slightly higher attenuation than the second batch but the overall variation was small. The 6% silica phantoms range from 30.2 to 31.5 dB/cm, with a mean attenuation of 30.94 dB/cm and relatively constant standard deviation of 0.9 dB/cm.

The attenuation for the 10% silica phantoms is shown at 25 MHz in Fig 4.9. The three batches ranged from 38.98 to 47.86 dB/cm, with a mean of 45.30 dB/cm. The standard deviations were slightly higher than the other silica phantoms as well, ranging from 1.1-1.5 dB/cm. The eight phantoms varied by 4.3 dB/cm but within the batches showed little variation, with the exception of the second batch. The particles do settle in solution, so it is

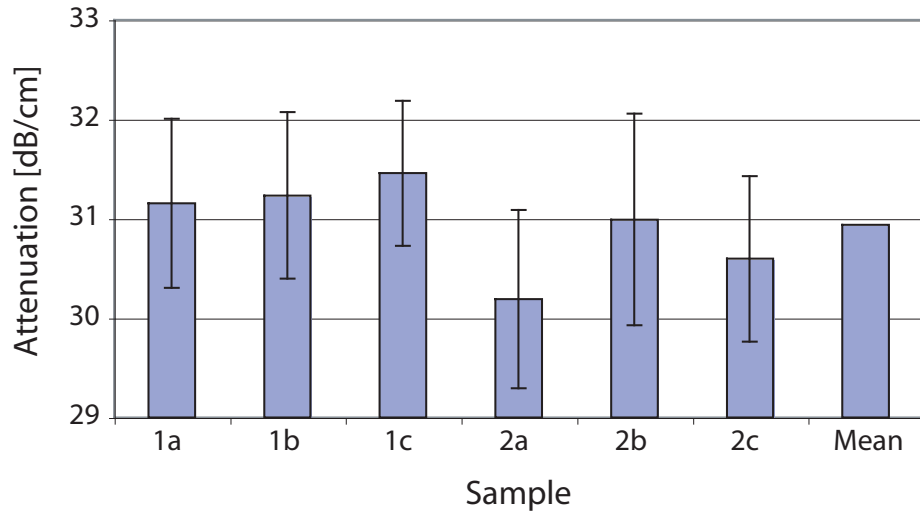


Figure 4.8: Attenuation for the 6% silica phantoms at 25 MHz.

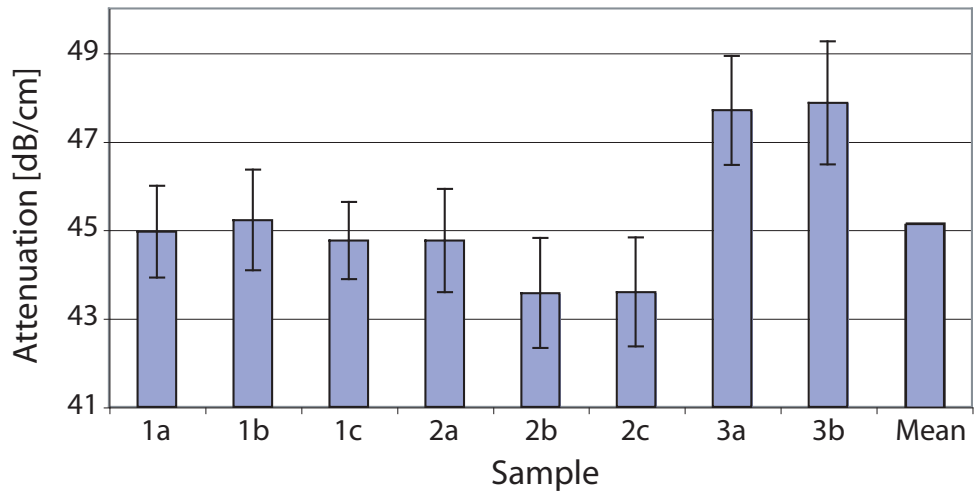


Figure 4.9: Attenuation for the 10% silica phantoms at 25 MHz.

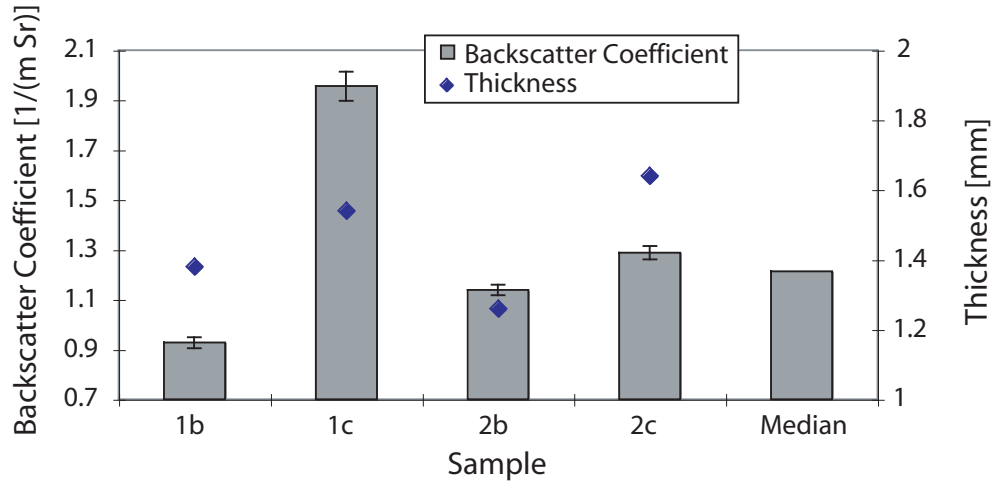


Figure 4.10: Backscatter coefficient and thickness for the 2% silica phantoms at 25 MHz.

possible that from batch to batch the actual silica concentration changed once the phantom was poured in the mold. The final silica concentration most likely varied more in the higher concentration phantoms.

The mean power law exponents for the three concentrations did not show a correlation with the increase in silica concentration as the exponent y for the 2, 6 and 10% silica phantoms was 1.47, 1.53 and 1.52, respectively.

The variation in silica content did not show any clear affect on the phase velocity.

The BC for the 2% silica phantoms at 25 MHz is plotted in Fig. 4.10 with the sample thickness. The BC ranged from 0.93 - 1.96 (m Sr)⁻¹ and the median was 1.21 (m Sr)⁻¹. Due to the uneven distribution, the median was a better estimate of the BC of the samples rather than the mean. The standard deviation was highest for the *1c* sample, which had the highest BC, and was smallest for the *2b* sample. In the majority of the phantoms, the

standard deviation showed a correlation with the amplitude of the BC and was generally two orders of magnitude smaller than the BC. We expected that the BC would show some proportionality to the attenuation, based on the number of scatterers in the phantom, but this was not the case within the batches of silica concentrations. Rather, the BC showed a stronger correlation with the thickness of the sample within each particular batch. Figure 4.10 shows that the BC was higher for $1c$ and $2c$, both of which are thicker than the b phantom in their respective batch. The attenuation in $1c$ was higher than in $1b$ but the same is not true for the second batch. The BC was calculated from the same data window length for all of the phantoms, so a correlation with the thickness was not expected. Indeed, an increase in the BC with the thickness would suggest that the thicker samples contained more scattering particles. Since the thicker samples were poured from the same liquid phantom batch as the thinner samples, this explanation must be ruled out.

An additional mechanism which must be examined is the effect of the settling of the scattering particles. If particle settling were indeed an issue (caution was taken to cool the phantom as quickly as possible to avoid settling) the overall apparent attenuation of the wave would be the same, as the beam would transmit through the same number of particles. The material density throughout the phantom, however, would be slightly affected, which could in turn affect the acoustic impedance. However, the region of measurement for the BC is different from the other properties, as only the top portion of the phantom is measured for an echo, the length of which is constant throughout the experiments. Any settling action would cause a lower number density of particles in the top portion, so the BC would

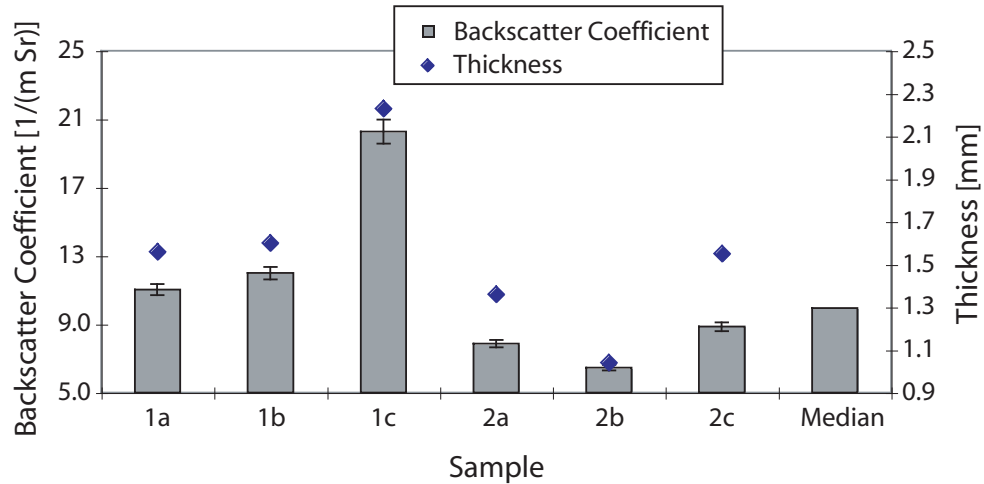


Figure 4.11: Backscatter coefficient and thickness for the 6% silica phantoms at 25 MHz.

effectively be lower. If we assume that the thicker phantoms take longer to cool (i.e., set) then the thicker phantoms should have a lower number density of particles in the top region of the phantom when compared to the thinner phantoms. If this were the case, however, we would expect an inverse relationship between the phantom thickness and BC, which contradicts our experimental results. As a result, an explanation of the correlation of the thickness to the BC is unclear. A future experiment to examine the effect of particle settling could be to remove the phantom from its glass backing and measure it upside-down, with the bottom of the phantom facing the transducer. Additional future experiments related to this issue should include a rigorous study of the effect of the phantom thickness on the acoustic properties.

The BC at 25 MHz and the thickness of the 6% silica phantoms is plotted in Fig. 4.11. The samples ranged from 6.46 to 12 (m Sr)⁻¹ with the exception of the *1c* sample, which

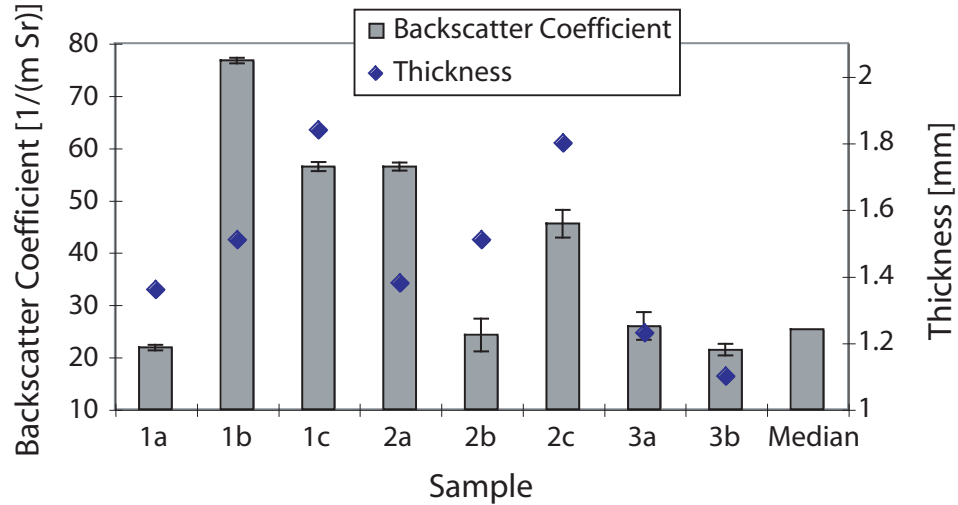


Figure 4.12: Backscatter coefficient and thickness for the 10% silica phantoms at 25 MHz.

was much higher, at 20.3 (m Sr)^{-1} . The median BC was 9.94 (m Sr)^{-1} . The 6% silica phantoms had a strong correlation with the thickness as well, which could explain the high BC for the *1c* phantom.

The BC for the 10% silica phantoms, plotted at 25 MHz in Fig. 4.12, shows the most spread of the silica phantoms. The BC ranged from 15.1 to 76.7 (m Sr)^{-1} with a median value of 25.3 (m Sr)^{-1} . The 10% silica phantoms had the most variation of the three concentrations but there was no correlation with the sample thickness, with the exception of the third batch.

The mean of the attenuation and backscatter coefficient for the three silica concentrations is presented in Fig. 4.13. The plot clearly shows that both the attenuation and backscatter coefficient increase with the silica concentration. The attenuation appears to have a linear increase with the silica concentration.

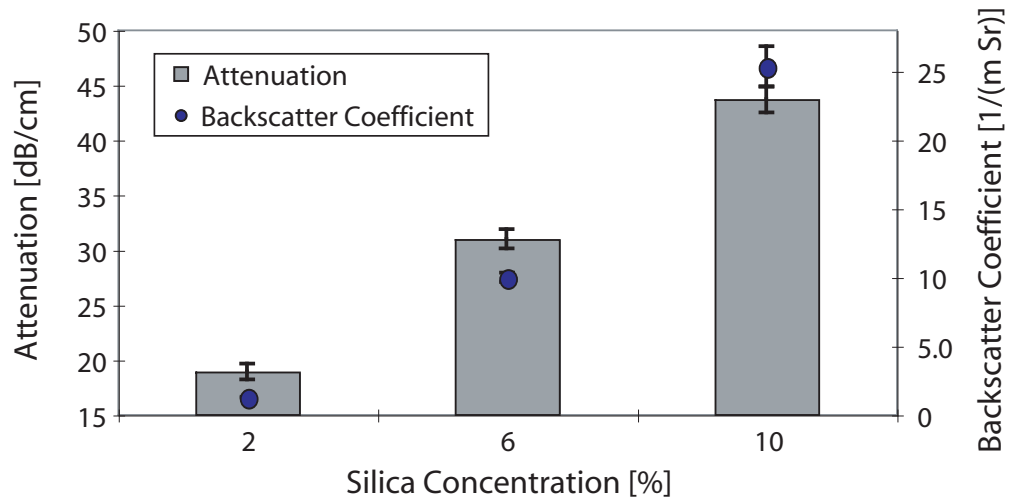


Figure 4.13: Mean attenuation and backscatter coefficient for the three silica concentrations at 25 MHz. Both the attenuation and the backscatter coefficient increased with the silica concentration.

4.4.3 Propanol variation

It has been documented that propanol has the effect of changing the sound speed in tissue phantoms [6, 40]. Burlew [6] showed an increase from 1500-1595 m/s, approximately, for a 0-20% concentration of propanol, by weight, so propanol concentrations of 0, 8 and 12% were used. The three recipes are shown in Table 4.3.

Table 4.3: Phantom recipes for propanol variation studies, by percent weight

Propanol	Gelatin	Agar	Methyl Paraben	Silica	Water
0	15	4	0.2	6	74.8
8	15	4	0.2	6	66.8
12	15	4	0.2	6	62.8

Adding propanol to the recipe presented some difficulties. Normally the liquid ingredients were degassed before the solution was heated and the gelatin added. However,

we noticed that after the phantom was made, the water in the degassing tank smelled of propanol and had an oily feel, giving the impression that propanol was removed from solution during the degassing process. First we checked to see if the propanol was being boiled away, but the boiling point of propanol is 97°C and the highest temperature during the construction process was 90°C . The highest pressure during the procedure was approximately one atmosphere of vacuum (the corresponding temperature at this step was approximately 30°C), which corresponds to a vapor pressure for propanol of 28.97 mmHg and 31.82 mmHg for water [50]. The procedure was changed, so that the propanol was not added until the final degassing step, but the tank water still showed traces of propanol. Therefore, it is possible that the final concentration of propanol was lower than expected.

The phase velocity of the three propanol batches at 25 MHz is plotted in Fig. 4.14 and

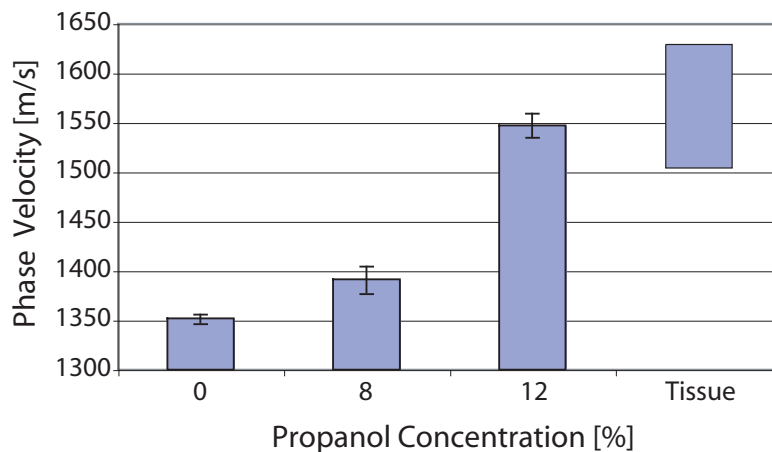


Figure 4.14: Mean phase velocity for the propanol phantoms at 25 MHz. The phase velocity was expected to increase with an increase in propanol concentration. The range for the phase velocity in human arteries is included for reference.

similar to other reports, the phase velocity showed an overall increase with an increase in

propanol concentration. There was some variation in the results within each phantom batch, but the mean of the results supports the expected increase. The 0% propanol phantoms ranged from 1304.14-1393.04 m/s at 25 MHz with a mean phase velocity of 1351.79 m/s. The 8% propanol phantoms were more consistent, ranging from 1359.87-1429.19 m/s at 25 MHz, and the mean was 1391.20 m/s. The 12% propanol phantoms had the highest phase velocity, ranging from 1505.40-1588.55 m/s at 25 MHz. The mean was 1546.98 m/s. The uncertainty of the measurement for the three phantoms in each concentration increased slightly with the increase in propanol: the uncertainty was 14.8, 15.7 and 18 m/s for the 0, 8 and 12% propanol phantoms, respectively. The range for human tissue, as referenced in Table 1.2, is plotted as well.

Both Burlew and Madsen [6, 40] report a larger increase in sound speed for the increase of propanol which we used in our phantoms. However, it is difficult to compare our results for the variation in propanol with those in the literature since our base phantom recipe is different from the literature recipes. We suspect that the sound speed is not completely dependent on the propanol concentration and that the rest of the ingredients play a role in the speed of sound through the phantom. The sound speed did increase with the concentration of propanol and the 12% propanol concentration matched the documented sound speed for human arteries. The dispersion predicted by the time causal model matched the slope of the phase velocity for each phantom. The impedance, attenuation and backscatter coefficient showed no effects from the variation of propanol concentration.

4.4.4 Gelatin variation

The concentration of the gelatin was varied in 5% increments from 10-25%, shown in Table 4.4. The only difficulty in the construction of the gelatin phantoms came in the higher concentrations, due to the corresponding low concentration of water. The phantoms were noticeably stiffer at the higher concentrations.

Table 4.4: Phantom recipes for gelatin variation studies, by percent weight

Gelatin	Agar	Methy Paraben	Silica	Propanol	Water
10	4	0.2	6	8	71.8
15	4	0.2	6	8	66.8
20	4	0.2	6	8	61.8
25	4	0.2	6	8	56.8

The mean phase velocity for each concentration is plotted in Fig. 4.15. There is

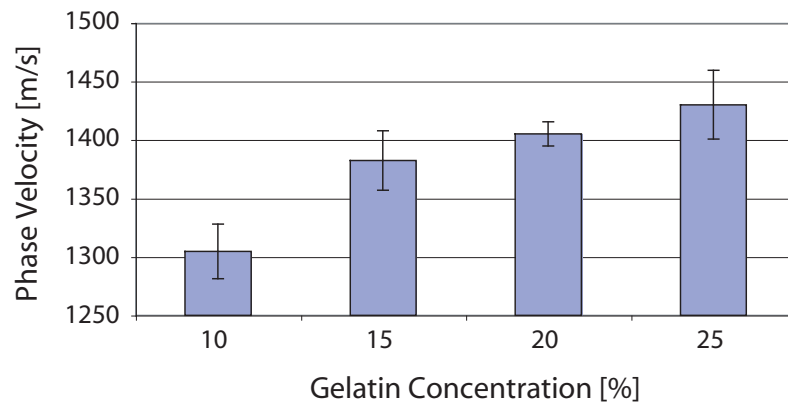


Figure 4.15: Mean phase velocity for the four gelatin concentrations at 25 MHz.

a noticeable increase in phase velocity with increasing gelatin concentration. The lowest concentration phantoms, the 10% gelatin, had the lowest mean phase velocity, at 1343.12 m/s, and the highest concentration, 25% gelatin, had the highest phase velocity of the four

concentrations, averaging to be 1444.11 m/s at 25 MHz. The 15% and 20% gelatin phantoms had similar mean phase velocities, 1391.20 and 1394.52 m/s, respectively. The error bars for the phantoms represent the uncertainty of the three phantom measurements for each concentration. The uncertainty increased with the gelatin concentration, from 23.3 to 29.4 m/s. Note that the 20% gelatin phantoms had a lower uncertainty, 10.4 m/s. The variation in gelatin study was conducted early on in the phantom experiments and due to data loss, the 20% gelatin phantoms had to be remade at a later date. One of the improvements in the phantom studies which we made was the method which we used to measure the thickness of the phantom. The 10, 15 and 25% gelatin phantom thicknesses were measured by hand with a pair of calipers, while the 20% gelatin phantoms were measured using the time-of-flight method (described in the Thickness Measurement paragraph in Sec. 3.1), and as a result, the standard deviation decreased dramatically using this alternate method of measuring the thickness.

The effect of gelatin content on attenuation of the samples at 25 MHz is shown in Fig. 4.16. There was a general increase in attenuation with the gelatin concentration with a peak value for the 20% gelatin phantom. The attenuation for the four concentrations at 25 MHz was 25.58, 29.14, 40.51 and 35.98 dB/cm, respectively.

One possible explanation for the higher attenuation in the 20% gelatin phantom was that a different technique for adding the silica into solution was used in an attempt to prevent loss of the particles in the transfer to solution. Previously, the silica particles were immersed in water before the rest of the ingredients had been dissolved and stirred

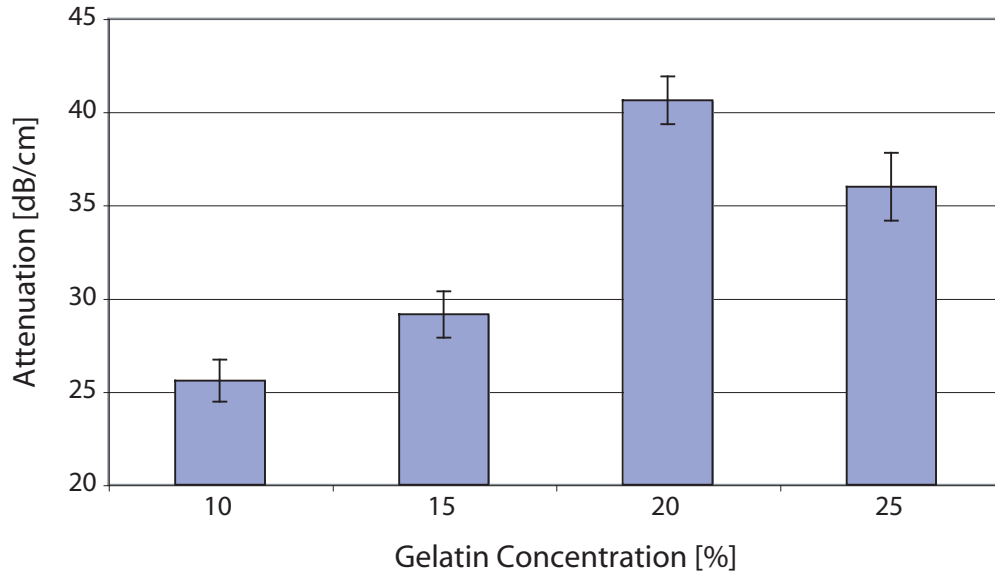


Figure 4.16: Mean attenuation for the four gelatin concentrations at 25 MHz.

occasionally until the particle and water mix was added to the rest of the phantom mix before the final degassing step. This meant that the particles had time to settle while the rest of the phantom construction steps were being carried out. In the case of the 20% gelatin phantom (which had to be remade at a later date, see above), the silica particles were not immersed in water until just before the final degassing step, giving them much less settling time (as described in Sec. 4.2). Therefore, we suspect that the 20% gelatin phantom had an actual silica percentage closer to the recipe than the other phantoms. The difference in these two methods belies one of the difficulties in constructing phantoms, as the phantom does not necessarily reflect the intended proportions of the recipe. Unfortunately, time did not permit us to redo the other gelatin phantoms. However, only the 10, 15 and 25% gelatin phantoms were constructed using the older method of adding in the silica particles; all of

the other phantoms presented here were constructed using the newer method.

The impedance did not show a dependence on the gelatin concentration. The backscatter analysis had not been developed by the time the gelatin variation measurements were performed so the effect of the gelatin concentration on the backscatter coefficient is unknown.

4.4.5 Agar variation

The effect of the agar concentration was examined by varying the concentration in 2% increments from 2-6%. However there was no correlation of the agar concentration with any of the acoustic properties.

By increasing the concentration of the silica the attenuation and backscatter coefficient were increased. Unexpectedly, the impedance showed a weak dependence on the silica concentration as well. An increase in the gelatin concentration produced a slight increase in the sound speed and attenuation. Finally, the propanol concentration affected the phase velocity, boosting the phase velocity by a maximum of 254 m/s for a 12% increase in the concentration of propanol.

Chapter 5

Tissue Measurements

The SAM was used to measure the acoustic properties of one human specimen. The specimen was a femoral artery provided by Dr. Marvin Doyley at Dartmouth College. No information about the subject was available and the artery was believed to be healthy. The theory and analysis was modified from that presented in Chapter 2 due to the layered nature of the tissue.

5.1 Measurement

The artery was approximately 130 mm long and 7.4 mm in diameter and had been preserved in 10% formalin. The artery was sliced down the lumen axis and unrolled so it lay flat, as shown in Fig. 5.1. The surface appeared to be smooth and rubbery and void of calcifications or lesions. The thickness of the artery was difficult to measure since the surface would compress and spring back to its normal state when pressed. The surface thickness was

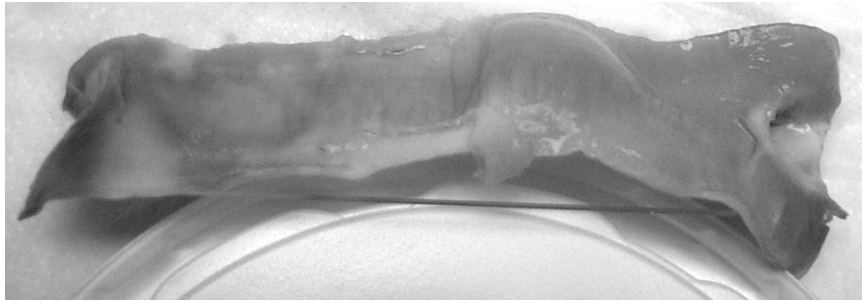


Figure 5.1: Femoral artery used for the SAM measurements. The artery measured approximately 130 mm in length and 12 mm in width.

measured similarly to the polyethylene samples, in eight different locations with a pair of calipers, with an average thickness of 1.72 mm.

The sample was mounted so that the pulse from the SAM would be incident on the intima (this is the orientation that would be used in an IVUS system). The sample was water backed and this was achieved by stretching the artery over a washer (38.33 mm OD, 10.30 mm ID, 1.26 mm thick) and then using clamps to hold the artery taut. This setup initially provided a flat surface but the artery demonstrated creep over the course of a measurement; that is, the sample would sag axially and curl in the radial direction. The surface therefore was not necessarily normal to the transducer axis; periodically, between scans, the artery was reclamped in order to keep the surface flat. Multiple 2 x 2 mm regions were scanned over a two-day period and the tissue was kept refrigerated when it was not being measured. Towards the end of the two days, the top layers of the artery showed some wear and became separated from the adventitial layer. Figure 5.2 shows the separation of the layers, as well as the curvature in the surface.

Five regions were measured on the first day and four regions were measured on the

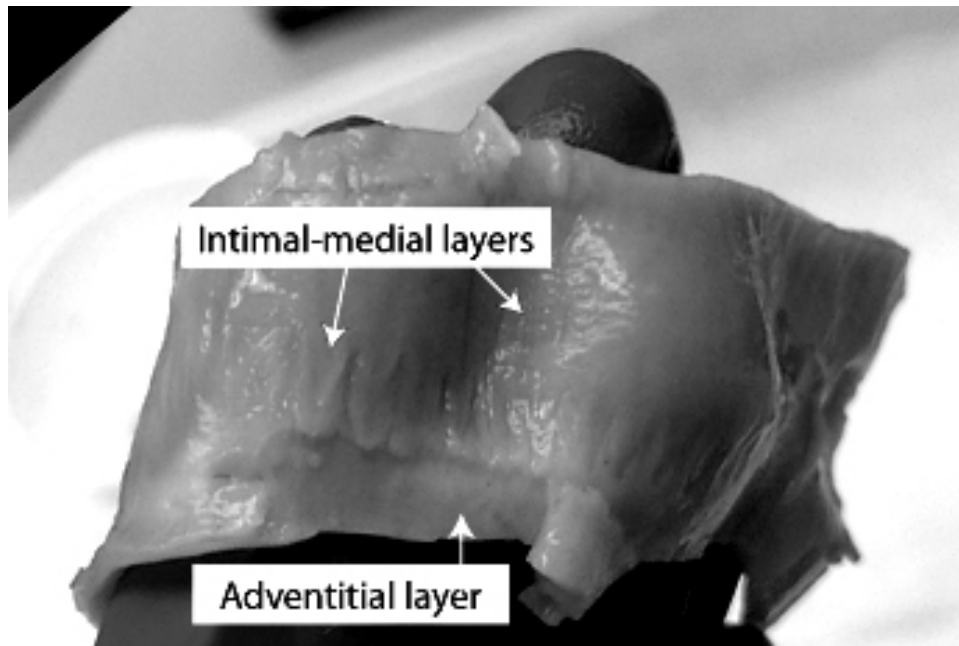


Figure 5.2: The femoral artery. The intimal-medial layers and the adventitial layer became separated after being clamped and were visible to the eye.

second day. We noticed that capturing all of the reflections in a single window, as opposed to the multiple windows used for the top and bottom reflections in the polyethylene and phantom measurements, made it easier to identify the regions of the tissue which we were seeing in the received echo, as the reflections were not as clearly distinguished from the noise level as in the polyethylene and phantom experiments. In addition, capturing all of the echoes in one window allowed us to more easily distinguish the relative peak amplitudes of the tissue layers and therefore adapt the analysis code to search for the proper area for the peak detection. Of the nine measurements, only four of the data sets held good data. Three of the datasets were from the first day, *1b*, *1d*, *1f*, and one was from the second day, *2a*. The data was captured using the same pulser/receiver settings as in the previous

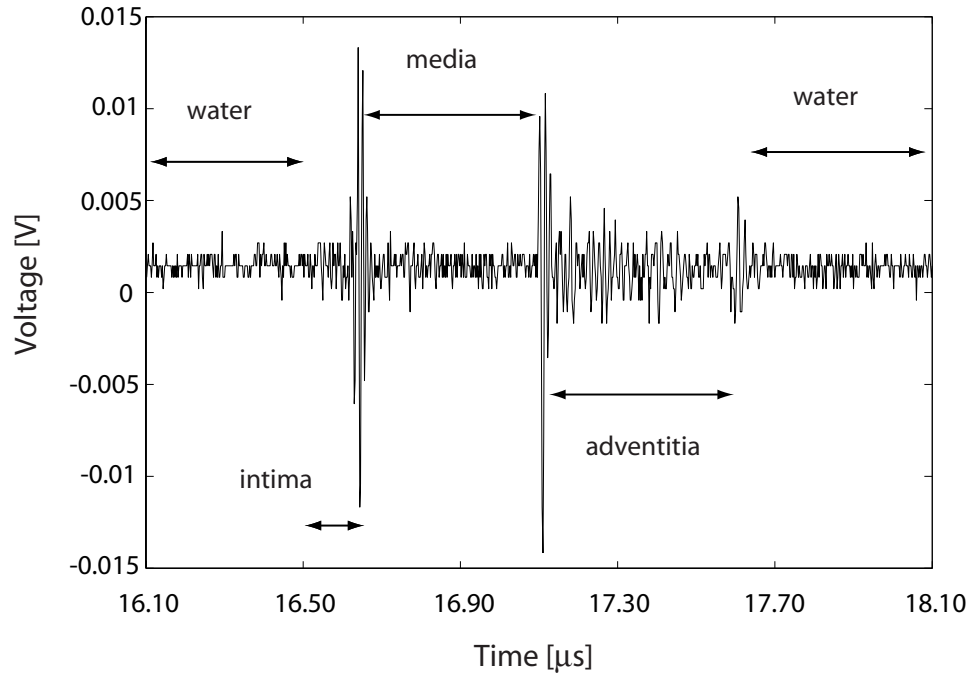


Figure 5.3: The signal from the artery in a ‘good’ region. The echoes from the intima-media, media-adventitia and adventitia-water boundaries are clearly visible, delineating each layer. The adventitial layer features more backscatter than the other layers.

polyethylene and phantom experiments: the impedance was measured using $E = 1 \mu\text{J}$ and $A = 12 \text{ dB}$ and the other properties were measured using the higher energy settings, $E = 8 \mu\text{J}$ and $A = 19 \text{ dB}$.

The waveform shown in Fig. 5.3 is representative of a ‘good’ echo signal measured from the artery. The signal from the intima appears to start around $16.50 \mu\text{s}$. There is no clear interface signal but there does appear to be an increase in backscatter. This is consistent with other data in the literature which indicates that a healthy intima is thin and difficult to detect acoustically [35, 36, 67]. We interpreted the signal at $16.70 \mu\text{s}$ as the intima-media boundary. The signal from within the media shows little backscatter

which is also consistent with reports in the literature [35, 36, 67]. The signal at $17.10 \mu\text{s}$ was interpreted as coming from the media-adventitia boundary. The signal from within the adventitia showed clear backscatter, again consistent with the literature [35, 36, 67]. The signal at $17.70 \mu\text{s}$ was from the adventitia-water interface. The identification of the multiple layers in Fig. 5.3 was consistent with the layers which we observed visually in Fig. 5.2. For most of the regions which we inspected the reflection from the intima-media boundary was strong, as was the media-adventitia boundary. However, the reflection from the adventitia-water interface was relatively weak, which we attributed to a combination of similar impedances and the attenuation of the signal. We suspect that the curved surface on the back of the tissue also affected the signal.

Not all of the data was as clean as the reflections shown in Fig. 5.3. Figure 5.4 shows a ‘poor’ waveform where interfacial echoes were hard to discern. Therefore, the automated peak-detect routine that was used to identify surface reflections in the polyethylene and phantom measurements could not be employed for locations that had these indistinguishable echoes. Instead the data for each location had to be inspected visually to ensure that clear interface signals were present that could be identified by the automated analysis. Waveforms without clear interface signals were excluded from the analyses. The automated peak-detect routine, with an additional peak threshold detection routine, was employed for the *1f* and *2a* data sets. For all of the measurements, the location of the reflection from each layer boundary in the signal was further checked manually to ensure that the location was being identified correctly.

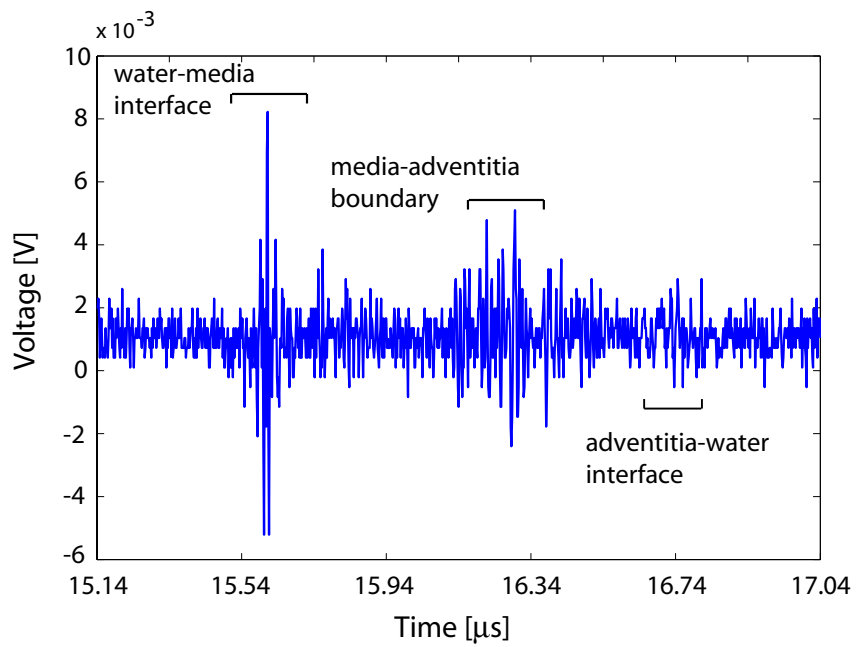


Figure 5.4: A 'poor' signal from the artery. The echoes from the intima-media, media-adventitia and adventitia-water boundaries are clearly visible, delineating each layer. The medial layer features more backscatter than the other layers.

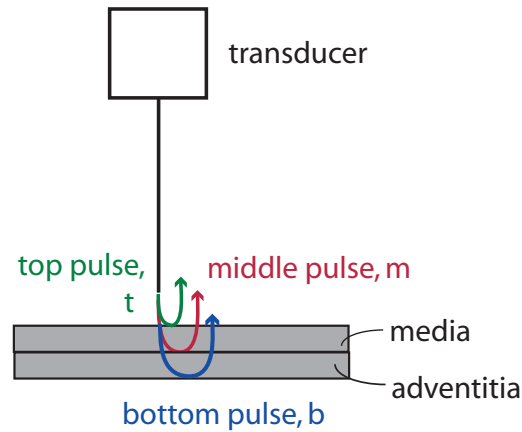


Figure 5.5: Reflections from a pulse through an artery. A healthy intima is nearly acoustically transparent, so the wave is reflected from the water-media, media-adventitia, and adventitia-water interfaces.

5.2 Two-layer analysis

The most important difference between tissue and the phantoms is the presence of multiple layers in the tissue. This means that the plane wave theory analysis developed in Chapter 2 for uniform media is not valid. It is necessary therefore to develop a new analysis for a layered medium.

For a two-layered medium we expect three reflected pulses to be observable, as illustrated in Fig. 5.5. Figure 5.3 showed that a healthy intima does not reflect the pulse very strongly, so we consider a healthy artery to effectively have two layers: the media and the adventitia. We will refer to these pulses as P_t , P_m , and P_b .

Using the same plane wave approximation as in Chapter 2 we can predict what the

spectra of these three pulses should be. For the reflection from the top surface

$$P_t(f) = P_0(f)R_{wm}E(f) \quad (5.1)$$

where R_{wm} is the reflection coefficient from the water-media boundary and P_0 and $E(f)$ account for the transmission effects through the water column between the transducer and sample surface. The middle pulse will be given by

$$P_m(f) = P_0(f)T_{wm}R_{ma}e^{-2\alpha_m(f)x_m}T_{mw}E(f) \quad (5.2)$$

where T_{wm} is the pressure transmission coefficient for the water-media boundary, the exponential term accounts for the roundtrip attenuation in the media, R_{ma} is the reflection coefficient for the media-adventitia boundary, and T_{mw} is the transmission coefficient at the media-water boundary.

The reflection from the bottom of the tissue, the adventitia-water interface, transmitted through the media-adventitia boundary with an amplitude T_{ma} . The pulse traveled through the adventitia layer and reflected off the adventitia-water interface with a reflection coefficient R_{aw} . The pulse transmitted through the adventitia-media boundary and through the media-water boundary and once transformed to the frequency domain, was $P_b(f)$.

$$P_b = P_0(f)T_{wm}e^{-2\alpha_m(f)x_m}T_{ma}e^{-2\alpha_a(f)x_a}R_{aw}T_{am}T_{mw}E(f) \quad (5.3)$$

The reflection coefficient at the top interface and the impedance of the first layer are determined in the same manner as before. Therefore R_{wm} and Z_m are

$$R_{wm} = R_{0r} \left| \frac{P_t}{P_r} \right| \quad (5.4)$$

$$R_{wm} = \frac{Z_m - Z_w}{Z_w + Z_m} \quad (5.5)$$

$$Z_m = Z_w \frac{1 + R_{wm}}{1 - R_{wm}} \quad (5.6)$$

The literature reports [35, 57] that the power law exponent y for the attenuation in tissue is close to unity, where the dispersion is at a maximum. As a first order approximation we can assume the impedances for the adventitial layer to be constant with frequency, and for R_{ma} to be constant with frequency as well. These unknown parameters can be isolated by separating Eq. 5.2 in terms of known parameters:

$$\frac{P_m(f)}{P_0(f)E(f)T_{wm}T_{mw}} = R_{ma}e^{-2\alpha_m(f)x_m} \quad (5.7)$$

$$\ln \left(\frac{P_b(f)}{P_0(f)E(f)T_{wm}T_{mw}} \right) = \ln R_{ma} - 2\alpha_m(f)x_m \quad (5.8)$$

The assumptions that the impedance is constant with frequency, R_{ma} , and that attenuation in tissue corresponds to a power law allow us to model the unknown parameters in Eq. 5.8 as

$$\ln R_{ma} - 2\alpha_m(f)x_m = C_1 - C_2f^y \quad (5.9)$$

By fitting Eq. 5.9 to a power law Z_a and $\alpha_m(f)$ can be determined and the transmission and reflection coefficients T_{ma} , T_{am} and R_{aw} in Eq. 5.3 can be solved for. The attenuation in the adventitial layer can be found by separating out the rest of the known parameters:

$$\alpha_a(f) = \frac{1}{2x_a} \ln \frac{P_0(f)E(f)T_{wm}T_{mw}R_{ma}}{|P_b|} \quad (5.10)$$

$$\frac{P_t}{P_w} = \frac{R_{ws}}{R_{wg}} \quad (5.11)$$

$$\left| \frac{P_b}{P_t} \right| = \frac{T_{ws}R_{sr}T_{sw}}{R_{ws}} e^{-2\alpha_s(f)L} \quad (5.12)$$

The backscatter for the medial layer is determined from the form used for the phantoms, as described in Eq. 2.37. For the backscatter in the adventitia, however, the attenuation and transmission loss effects from the medial layer must be accounted for. The attenuation loss in the formulation of the backscatter coefficient of the adventitia is

$$A_{s,adventitia} \cong A_{s,media} \cdot \exp[-4\alpha(\omega)(\bar{r}_a - r_{ma})] \cdot \frac{\exp[2\alpha\tau_p c_s] - \exp[-2\alpha\tau_p c_s]}{4\alpha\tau_p c_s} \cdot \frac{\exp[2\alpha l] - \exp[-2\alpha l]}{4\alpha l} \quad (5.13)$$

where $A_{s,media}$ is the attenuation compensation term for the media determined from Eq. 2.35 and r_a is the distance from the transducer to the middle of the adventitia layer and r_{ma} is the distance from the transducer to the media-adventitia boundary.

We include the transmission loss by examining $\xi(f)$ through the media and adventitia:

$$\xi_{adventitia}(f) = (T_{0m}T_{ma}T_{m0})^2 \quad (5.14)$$

The loss terms $A_{s,adventitia}$ and $\xi_{adventitia}$ are included in the expression for $\eta(f)$ as before, in Eq. 2.37.

5.2.1 Results

The phase velocity of the four measurements at 25 MHz is displayed in Fig. 5.6. The phase velocity showed a large spread, varying from 1278 to 1758 m/s for the four measurements. At 25 MHz, the phase velocity was 1758, 1386, 1257 and 1650 m/s for *1b*, *1d*, *1f* and *2a*, respectively. It should be noted that, similar to the attenuation results, the *1b* and *2a* regions had similar results. The measurements displayed a slight increase with frequency

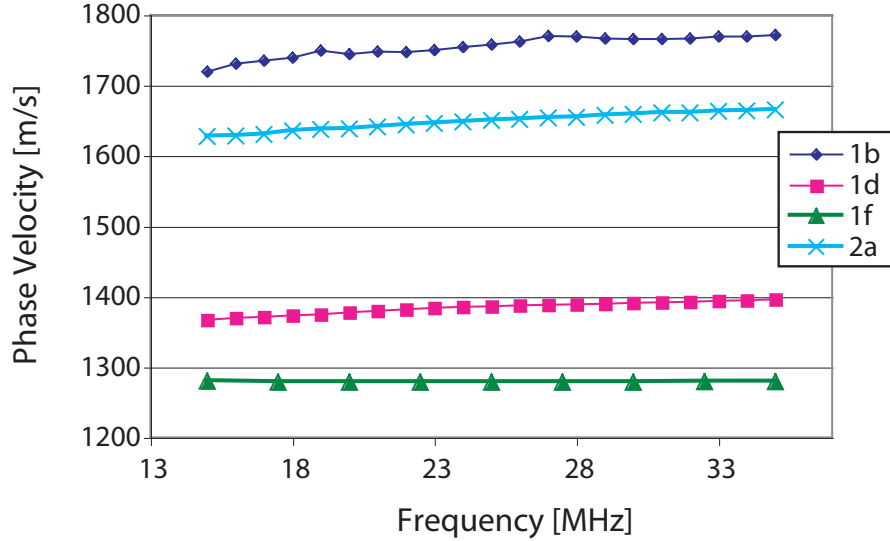


Figure 5.6: Phase velocity of the femoral artery at 25 MHz. The phase velocity was in the expected range for tissue.

with the exception of the $1f$ region. For clarity, the standard deviations were not plotted, due to their relatively high value; for the $1b$, $1d$, $1f$ and $2a$ the standard deviation was 279, 183, 67 and 282 m/s, respectively.

The large spread for each location can be explained in part by the variation in thickness across the sample, which was not taken into account in the analysis. By inspecting the maximum difference in the relative arrival times to the top and bottom layers and multiplying by the mean sound speed we were able to obtain an idea of the range in thickness for each location. For the four locations, the thickness varied 23-35% from the average measured thickness (1.72 mm), which had a maximum 35% variation as well.

The impedance results for the medial layer are shown in Fig. 5.7. The impedance for the four measurements was similar and displayed a small increase over the frequency range.

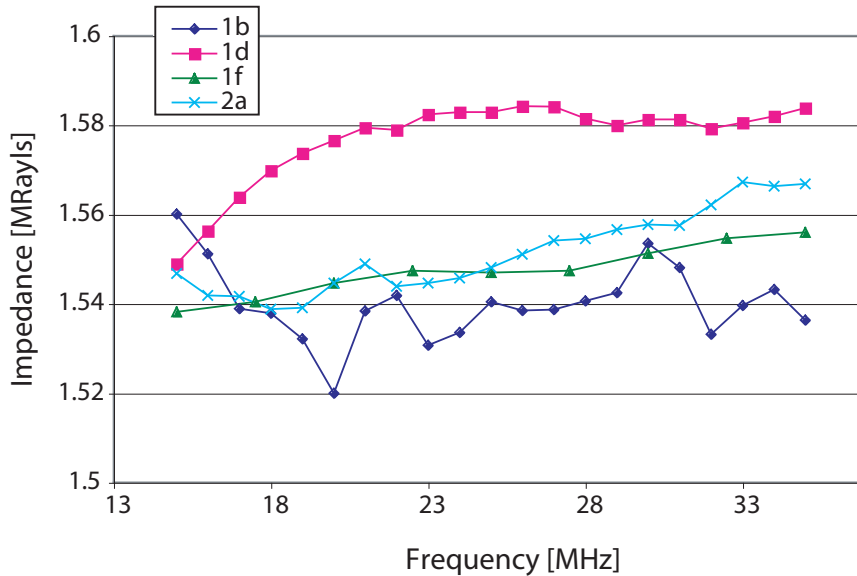


Figure 5.7: Impedance results for the medial layer. The impedance is in the expected range for tissue and was similar for the four regions.

At 25 MHz, the impedance at the *1d* location was 1.58 MRayls, *1b* was 1.54 MRayls and *1f* and *2a* were 1.55 MRayls. The impedance at the *1b* location had the lowest standard deviation at 25 MHz, at 0.02 MRayls, while *1d* had the highest standard deviation of 0.05 MRayls at 25 MHz. The *1f* and *2a* locations had similar standard deviations of 0.03 MRayls at 25 MHz.

The impedance results for the adventitia are displayed in Fig. 5.8. The adventitia generally showed a higher impedance than the media. The results from the *1d* measurements were neglected due to a large spread, but both the *1b* and *2a* locations had a higher impedance than their respective medial layers, 1.66 and 1.64 MRayls, respectively. The impedance for the adventitia in the *1f* data set was slightly lower than its medial layer, 2.04 MRayls. Similar to its medial layer impedance, the *1d* data set was higher than the three

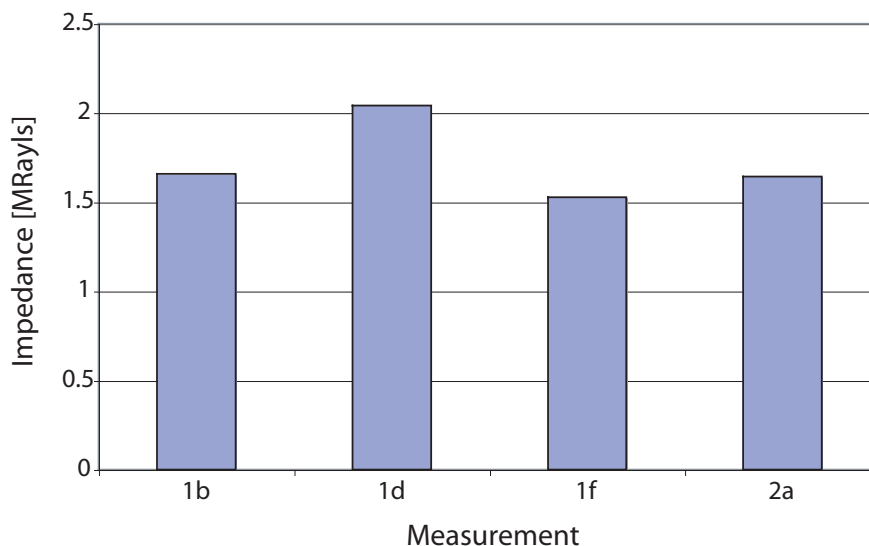


Figure 5.8: Impedance results for the adventitial layer at 25 MHz. The impedance is in the expected range for tissue.

other data sets. The standard deviations were higher in the adventitia by approximately an order of magnitude. We expected a higher standard deviation since the scattered signal at the media-adventitia boundary was not as clearly-defined as for the intima-media boundary.

The attenuation in the media is shown in Fig. 5.9. The attenuation varied for the four measurements. The *1f* region displayed the lowest attenuation of 6 dB/cm at 25 MHz, while the *1d* region had the highest attenuation, 63.7 dB/cm at 25 MHz. The *1b* and *2a* regions were more similar, with attenuations of 24.4 and 19.6 dB/cm at 25 MHz. While the results exhibited a large spread, the power law exponents were largely similar, $y = 1.1, 0.9, 1.1$ for the *1b*, *1d* and *2a* regions, respectively. The power law exponent for the *1f* region was 0.76. The standard deviations are not included since the attenuation results come from a power law fit. The results for y met our expectations, as the literature reports values close to 1 for tissue.

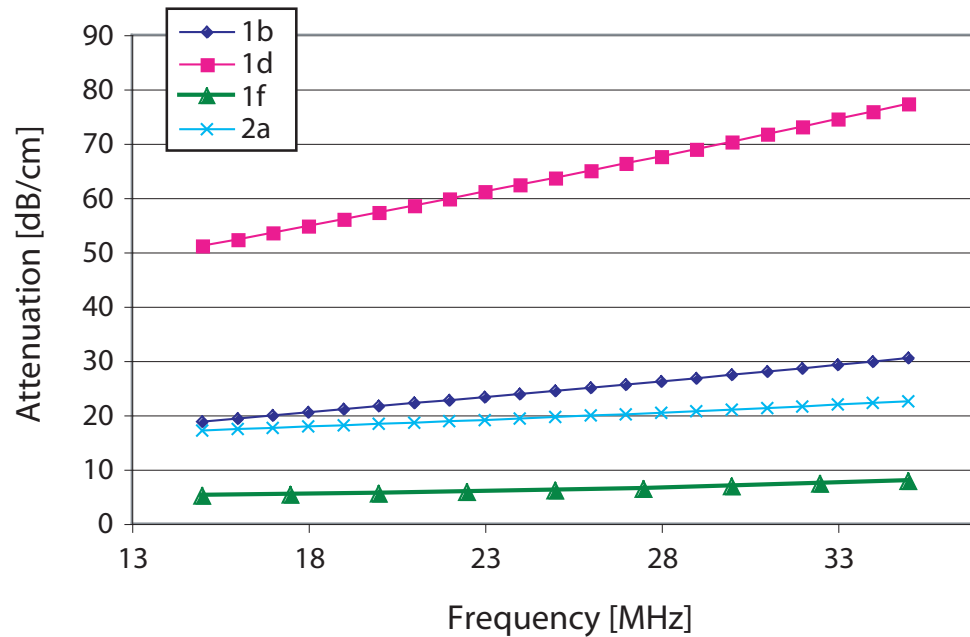


Figure 5.9: Fitted attenuation of the medial layer.

Figure 5.10 shows the measured acoustic attenuation in the adventitia. The attenuation was higher in the adventitial layer. The *1b* and *2a* regions were similar: at 25 MHz the attenuation was 36.1 and 41.4 dB/cm, respectively. The adventitia attenuations in the *1d* and *1f* data sets were considerably higher, with attenuations of 108.6 and 149.4 dB/cm at 25 MHz. The power law exponents ranged from 1.37 to 1.49 for the four regions.

Comparing the attenuation in the individual layers to results from the literature was difficult, since we could not locate any published reports of measurements in the individual layers. The literature reports [5, 14, 22, 35] values for the entire tissue of y close to 1, which falls in the range measured in the SAM. Using $y = 1$ we extrapolated the attenuation values in Table 1.2 to 25 MHz, yielding attenuations for the femoral and carotid arteries ranging

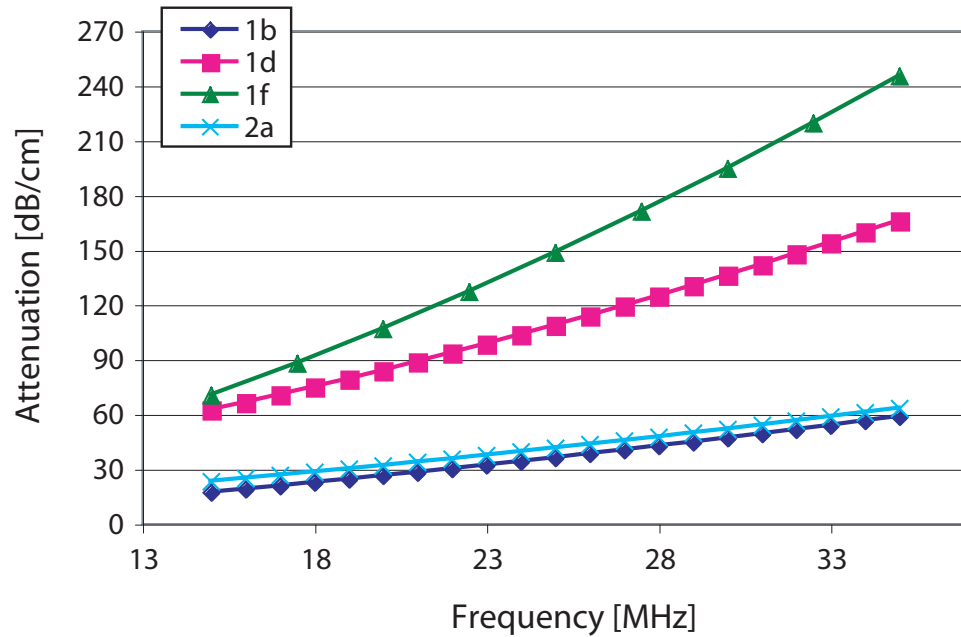


Figure 5.10: Fitted attenuation of the adventitial layer. The attenuation in the adventitia was higher than the media.

from 33-51 dB/cm. Comparing the results to those from the SAM, it would appear that the *1b* and *2a* regions most closely matched the literature results.

Of the four measurements, only *1f* and *2a* produced coherent, reasonable results for the backscatter coefficient. The backscatter coefficient in the media for the two locations is shown in Fig. 5.11. The two regions have similar values and both increase with frequency. The backscatter coefficients at 25 MHz were 1.4 and 2.3 (m Sr)⁻¹ for *1f* and *2a*, respectively. Referring to Table 1.1, Lockwood shows the medial layer of the femoral artery as having a backscatter coefficient of 20 (m Sr)⁻¹ at 50 MHz. Fitting the referenced BC to the reported $f^{1.4}$ trend and extrapolating down to 25 MHz, the referenced BC is 7.6 (m Sr)⁻¹, which is higher than the SAM values.

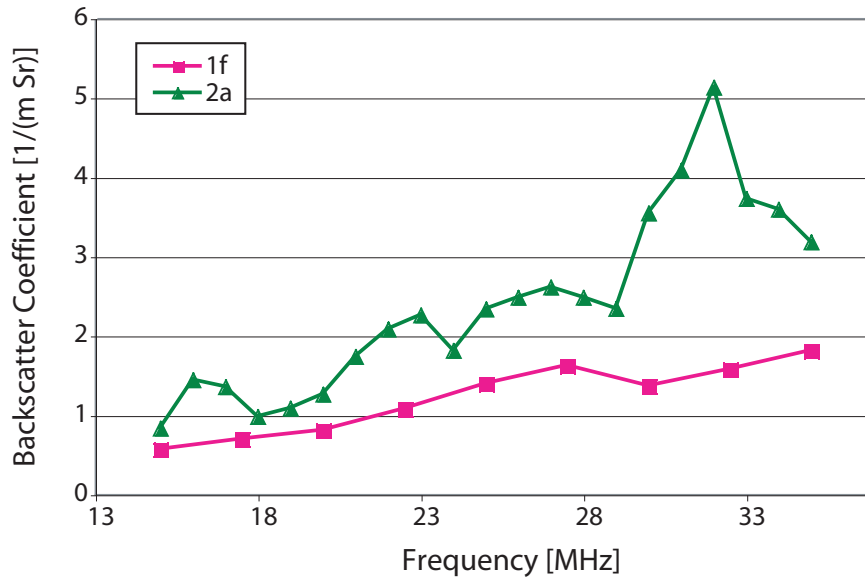


Figure 5.11: Backscatter coefficient of the medial layer in the femoral artery. Compared to the literature $(7.6 \text{ (m Sr)}^{-1})$ the values are low.

The slope for the $2a$ data set is not smooth and reflects the jumps in the frequency spectra from the backscatter signal, shown normalized against the spectra of the reference reflection in Fig. 5.12. The jumps in the slope in Fig. 5.12 are indicators that the noise affects the backscatter signal.

Despite an apparently high level of backscatter for the four data sets visually, only the $2a$ data set had a backscatter coefficient for the adventitial layer in the expected range and trend, shown in Fig. 5.13. The $1d$ measurement of the backscatter coefficient was in the same range as $1f$ but did not increase with frequency. The $1f$ measurement increased with $f^{3.5}$ but was an order of magnitude higher than the $2a$ measurement. As expected, the BC for the adventitia was higher than the medial layer and features similar jumps in the slope. The BC increased from 2.4 to 27.7 (m Sr)^{-1} over the 15-35 MHz range and corresponded

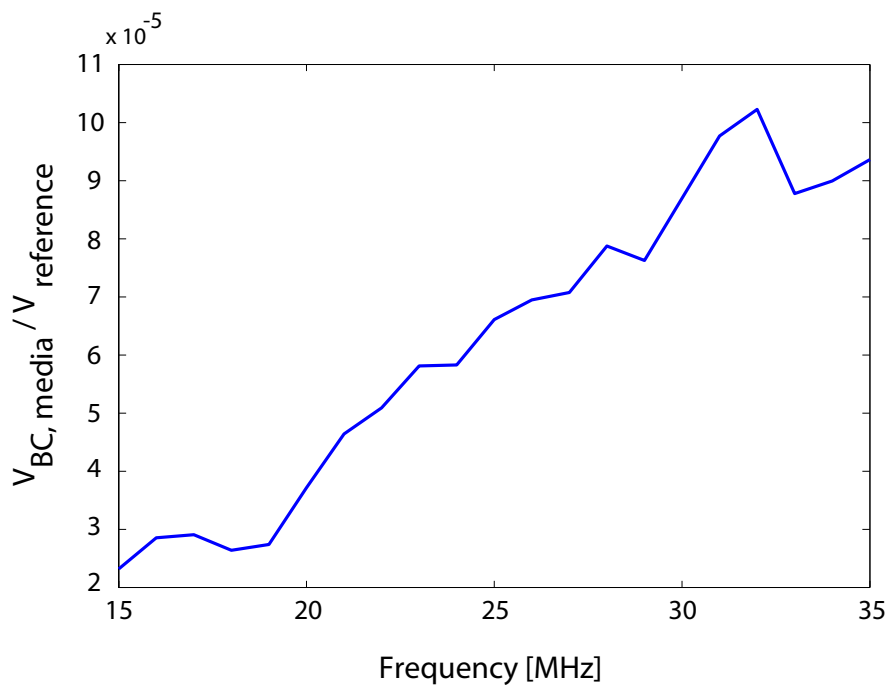


Figure 5.12: Frequency spectra of the backscatter region in the medial layer, normalized against the spectra of the reference reflection for a representative data point in sample *2a*. The slope is not smooth, since the noise contributes to backscatter signal, and ultimately affects the slope of the backscatter coefficient.

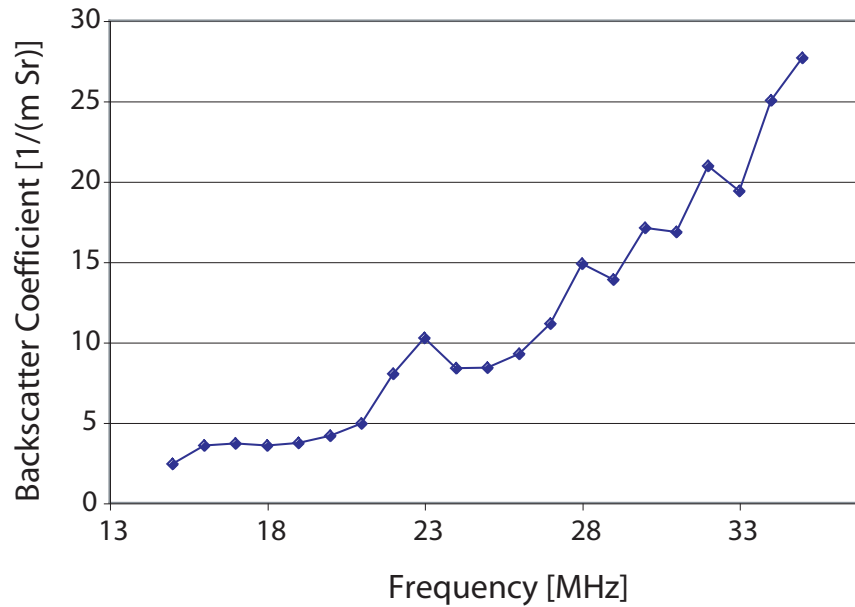


Figure 5.13: Backscatter coefficient of the adventitia layer for the *2a* region. The result is low compared to the literature value (30 (m Sr)^{-1} at 25 MHz).

to an $f^{2.8}$ slope when fit to a power law. The Lockwood [35] study reported a backscatter coefficient of 80 (m Sr)^{-1} at 50 MHz. Extrapolating in the same manner as for the medial value, the referenced backscatter coefficient is 30 (m Sr)^{-1} at 25 MHz, which compares favorably with the backscatter coefficient for the SAM adventitia which was 8.4 (m Sr)^{-1} at 25 MHz.

As an initial feasibility study, the arteries provided a good chance to apply the measurement scheme and analysis techniques of the SAM to tissue. Measurements of impedance, sound speed, attenuation and backscatter coefficient were all consistent with values reported in the literature.

Chapter 6

Discussion/Conclusion

A scanning acoustic microscope has been successfully implemented. For the case of homogeneous materials, plane wave analysis was presented that allowed us to determine the acoustic impedance, attenuation, phase velocity and backscatter coefficient of homogeneous materials. The system was validated by measuring the attenuation and phase velocity of high- and low-density polyethylene and comparing the SAM measurements with literature results. Causality was used to further validate the attenuation and phase velocity relationships. The focal region of the transducer was examined to validate the plane-wave approximation of the analysis and a range of the insonification angle from the transducer for which the measurements remained valid was determined. A set of recipes for tissue-mimicking phantoms were developed and characterized for use in the SAM and an IVUS system. An initial study was performed on a human femoral artery.

6.1 Validation of impedance, attenuation and phase velocity measurements

Two types of HDPE of varying thickness, KP and LP, were measured for impedance, attenuation and phase velocity over a 10-35 MHz range. The results at 10 and 35 MHz are compiled in Tables 6.1 and 6.2. The acoustic impedance Z exhibited a slight increase with frequency which is consistent with the increase in phase speed. The density for the two samples was determined from the impedance and sound speed and was within 7% of the manufacturer's value for the density. The attenuation α increased with frequency and displayed the expected power law slope. Using Szabo's time causal model (TCM) for a medium with power law attenuation the measured attenuation was used to predict the dispersion of the phase velocity. The dispersion predicted by the time causal model was similar to the measured dispersion above 17.5 MHz. Below 17.5 MHz the time causal model predicted a steeper slope in dispersion and this may be attributable to the low signal to noise ratio in the measurements at those frequencies.

Table 6.1: Measured and extrapolated results for HDPE at 10 and 35 MHz

Sample	$\alpha \pm \alpha$ [dB/cm]	$Z \pm Z$ [MRayls]	$c \pm c$ [m/s]	TCM [m/s]
SAM KP	21.8-110.6 \pm 2-6	2.33-2.42 \pm 0.1	2421-2436 \pm 3	2417-2436
SAM LP	25-119 \pm 5-2	2.25-2.37 \pm 0.09-0.02	2280-2291 \pm 4	2273-2292
Wu	21.6-86.1	–	–	2387-2400
He & Zheng	15.3-68.9	–	–	2580-2596

Table 6.2: Comparison of manufacturer and measured values for HDPE at 25 MHz

Sample	ρ_{man} [g/cm ³]	ρ_{SAM} [g/cm ³]
SAM KP	0.94	1.01
SAM LP	0.96	0.98

The results for the attenuation and phase velocity of the HDPE samples were compared with measured results for HDPE by Wu and He and Zheng. The referenced results were measured at a lower frequency range so the attenuation values were fit to a power law and the attenuation was extrapolated to the frequency range (10-35 MHz) of the SAM. The time causal model was used to extrapolate the phase velocity values to the higher frequencies. The extrapolated results for WHZ at 10 and 35 MHz are also shown in Table 6.3. The agreement with WHZ is satisfactory given the fact that the WHZ results were extrapolated out to five times the reported frequency. The phase velocity measurements all fell with a 200 m/s (<10%) range and variation is likely due to sample differences. The four data sets exhibited similar dispersion, although it should be noted that the slope of the time causal model extrapolation for both referenced results was slightly lower than the results at the lower frequencies.

LDPE was also measured for impedance, attenuation and phase velocity over a 10-35 MHz range. The results are presented at the 10 and 35 MHz frequencies in Table 6.3. The trends exhibited by the LDPE were similar to those of the HDPE. The impedance increased with frequency and was similar to the manufacturer's value for the density. The attenuation exhibited the expected power law and the time causal model agreed with the measured phase

velocity above 17.5 MHz. Similar to the HDPE samples, the TCM predicted a steeper slope below 17.5 MHz.

Table 6.3: Measured and extrapolated results for LDPE at 10 and 35 MHz

Sample	$\alpha \pm \alpha$ [dB/cm]	$Z \pm Z$ [MRayls]	$c \pm c$ [m/s]	TCM [m/s]
SAM	52.1-222.3 \pm 7-14	2.0-2.1 \pm 0.06-0.01	2032-2059 \pm 5	2027-2059
Wu	51.4-177.3	–	–	2040-2066
He & Zheng	48.1-133.8	–	–	2576-2593

Wu and He and Zheng published results for LDPE at lower frequency ranges as well, so the same methods used for the HDPE were used to extrapolate the results to the 10-35 MHz range, also presented in Table 6.3. The data sets all exhibited similar attenuation through 10 MHz; however at 35 MHz the SAM attenuation was significantly higher. This is likely due to the fact that extrapolating a power law attenuation leads to large discrepancies at the higher frequencies. The phase velocity extrapolations for WHZ also had a large variance, of 500 m/s, also attributable to the difference in the LDPE samples. The SAM results were similar in value to the Wu extrapolations and the overall slopes for the three studies were similar.

All three groups showed some disagreement in the attenuation and phase velocity values but since the differences were relatively small and the overall trends were similar we consider that the SAM is able to produce valid measurements of attenuation and phase velocity for homogeneous materials. We attribute the differences in the results to the materials, as we were unable to obtain the exact types of polyethylenes which the He and Zheng and Wu groups measured.

6.2 Pulser energy settings

We noticed some discrepancies in the impedance results when we used different energy settings for the transducer. Since the impedance depends on the amplitude of the reflected pulses from the glass and top surface of the material, we examined the frequency spectra of the pulse for the glass and the HDPE. The frequency spectra varied by the energy setting, as the spectra peaked at lower frequencies for the higher energy levels. We attributed the differences to the fact that at higher energies the pulser excited the transducer with a longer duration electrical signal which should increase the amplitude at the lower frequency levels. However, more puzzling was that the response was slightly different in the reference and HDPE measurements, as the reference exhibited sharper peaks than the HDPE. This discrepancy shows up most clearly in the impedance results since the impedance calculation depends mostly on the ratio of the signal amplitudes from the top surface and reference measurements. The attenuation calculation does not have as strong a dependence on the reference measurement and the calculation of the sound speed does not involve the reference measurement at all. The attenuation and phase velocity did not show a large dependence on the energy level, so we decided to use the highest energy level in order to improve the signal to noise ratio. For the impedance measurements we decided to use the energy level which gave us the best response from the transducer; as the frequency response for the reference at the lowest energy level had the most rounded and even distribution over the frequency range we decided to measure the impedance at the lowest energy level. The lack of agreement in impedance measurements at given energy levels warrants further investigation.

6.3 Focal region

The focal region of the transducer was examined in order to validate the plane wave assumption and to find the optimal position for the sample. By inspecting the attenuation, phase velocity and impedance at half-millimeter steps from 9-15 mm from the transducer we determined that the three properties stayed locally constant for a distance of 11.5-13 mm from the transducer to the top of the sample surface. The attenuation increased by 12 dB/cm from 11.5-13 mm at 25 MHz but when the attenuation was normalized to the attenuation at the nominal focal length there was an increase of less than 15% from 11.5-13 mm. The phase velocity and impedance showed a smaller variation over the 11.5-13 mm range at 25 MHz: the phase velocity decreased by 5 m/s and the impedance decreased by 0.01 MRayls. We concluded that the sample should be placed 11.5 mm from the transducer.

6.4 Effect of transducer angle

The angle of the transducer was varied to determine the range for which the plane wave theory remained valid. The sample table was tilted from 0 to 5° by 0.5° increments and the impedance, attenuation and phase velocity were measured. We concluded that the angle of the transducer could vary up to $\pm 2.5^\circ$ before the results deviated from the normal incidence result by more than 6%. The impedance and phase velocity decreased with an increase in angle but, up to 2.5°, showed a deviation of 0.04 MRayls and 5 m/s, respectively. The attenuation increased with the angle and deviated by 4 dB/cm with a 2.5° tilt in the

Table 6.4: Effect of silica concentration at 25 MHz

Silica [%]	$\alpha \pm \delta\alpha$ [dB/cm]	$Z \pm \delta Z$ [MRayls]	$\eta \pm \delta\eta$ [(m Sr) ⁻¹]
2	18.9 ± 1	1.60 ± 0.06	1.21 ± 0.07
6	30.9 ± 2	1.63 ± 0.1	9.94 ± 0.9
10	45.3 ± 4	1.68 ± 0.1	25.3 ± 5

transducer.

6.5 Phantom measurements

We developed a set of recipes for tissue-mimicking phantoms which allowed us to vary the impedance, attenuation, phase velocity and backscatter coefficient. Using Burlew, Madsen, Ryan and de Korte’s recipes as guidelines we developed a base recipe and varied the ingredient concentrations. We found that altering the silica content primarily affected the attenuation and backscatter coefficient and had a minimal effect on the impedance. The propanol and gelatin affected the properties in varying proportions. Agar concentration appeared to have no effect on the acoustic properties. We noticed very little dispersion in the phase velocity results and the time causal model matched this level of dispersion for all of the results.

Increasing the concentration of silica increased both the attenuation and backscatter coefficient and a slight increase in impedance was observed. The effect of the silica concentration on the measured impedance, attenuation, and backscatter coefficient at 25 MHz is shown in Table 6.4. The sound speed was unaffected by the silica content.

Previous studies have reported an increase in sound speed with an increase in propanol. We tested the effect of the propanol content by varying the concentration at percentages of 0, 8 and 12% and indeed noticed an increase in sound speed. The other properties remained unaffected by the propanol concentration. Table 6.5 compiles the results. The literature [35] reports a range from 1579-1628 m/s for the human artery so the 12% propanol phantoms are in the vicinity of the human artery.

An increase in the gelatin concentration was found to increase the sound speed in the phantoms and affected the attenuation as well. We increased the gelatin content from 10-25% in 5% increments and the results are compiled in Table 6.6. For the 20% batch a different technique for adding the silica to the solution so this data is excluded from the table (see Sec. 4.4.4 for the full results). The increase in phase velocity with gelatin concentration was not uniform. There was a marked increase in the attenuation with gelatin but the backscatter coefficient didn't change. Therefore gelatin provides a process by which the attenuation can be changed independent of the backscatter coefficient. This effect is presumably because the gelatin affects the absorption of sound rather than the scattering.

With the proper concentrations the phantoms have been shown to provide the documented sound speed, attenuation and backscatter for human tissue.

Table 6.5: Effect of propanol concentration at 25 MHz

Propanol [%]	$c \pm \delta c$ [m/s]
0	1352 ± 7
8	1391 ± 25
12	1547 ± 16

Table 6.6: Effect of gelatin concentration at 25 MHz

Gelatin [%]	$\alpha \pm \delta\alpha$ [dB/cm]	$c \pm \delta c$ [m/s]
10	25.6 ± 2	1343 ± 18
15	29.1 ± 2	1391 ± 24
25	36.0 ± 3	1444 ± 20

6.6 Variations in phantom results

In the course of the phantom experiments we noticed variation in the results both from batch to batch and within given batches. We expected that due to the nature of the phantom construction process, the properties of the phantoms would change between batches but the variations (i.e., the precision) within the batches were unexpected. We noticed up to 6% variation in the results (for the sound speed, slightly lower for the other properties) within the three phantoms from a given batch. This variation must be attributed to problems inherent to the phantoms, since variation between samples in the polyethylene experiments was highest for the impedance, at 1.5%. We were also surprised that the attenuation and backscatter coefficient did not exhibit a more directly proportional relationship within each phantom since the two properties are closely related to the scattering distribution and content; there were multiple measurements where the respective change in attenuation within a batch was not reflected in the same manner in the backscatter measurements.

Two factors which could lead to these differences are the order in which the phantoms were poured into the molds and measured and the sample thickness. The phantom solution was always poured into the molds and measured in the same order (a , b , c) but there was

no apparent relationship between the results and the particular mold. The difference in thickness showed a positive correlation with the backscatter results in the silica variation experiments. This correlation is puzzling, since the thickness of the phantom does not enter into the calculation of the backscatter coefficient since the BC is a measurement of the backscatter cross-section of the scatterer per unit volume. However, the relationship could have some implications that there is settling of the silica particles after the phantom was poured, although we would expect to see an impact of the thickness on the attenuation results as well. Swelling of the phantom, which would increase the water content in the top of the phantom, could also play a role, since the effective particle density would change as a function of depth within the phantom. We suggest that future experiments examine both these relationships closer.

Previous studies of phantoms have reported large discrepancies as well. Notable is the Madsen et al [43] study, where 10 different groups characterized ten sets of phantoms from the same batch for the sound speed, attenuation and backscatter coefficient. Each set consisted of two phantoms which differed in the concentration of water, n-propanol, agar, graphite and glass beads. Multiple methods of measurement and analysis were used in the study. There was good agreement in the results for the attenuation but the propagation speed and backscatter coefficient results varied widely. The results for the sound speed varied by about 20 m/s for the two phantoms and the backscatter coefficient results varied by more than an order of magnitude. In light of this study, the differences observed in the SAM phantoms are better received.

6.7 Tissue study

One of the goals for the SAM is to characterize arterial plaque. As a step towards that goal we measured the acoustical properties of three human artery walls in order to gain experience and examine the limitations of the SAM when working with *in vitro* artery samples. The arteries were not easy to work with, as they sagged over the time it took to complete a scan and the reflections from the top and bottom surfaces were not always very strong. We experimented with two windowing settings for capturing the top and bottom surface reflections and determined that capturing the two reflections in the same window made the data easier to interpret and analyze.

Only the data obtained with the femoral artery was analyzed and not all of the locations in the raster scan returned good data. Since the tissue was effectively a two-layer medium we developed an analysis based on the assumption that the sound speed was constant through both layers. As a result, the attenuation, impedance and backscatter coefficient was determined for the medial and adventitial layers and the phase velocity was determined for the tissue. The results for the four measurements at 25 MHz are compiled in Table 6.7. We had to examine each location to inspect the signals before the data could be analyzed.

The impedance values matched the expected values, and the adventitia generally had a higher impedance than the media. In addition, the impedance exhibited a slight increase with frequency, which suggests that there is small amount of dispersion in the tissue. The attenuation exhibited a large spread in both the media and adventitia measurements. The *1b* and *2a* results were similar to the average attenuation results found in the literature.

Table 6.7: Tissue results at 25 MHz

Measurement	α [dB/cm]	Z [MRayls]	c [m/s]	η [(m Sr) ⁻¹]
media:				
1b	24.4	1.54	1758	–
1d	36.7	1.58	1386	–
1f	6.0	1.55	1278	1.40
2a	19.6	1.55	1650	2.33
adventitia:				
1b	36.1	1.66	1758	–
1d	108.6	2.04	1386	–
1f	148.4	1.53	1278	–
2a	41.4	1.64	1650	8.4

The power law exponent for the medial layer was close to the reported literature values of $y = 1$ but was higher in the adventitial layer. The sound speed also had a large variation between measurements but again, the *1b* and *2a* regions were similar to the published results for tissue. The backscatter coefficient was in the documented range for the two layers, but is based only the *1f* and *2a* regions for the media and the *2a* region for the adventitia. However, both the attenuation and backscatter measurements were affected by the noise in the signal, as the reflection from the bottom surface was quite weak and the noise contribution to the backscatter signal was clearly visible.

The arteries provided valuable experience for adapting the SAM to *in vitro* artery measurements. The main deficiency in the measurements was the reflection from the bottom surface, and future work should focus on improving the signal from the bottom surface. A better holder should be constructed to fix the tissue so the surface is more planar, while

preserving the water backing. A flatter surface should improve the reflection from the top surface and should have the same impact for the reflection from the bottom surface. The thickness measurements can be improved as well. We suggest trying to replicate the method used to measure the thickness of the phantoms. For example, by punching a hole into a section of the tissue which is over the sample holder we could measure the time of travel to the bottom of the sample through the water channel in the hole. If the top surface of the artery was kept flat enough over the region where it is being measured with the water backing, then it could be assumed that the bottom of the artery is at the same height as the region where the hole was punched. Hence, the thickness of the sample could be determined at every location by applying the thickness measurement method used for the phantoms.

6.8 Summary and Conclusions

Methods and instrumentation for the acquisition and analysis of acoustical data leading to the determination of the acoustical impedance, attenuation, phase velocity and backscatter coefficient were developed for a scanning acoustic microscope operating over the 10-40 MHz range. The impedance, attenuation and phase velocity were validated against documented results for high and low-density polyethylene. The attenuation and phase velocity were further validated through the causality condition using the time causal model. A set of recipes was developed for tissue-mimicking phantoms which demonstrated control over the impedance, attenuation, phase velocity and backscatter coefficient of the phantoms. Preliminary experiments demonstrated the utility of the SAM in being able to measure and

recover the acoustic properties of human tissue. The eventual goal is to measure tissue with enough accuracy to identify regions with plaque and successfully correlate the results with histology.

Appendix A

MATLAB Analysis Codes

The MATLAB analysis consists of a ‘front end’ code, which is primarily responsible for passing the name and location of the data file to the ‘back end’ analysis code, as well as the plotting of the results. The first code shown here, *an_G15S6P0_1a.m*, is a sample front end code used for the analysis of a 15% gelatin, 6% silica, 4% agar, 0% propanol phantom constructed in the *a* mold. The analysis back end code, *singleanal_vabc.m*, is responsible for the processing of the data. The analysis calls a short least-squares error routine, *lsealpha.m*, which appears after the analysis code.

The analysis of the polyethylene data is similar to the phantom analysis with the exception of the backscatter coefficient calculation and the thickness calculation, both of which are omitted for the polyethylene sample analyses.

```
% an_G15S6P0_1a.m, front-end template for single-layer analysis  
  
% written: Caleb Farny, 01/26/03  
clc
```

```

cd ..
% specify directory date for sample:
sampledir = '14-May-2003';
datedir(1) = datenum(sampledir);
% for glass, if in separate directories:
glassdir = '12-Apr-2003';
datedir(2) = datenum(glassdir);
% specify title of sample and glass datafiles (w/o format):
sample = 'G15S6P0_1a';
glass = 'ref_seqE18';
bc_title = 'G15S6P0_ptpbc_1a';

global Pw Pt
% specify range for freq:
freqmin = 15e6;
freqmax = 35e6;
% specify material for impedance:
Zr = 13e6; % for glass [Rayls]

% Call analysis function:
[c1,alpha,alphacal,Z1,c_tcm,y,a1,freq,fmin,fmax,th,eta] ...
    = singleanal_vabc(datedir,sample,glass,freqmin,freqmax,Zr,bc_title);

[l m n] = size(c1);

% ----- cleanup and declarations -----
Z1 = Z1 * 10^-6;
% calculate atten in dB/cm:
alphadb = alpha * 8.6859 / 100;
alphacaldb = alphacal * 8.6859 / 100;
% reshape:
rsc = reshape(c1,size(c1,1),numel(c1(1,:,:)));
rstcm = reshape(c_tcm,size(c_tcm,1),numel(c_tcm(1,:,:)));
rsatt = reshape(alphadb,size(alphadb,1),numel(alphadb(1,:,:)));
rscalatt = reshape(alphacaldb,size(alphacaldb,1), ...
    numel(alphacaldb(1,:,:)));
rsz = reshape(Z1,size(Z1,1),numel(Z1(1,:,:)));
rseta = reshape(eta,size(eta,1),numel(c1(1,:,:)));

% determine averages:
for f = fmin:fmax,
    fcount = f - fmin+1;

```

```

        meanc(fcount,1) = mean(rsc(f,:));
        stdc(fcount,1) = std(rsc(f,:));
        meanatt(fcount,1) = mean(rsatt(f,:));
        stdatt(fcount,1) = std(rsatt(f,:));
        meancalatt(fcount,1) = mean(rscalatt(f,:));
        meanpc(fcount) = mean(rstcm(fcount,:));
        stdpc(fcount) = std(rstcm(fcount,:));
        meanz(fcount,1) = mean(rsz(f,:));
        stdz(fcount,1) = std(rsz(f,:)); % [MRayls]
        meaneta(fcount,1) = mean(rseta(f,:));
        stdeta(fcount,1) = std(rseta(f,:));
end
meany = mean(mean(y));
meanal = mean(mean(a1));
rho = meanz./meanc*10^6;

sample
format bank
disp('mean of the sound speed: '); meanc
format
disp('standard deviation of sound speed: '); stdc
disp('mean of power law, y'); meany
disp('mean of the standard deviation for y'); mean(std(y))
disp('mean of alpha_1'); meanal
disp('mean of attenuation at center freq:'); meanatt
disp('standard deviation of attenuation:'); stdatt
disp('mean of impedance:'); meanz
disp('standard deviation of impedance:'); stdz
disp('density:'); rho
sample

% ----- plotting section -----
freq = freq*10^-6;
frange = freq(fmin:fmax);
figure;
subplot(2,1,1);
yr=plot(freq(1:60),rsc(1:60,:),'b');
hold on
gh=plot(frangle,rstcm,'g');
title(['Sound speed for: ',sample]);
legend([yr(1,1) gh(1,1)],'Actual','Time Causal Model Prediction',4);
xlabel('Frequency [MHz]');

```

```

ylabel('Sound speed [m/s]');
subplot(2,1,2)
% plot mean sound speed:
plot(frange,meanc);
hold on
plot(freq(fmin:fmax),meanpc,'md');
legend('Actual','Time Causal Model Prediction',4);
errorbar(freq(fmin:fmax),meanc,stdc);
title('Mean Sound Speed');
xlabel('Frequency [MHz]');
ylabel('Sound Speed [m/s]');
% plot attenuation:
figure;
subplot(2,1,1)
plot(frange,rsatt(fmin:fmax,:),'k')
title(['Attenuation for: ',sample]);
xlabel('Frequency [MHz]');
ylabel('Attenuation [dB/cm]');
subplot(2,1,2)
plot(frange,meanatt)
errorbar(frange,meanatt,stdatt);
title(['Attenuation in dB/cm for: ',sample]);
xlabel('Frequency [MHz]');
ylabel('Attenuation [dB/cm]');
% evaluate fit, plot alpha matrix:
figure;
plot(frange,rscalatt(fmin:fmax,:),'r');
title(['Calculated Attenuation for: ',sample]);
xlabel('Frequency [MHz]');
ylabel('Attenuation [dB/cm]');
% plot impedance:
figure;
subplot(2,1,1)
plot(frange,rsz(fmin:fmax,:),'k');
title(['Impedance for: ',sample]);
xlabel('Frequency [MHz]');
ylabel('Impedance [MRayls]');
hold off
subplot(2,1,2)
plot(frange,meanz)
errorbar(frange,meanz,stdz)
title('Mean Impedance')

```

```

xlabel('Frequency [MHz]')
ylabel('Impedance [MRayls]')
figure;
plot(frange,rho)
title('Sample Density')
xlabel('Frequency [MHz]')
ylabel('Density [kg/m^3]')
if exist('th')==1,
    % surface thickness plot:
    figure;
    imagesc(th);
    colorbar
end
figure;
plot(frange,meaneta)
errorbar(frange,meaneta,stdeta)
title('Backscatter Coefficient')
xlabel('Frequency [MHz]')
ylabel('Backscatter Coefficient [mm^-1 Sr^-1]')
loader = zeros(fmax-fmin+3,12);
loader(1,3) = meany;
loader(1,4) = meana1;
loader(1,5) = mean(mean(th));
for cnt = 3:fmax-fmin+3,
    num = cnt - 2;
    loader(cnt,1) = frange(num,1);
    loader(cnt,2) = meanatt(num,1);
    loader(cnt,3) = stdatt(num,1);
    loader(cnt,4) = meancalatt(num,1);
    loader(cnt,5) = meanc(num,1);
    loader(cnt,6) = stdc(num,1);
    loader(cnt,7) = meanpc(1,num);
    loader(cnt,8) = meaneta(num,1);
    loader(cnt,9) = stdeta(num,1);
    loader(cnt,10) = meanz(num,1);
    loader(cnt,11) = stdz(num,1);
    loader(cnt,12) = rho(num,1);
end
cd prop
save(strcat('prop_',sample,'.mat'), 'freq', 'meanc', ...
    'c1', 'alpha','eta', 'Z1','rho','th', 'meany', 'meana1', 'meanatt', ...
    'meaneta','meanz', 'stdc','stdatt','meaneta','stdz','meanpc','th')

```



```

save(strcat('load_',sample,'.xls'), 'loader','-ASCII','-DOUBLE','-TABS')

cd ../

% ----- end of front end code -----

% ----- start back end code -----
% singleanal_vabc.m: acoustic analysis for single-layer medium
% written: Caleb Farny, 4/12/03
% -----
function[c1,alpha,alphacal,Z1,c_tcm,y,a1,freq,idxmin,idxmax,th,eta] ...
    = singleanal_vabc(datedir,samp_title,gl_title,freqmin,freqmax, ...
Zr,bc_title)

% convert directory names:
sampledir = datestr(datedir(1));
glassdir = datestr(datedir(2));
cd data
cd(glassdir)
load(gl_title)
cd ../
cd(sampledir)
load(samp_title)
load(bc_title)
ref = desc.ref; % 0 for water, 1 for glass
if nargin==8,
    th = desc.th*10^-3;
end
cd ../..

global Pw Pt
% specify range for freq:
freqmin = 15e6;
freqmax = 40e6;
% specify material for impedance:
Zr = 13e6; % for glass [Rayls]

% convert directory names:
sampledir = datestr(datedir(1));
glassdir = datestr(datedir(2));
cd data
cd(glassdir)

```

```

load(gl_title)
cd ../
cd(sampdir)
load(samp_title)
load(bc_title)
ref = desc.ref; % 0 for water, 1 for glass
% if nargin==8,
    act_th = desc.th*10^-3
% end
cd ../..

global Pw Pt

if exist('vwf1')==0,
    vwf1 = vwf;
    vwfa = vwf;
    vwfi = vwf;
end

pwa = vwfa;
pwi = vwfi;
pta = vwfa;
pti = vwfi;
pb = vwf2;
pbc = vwfb1;

% define local constants:
Z0 = 1.5e6; % for water [Rayls]
c0 = 1491; % water, [m/s]
rho_0 = 1e3; % water, [kg/m^3]
D = 11.5e-3; % focal length [m]
E_inf = 0.46; % constant
apt = 0.125*2.54/(2*100); % aperature radius [m]
% pull out size from pulses:
[l m n] = size(pb); % should be representative of each pulse
% thickness info:
if exist('vwf3')==1,
    [amp3 ind3] = max(vwf3);
    tm_r = t03 + ind3*tsample;
end
tm_t = t01;

```

```

th = zeros(m,n);
% initialize:
uwcnt1 = 0;
uwcnt2 = 0;
winidx = [-99:100];    % window measure
winidxs = [1:200];    % window measure for BC
tau = length(winidxs)*tsample;    % length of time gate of BC region [s]
tau_p = 4.1673e-08;    % length of pulse [s]
% define freq range:
npts = length(winidx);
hlen = npts/2;    % new
deltaf = 1/(tsample * npts);
wind = hann(npts);
freq = (deltaf * [1:hlen-1])';    % take positive freq's
omega = 2*pi*freq;
% determine location of limits within freq:
[amp idxmin] = min(abs(freq - freqmin));
[amp idxmax] = min(abs(freq - freqmax));
fc = round(median(idxmin:idxmax));    % center freq
omegacen = omega(fc);

k0 = omega/c0;
szfreq = size(freq);
wdx = size(winidx);
% calculate variables:
Gp = k0 * apt^2 / (2*D);
D_ref = exp( (2/pi)*(Gp/pi).^(-1/2) );

% choose between glass/reference or water backing:
if ref > 0,    % glass/reference
    Zb = Zr;
    bking = 0;
else    % water
    Zb = Z0;
    bking = pi;
end
R0r = (Zr - Z0)/(Zr + Z0);

for xcnt = 1:m,
    for ycnt = 1:n,
        % only care about the max of the pulse and the delay:
        [amp0 ind0] = min(pwa(:,xcnt,ycnt));
    end
end

```

```

windpwa(:,xcnt,ycnt) = pwa(ind0 + winidx,xcnt,ycnt) .* wind;
windpwi(:,xcnt,ycnt) = pwi(ind0 + winidx,xcnt,ycnt) .* wind;
[amp1 ind1] = min(pta(:,xcnt,ycnt));
windpta(:,xcnt,ycnt) = pta(ind1 + winidx,xcnt,ycnt) .* wind;
windpti(:,xcnt,ycnt) = pti(ind1 + winidx,xcnt,ycnt) .* wind;
[amp2 ind2] = max(abs(pb(:,xcnt,ycnt)));
windpb(:,xcnt,ycnt) = pb(ind2 + winidx,xcnt,ycnt) .* wind;
[ampbc indbc] = min(pbc(1:200,xcnt,ycnt));
indbc = indbc + 40; % move past signal for BC window start
windpbc(:,xcnt,ycnt) = pbc(indbc + winidxs,xcnt,ycnt) .* wind;
Pwa(:,xcnt,ycnt) = fft(windpwa(:,xcnt,ycnt));
Pw1a = Pwa(2:hlen,xcnt,ycnt); % match up pos freq's
Pwi(:,xcnt,ycnt) = fft(windpwi(:,xcnt,ycnt));
Pw1i = Pwi(2:hlen,xcnt,ycnt); % match up pos freq's
Pta(:,xcnt,ycnt) = fft(windpta(:,xcnt,ycnt));
Pt1a = Pta(2:hlen,xcnt,ycnt);
Pti(:,xcnt,ycnt) = fft(windpti(:,xcnt,ycnt));
Pt1i = Pti(2:hlen,xcnt,ycnt);
Pb(:,xcnt,ycnt) = fft(windpb(:,xcnt,ycnt));
Pb1 = Pb(2:hlen,xcnt,ycnt);
Pbc(:,xcnt,ycnt) = fft(windpbc(:,xcnt,ycnt));
Pbc1 = Pbc(2:hlen,xcnt,ycnt);

% determine thickness:
if exist('vwf3')==1,
    th(xcnt,ycnt) = ( tm_r - (tm_t + ind1*tsample) )*c0/2;
else
    th(xcnt,ycnt) = act_th;
end

% next, find phase spectra:
thetat(:,xcnt,ycnt) = angle(Pt1a);
thetab(:,xcnt,ycnt) = angle(Pb1) - bking;
% unwrapping routine:
for s = 6:hlen-1,
    while thetat(s,xcnt,ycnt) > (thetat(s-1,xcnt,ycnt) + pi/2),
        thetat(s:end,xcnt,ycnt) = thetat(s:end,xcnt,ycnt) - 2*pi;
        uwcnt1 = uwcnt1 + 1;
    end
    uwdist(xcnt,ycnt) = uwcnt1;
    while thetab(s,xcnt,ycnt) > (thetab(s-1,xcnt,ycnt) + pi/2),
        thetab(s:end,xcnt,ycnt) = thetab(s:end,xcnt,ycnt) - 2*pi;

```

```

        uwcnt2 = uwcnt2 + 1;
    end
end
for s = 7:-1:2,
    while thetat(s,xcnt,ycnt) > (thetat(s-1,xcnt,ycnt) - pi/2),
        thetat(1:s-1,xcnt,ycnt) = thetat(1:s-1,xcnt,ycnt) + 2*pi;
    end
    while thetab(s,xcnt,ycnt) > (thetab(s-1,xcnt,ycnt) - pi/2),
        thetab(1:s-1,xcnt,ycnt) = thetab(1:s-1,xcnt,ycnt) + 2*pi;
    end
end
    ang1(:,xcnt,ycnt) = thetat(:,xcnt,ycnt) ...
- 2*pi.*freq*(t01+ind1*tsample);
    ang2(:,xcnt,ycnt) = thetab(:,xcnt,ycnt) ...
- 2*pi.*freq*(t02+ind2*tsample);

    % now that we have the phase spectra, find speed:
    c1(:,xcnt,ycnt) = (4*pi.*freq*th(xcnt,ycnt)) ...
./(ang1(:,xcnt,ycnt)-ang2(:,xcnt,ycnt));

    % find amplitude next:
    aPwa(:,xcnt,ycnt) = abs(Pw1a);
    aPwi(:,xcnt,ycnt) = abs(Pw1i);
    aPta(:,xcnt,ycnt) = abs(Pt1a);
    aPti(:,xcnt,ycnt) = abs(Pt1i);
    aPb(:,xcnt,ycnt) = abs(Pb1);
    aPbc(:,xcnt,ycnt) = abs(Pbc1);

    % next, find impedance. first compute R01:
    R01i(:,xcnt,ycnt) = R0r * aPti(:,xcnt,ycnt) ./ aPwi(:,xcnt,ycnt);
    R01a(:,xcnt,ycnt) = R0r * aPta(:,xcnt,ycnt) ./ aPwa(:,xcnt,ycnt);
    Z1(:,xcnt,ycnt) = Z0 * (1 + R01i(:,xcnt,ycnt)) ...
./ (1 - R01i(:,xcnt,ycnt));

    % finally, determine attenuation:
    % first find refl and trans coeff's:
    T01 = 2*Z1 ./ (Z1 + Z0);
    T10 = 2*Z0 ./ (Z1 + Z0);
    R1r = (Zb - Z1) ./ (Zb + Z1);
    lnarg = log(abs(aPta(:,xcnt,ycnt) .* T01(:,xcnt,ycnt) ...
.* R1r(:,xcnt,ycnt) .* T10(:,xcnt,ycnt) ...
./ (aPb(:,xcnt,ycnt) .* R01a(:,xcnt,ycnt))));

```

```

alpha(:,xcnt,ycnt) = lnarg ./ (2*th(xcnt,ycnt));

rho_s(:,xcnt,ycnt) = Z1(:,xcnt,ycnt) ./ c1(:,xcnt,ycnt);
% backscatter:
eps(:,xcnt,ycnt) = 16*(rho_s(:,xcnt,ycnt) .* c1(:,xcnt,ycnt) ...
/(rho_0 * c0)).^2 ./ ((1+rho_s(:,xcnt,ycnt) .* c1(:,xcnt,ycnt) ...
/(rho_0 * c0)).^4);
end
end
% increase number for max number of function evaluations:
maxevals = 2000*length(freq(idxmin:idxmax)); % default: 200*length(x)
maxiter = 2000; % default: 20
mnfe = optimset('MaxFunEvals',maxevals,'MaxIter',maxiter);
for xcnt = 1:m,
    for ycnt = 1:n,
        % determine alpha and power law, y, for expected freq range:
        ay = fminsearch('lsealpha',[1e-8, 1.3],mnfe, ...
freq(idxmin:idxmax), alpha(idxmin:idxmax,xcnt,ycnt));
        a1(xcnt,ycnt) = ay(1);
        y(xcnt,ycnt) = ay(2);
        alphacal(:,xcnt,ycnt) = a1(xcnt,ycnt) ...
.* abs(freq(1:idxmax)).^y(xcnt,ycnt);
        % convert alpha1 for TCM:
        alrad(xcnt,ycnt) = a1(xcnt,ycnt)./( (2*pi)^y(xcnt,ycnt) );
    end
end
% check sound speed by matching with time causal model:
% first make sure y is not an odd integer:
if y == 1,
    disp('y = 1')
end
for f = 1:idxmax-idxmin+1,
    fcnt = f + idxmin-1;
    for xcnt = 1:m,
        for ycnt = 1:n,
            del_v(f,xcnt,ycnt) = alrad(xcnt,ycnt) ...
.*tan(pi*y(xcnt,ycnt)/2) .* ( omega(fcnt).^(y(xcnt,ycnt)-1) ...
- omegacen.^(y(xcnt,ycnt)-1) );
            c_tcm(f,xcnt,ycnt) = 1/( 1/c1(fc,xcnt,ycnt) ...
+ del_v(f,xcnt,ycnt) );
        end
    end
end
end

```

```

end

rbar = D + th/2;
rsPwa = reshape(aPwa,szfreq(1),xcnt*ycnt);
rsPbc = reshape(aPbc,szfreq(1),xcnt*ycnt);
Vbc = rsPbc.^2;
Vw = rsPwa.^2;
for fcnt = 1:szfreq(1),
    mVbc(fcnt) = mean(Vbc(fcnt,:)); % spatial average of scatterer
    sVbc(fcnt) = std(Vbc(fcnt,:));
    mVw(fcnt) = mean(Vw(fcnt,:)); % system calibration resp can be
% avg'd over space, shouldn't vary, necessarily
end
size(mVbc)
for xcnt = 1:m,
    for ycnt = 1:n,
        % effective sample length:
        l_eff(xcnt,ycnt) = c1(fc,xcnt,ycnt)*(tau-tau_p)/2;
        al_s = alpha(:,xcnt,ycnt);
        c1_s = c1(:,xcnt,ycnt);
        D_s = pi*apt^2*E_inf / (D^2);
        A_s(:,xcnt,ycnt) = exp(-4*al_s*( rbar(xcnt,ycnt)-D) ) ...
            .* ( exp(2*al_s*tau_p.*c1_s) - exp(-2*al_s*tau_p.*c1_s) ) ...
            ./ (4*al_s*tau_p.*c1_s) .* ( exp(2*al_s*l_eff(xcnt,ycnt)) ...
            - exp(-2*al_s*l_eff(xcnt,ycnt)) ) ./ (4*al_s*l_eff(xcnt,ycnt));
        eta(:,xcnt,ycnt) = (mVbc./mVw)' .* D_s ...
            ./ (D_ref .* eps(:,xcnt,ycnt) .* A_s(:,xcnt,ycnt) ...
            .* l_eff(xcnt,ycnt));
    end
end
end

% ----- end singleanal_vabc -----

% ----- start lsealpha -----
% lsealpha.m: least-squares error routine
% for determining power law fit for attenuation.
% written: Caleb Farny, 11/12/02
% -----
function lse = lsealpha(ay,freq,alpha)
% a(1) is alpha1 and a(2) is y:
alphac = ay(1)*abs(freq).^ay(2);
lse = sum( (alphac-alpha).^2);

```

```
% ----- end lsealpha -----
```


Bibliography

- [1] V.C. Anderson, "Sound scattering from a fluid sphere," *Journal of the Acoustical Society of America* 22 (4) (1950) 426.
- [2] M.E. Anderson, M.S.C. Soo, G.E. Trahey, "Microcalcifications as elastic scatterers under ultrasound," *IEEE Transactions on Ultrasonics, Ferroelectrics and Frequency Control* 45 (4) (1998) 925.
- [3] D.T. Blackstock, *Fundamentals of physical acoustics* (John Wiley & Sons, New York, 2000)
- [4] M.E. Brezinski, G.J. Tearney, B.E. Bouma, J.A. Izatt, M.R. Hee, E.A. Swanson, J.F. Southern, J.G. Fujimoto, "Optical coherence tomography for optical biopsy: Properties and demonstration of vascular pathology," *Circulation* 93 (6) (1996) 1206.
- [5] S.L. Bridal, P. Fornes, P. Bruneval, G. Berger, "Parametric (integrated backscatter and attenuation) images constructed using backscattered radio frequency signals (25-56 MHz) from human aortae *in vitro*," *Ultrasound in Medicine and Biology* 23 (2) (1997) 215.

- [6] M.M. Burlew, E.L. Madsen, J.A. Zagzebski, R.A. Banjavic, "A new ultrasound tissue-equivalent material," *Radiation* 134 (1980) 517.
- [7] J.A. Campbell, R.C. Waag, "Normalization of ultrasonic scattering measurements to obtain average differential scattering cross sections for tissues," *Journal of the Acoustical Society of America* 74 (2) (1983) 393.
- [8] X. Chen, D. Phillips, K.Q. Schwarz, J.G. Mottley, K.J. Parker, "The Measurement of Backscatter Coefficient from a Broadband Pulse-Echo System: A New Formulation," *IEEE Transactions on Ultrasonics, Ferroelectrics and Frequency Control* 44 (2) (1997) 515.
- [9] X. Chen, K.Q. Schwartz, K.J. Parker, "Acoustic coupling from a focused transducer to a flat plate and back to the transducer," *Journal of the Acoustical Society of America* 95 (1994) 3094.
- [10] J.-F. Chen, J.A. Zagzebski, E.L. Madsen, "Tests of backscatter coefficient measurement using broadband pulses," *IEEE Transactions on Ultrasonics, Ferroelectrics and Frequency Control* 40 (5) (1993) 603.
- [11] T. Chklovski, "Scanning Acoustic Microscope for Characterization of Arterial Plaque," Master's Degree Thesis, Boston University (2003)
- [12] D.H. Cormack, *Basic Histology*, Lippincott-Raven (1997)
- [13] R.S. Cotran, T. Collins, B. Schmitt, editors, *Robbins Pathologic Basis of Disease, 6th ed.* Elsevier Science, 1998. Ch. 12, 498-515.

- [14] F.T. D'Astous, F.S. Foster, "Frequency dependence of ultrasound attenuation and backscatter in breast tissue," *Ultrasound in Medicine and Biology* 12 (10) (1986) 795.
- [15] A.C. De Franco, S.E. Nissen, "Intravascular ultrasound: Implications for understanding the development and potential regression of atherosclerosis," *American Journal of Cardiology* 88 (2001) 7.
- [16] V.A. Del Grosso, C.W. Mader, "Speed of sound in pure water," *Journal of the Acoustical Society of America* 52 (5) (1972) 1442.
- [17] C.L. Dent, M.J. Scott, S.A. Wickline, C.S. Hall, "High-frequency ultrasound for quantitative characterization of myocardial edema," *Ultrasound in Medicine and Biology*, 26 (3) (2000) 375.
- [18] E. Falk, P.K. Shah, V. Fuster, "Coronary plaque disruption," *Circulation* 92 (1995) 657.
- [19] J.J. Faran, "Sound scattering by solid cylinders and spheres," *Journal of the Acoustical Society of America* 23 (1951) 405.
- [20] S. Fields, F. Dunn, "Correlation of echographic visualizability of tissue with biological composition and physiological state," *Journal of the Acoustical Society of America* 54 (1973) 809.
- [21] S.A. Goss, R.L. Johnston, F. Dunn, "Comprehensive compilation of empirical ultrasonic properties of mammalian tissues," *Journal of the Acoustical Society of America* 64 (2) (1978) 423.

- [22] J.F. Greenleaf, F.A. Duck, W.F. Samayoa, S.A. Johnson, "Ultrasonic data acquisition and processing system for atherosclerotic tissue characterization," 1974 Ultrasonic Symposium Proceedings 738.
- [23] E.J. Gussenhoven, C.S. Essed, C.T. Lancee, F. Mastik, P. Frietman, F.C. Van Egmond, J. Reiber, H. Bosch, H. Van Urk, J. Roelandt, N. Bom, "Arterial wall characteristics determined by intravascular ultrasound imaging: An in vitro study," *Journal of the American College of Cardiology* 14 (4) (1989) 947.
- [24] C.S. Hall, C.T. Nguyen, M.J. Scott, G.M. Lanza, S.A. Wickline, "Delineation of the extracellular determinants of ultrasonic scattering from elastic arteries," *Ultrasound in Medicine and Biology* 26 (4) (2000) 613.
- [25] P. He, "Experimental verification of models for determining dispersion from attenuation," *IEEE Transactions on Ultrasonics, Ferroelectrics and Frequency Control* 46 (1999) 706.
- [26] P. He, "Measurement of acoustic dispersion using both transmitted and reflected pulses," *Journal of the Acoustical Society of America* 107 (2002) 801.
- [27] P. He, J. Zheng, "Acoustic dispersion and attenuation measurement using both transmitted and reflected pulses," *Ultrasonics* 39 (2001) 27.
- [28] C.R. Hill, *Physical Principles of Medical Ultrasonics* New York: Ellis Harwood

- [29] D. Huang, E.A. Swanson, C.P. Lin, J.S. Schuman, W.G. Stinson, W. Chang, M.R. Hee, T. Flotte, K. Gregory, C.A. Puliafito, J.G. Fujimoto, "Optical coherence tomography," *Science* 254 (1991) 1178.
- [30] M.F. Insana, R.F. Wagner, D.G. Brown, T.J. Hall, "Describing small-scale structure in random media using pulse-echo ultrasound," *Journal of the Acoustical Society of America* 87 (1) (1990) 179.
- [31] M.F. Insana, T.J. Hall, "Parametric ultrasound imaging from backscatter coefficient measurements image formation and interpretation," *Ultrasonic Imaging* 12 (1990) 245.
- [32] I.-K. Jang, B.E. Bouma, D.-H. Kang, S.-J. Park, S.-W. Park, K.-B. Choi, M. Shishkov, K. Schlendorf, E. Pomerantsev, S.T. Houser, H.T. Aretz, G.J. Tearney, "Visualization of coronary atherosclerotic plaques in patients using optical coherence tomography: Comparison with intravascular ultrasound," *Journal of the American College of Cardiology* 39 (4) (2002) 609.
- [33] C.L. de Korte, E.I. Cespedes, A.F.W. Van Der Steen, C.T. Lancee, "Intravascular elasticity imaging using ultrasound: Feasibility studies in phantoms," *Ultrasound in Medicine and Biology* 23 (5) (1997) 735.
- [34] D.J. Lee, B. Sigel, V.J.K. Swami, J.R. Justin, V. Gahtan, S.P. O'Brien, L. Dwyer-Joyce, E.J. Feleppa, A.B. Roberts, H.D. Berkowitz, "Determination of carotid plaque risk by ultrasonic tissue characterization", *Ultrasound in Medicine and Biology* 24 (9) (1998) 1291.

- [35] G.R. Lockwood, L.K. Ryan, J.W. Hunt, F.S. Foster, "Measurement of the ultrasonic properties of vascular tissues and blood from 35-65 MHz," *Ultrasound in Medicine and Biology* 17 (7) (1991) 653.
- [36] G.R. Lockwood, L.K. Ryan, A.I. Gotlieb, E. Lonn, J.W. Hunt, P. Liu, F.S. Foster, "In vitro high resolution intravascular imaging in muscular and elastic arteries," *Journal of the American College of Cardiology* 20 (1) (1992) 153.
- [37] J.C. Machado, F.S. Foster, "Validation of theoretical diffraction correction functions for strongly focused high frequency ultrasonic transducers," *Ultrasonic Imaging* 21 (1999) 95.
- [38] J.C. Machado, F.S. Foster, "Ultrasonic integrated backscatter coefficient profiling of human coronary arteries in vitro," *IEEE Transactions on Ultrasonics, Ferroelectrics and Frequency Control* 48 (1) (2001) 17.
- [39] B.D. MacNeill, H.C. Lowe, M. Takano, V. Fuster, I.-K. Jang, "Intravascular modalities for detection of vulnerable plaque: current status," *Arteriosclerosis, Thrombosis and Vascular Biology* 23 (2003) 1333.
- [40] E.L. Madsen, J.A. Zagzebski, R.A. Banjavie, R.E. Jutila, "Tissue mimicking materials for ultrasound phantoms," *Medical Physics* 5 (5) (1978) 391.
- [41] E.L. Madsen, M.F. Insana, J.A. Zagzebski, "Method of data reduction for accurate determination of acoustic backscatter coefficients," *Journal of the Acoustical Society of America* 76 (3) (1984) 913.

- [42] E.L. Madsen, G.R. Frank, F. Dong, "Liquid or solid ultrasonically tissue-mimicking materials with very low scatter," *Ultrasound in Medicine and Biology* 24 (4) (1998) 535.
- [43] E.L. Madsen, F. Dong, G.R. Frank, B.S. Garra, K.A. Wear, T. Wilson, J.A. Zagzebski, H.L. Miller, K.K. Shung, S.H. Wang, E.J. Feleppa, T. Liu, W.D. O'Brien, K.A. Topp, N.T. Sanghvi, A.V. Zaitsev, T.J. Hall, J.B. Fowlkes, O.D. Kripfgans, J.G. Miller, "Interlaboratory comparison of ultrasonic backscatter, attenuation, and speed measurements," *Journal of Ultrasound in Medicine* 18 (1999) 615.
- [44] J.N. Marsh, M.S. Hughes, C.S. Hall, S.H. Lewis, R.L. Trousil, G.H. Brandenburger, H. Levene, J.G. Miller, "Frequency and concentration dependence of the backscatter coefficient of the ultrasound contrast agent Albunex (R)," *Journal of the Acoustical Society of America* 104 (3) (1998) 1654.
- [45] J.N. Marsh, M.S. Hughes, G.H. Brandenburger, J.G. Miller, "Broadband measurement of the scattering-to-attenuation ratio for Albunex (R) at 37 degrees C," *Ultrasound in Medicine and Biology* 25 (8) (1999) 1321.
- [46] C.R. Meyer, E.H. Chiang, K.P. Fechner, D.W. Fitting, D.M. Williams, A.J. Buda, "Feasibility of high-resolution, intravascular ultrasonic imaging catheters," *Radiology* 168 (1988) 113.
- [47] T. Noritomi, B. Sigel, V. Swami, J. Justin, V. Gahtan, X. Chen, E.J. Feleppa, A.B. Roberts, K. Shirouzu, "Carotid plaque typing by multiple-parameter ultrasonic tissue

- characterization,” *Ultrasound in Medicine and Biology* 23 (5) (1997) 643.
- [48] M. O’Donnell, E.T. Jaynes, J.G. Miller, “General relationships between ultrasonic attenuation and dispersion,” *Journal of the Acoustical Society of America* 63 (6) (1978) 1935.
- [49] M. O’Donnell, E.T. Jaynes, J.G. Miller, “Kramers-Kronig relationship between ultrasonic attenuation and phase velocity,” *Journal of the Acoustical Society of America* 69 (3) (1981) 696.
- [50] S. Ohe, ”Distillation, Vapor Pressure, Vapor-Liquid Equilibria”, www.s-ohe.com
- [51] O’Neil, “Theory of focusing radiators,” *Journal of the Acoustical Society of America* 21 (5) (1949) 516.
- [52] A.D. Pierce, *Acoustics* Acoustical Society of America, Woodbury, New York, 1994 edition, 1994, 428-431.
- [53] B.I. Raju, M.A. Srinivasan, “High-frequency ultrasonic attenuation and backscatter coefficients of in vivo normal human dermis and subcutaneous fat,” *Ultrasound in Medicine and Biology* 27 (11) (2001) 1543.
- [54] V. Roberjot, S.L. Bridal, P. Laugier, G. Berger, “Absolute backscatter coefficient over a wide range of frequencies in a tissue-mimicking phantom containing two populations of scatterers,” *IEEE Transactions on Ultrasonics, Ferroelectrics and Frequency Control* 43 (5) (1996) 970.

- [55] J.H. Rose, M.R. Kaufmann, S.A. Wickline, C.S. Hall, J.G. Miller, "A proposed microscopic elastic wave theory for ultrasonic backscatter from myocardial tissue," *Journal of the Acoustical Society of America* 97 (1) (1995) 656.
- [56] L.K. Ryan, F.S. Foster, "Tissue equivalent vessel phantoms for intravascular ultrasound," *Ultrasound in Medicine and Biology* 23 (2) (1997) 261.
- [57] Y. Saijo, H. Sasaki, H. Okawai, S. Nitta, M. Tanaka, "Acoustic properties of atherosclerosis of human aorta obtained with high-frequency ultrasound," *Ultrasound in Medicine and Biology* 24 (7) (1998) 1061.
- [58] R.A. Sigelmann, J.M. Reid, "Analysis and measurement of ultrasonic backscattering from an ensemble of scatterers excited by sinewave bursts," *Journal of the Acoustical Society of America* 53 (1973) 1351.
- [59] T. Spencer, M.P. Ramo, D.M. Salter, T. Anderson. P.P. Kearney, G.R. Sutherland, K.A.A. Fox, W.N. McDicken, "Characterisation of atherosclerotic plaque by spectral analysis of intravascular ultrasound: An in vitro methodology," *Ultrasound in Medicine and Biology* 23 (2) (1997) 191.
- [60] T.L. Szabo, "Time domain wave equations for lossy media obeying a frequency power law," *Journal of the Acoustical Society of America* 96 (1) (1994) 491.
- [61] T.L. Szabo, "Causal theories and data for acoustic attenuation obeying a frequency power law," *Journal of the Acoustical Society of America* 97 (1995) 14.

- [62] T.L. Szabo, J. Wu, "A model for longitudinal and shear wave propagation in viscoelastic media," *Journal of the Acoustical Society of America* 107 (5) (2000) 2437.
- [63] T. Thieme, K.D. Wernecke, R. Meyer, E. Brandenstein, D. Habedank, A. Hinz, S.B. Felix, G. bauman,, F.X. Kleber, "Angioscopic evaluation of atherosclerotic plaques: validation by histomorphologic analysis and association with stable and unstable coronary syndromes," *Journal of the American College of Cardiology* 28 (1) (1996) 1.
- [64] V. Twersky, "Acoustic bulk parameters of random volume distributions of small scatterers," *Journal of the Acoustical Society of America* 36 (7) (1964) 1314.
- [65] M.P. Urbani, E. Picano, G. Parenti, A. Mazzarisi, L. Fiori, M. Paterni, G. Pelosi, L. Landini, "In vivo radiofrequency-based ultrasonic tissue characterization of the atherosclerotic plaque," *Stroke* 24 (10) (1993) 1507.
- [66] J. Van Cauwelaert, "Use of μ CT to follow the propagation of crack formation in IU and real kidney stones," Master's Degree Thesis, Boston University (2004)
- [67] M.K. Wolverson, H.M. Bashiti, G.J. Peterson, "Ultrasonic tissue characterization of atheromatous plaques using a high resolution real time scanner," *Ultrasound in Medicine and Biology* 9 (6) (1983) 599.
- [68] J. Wu, "Determination of velocity and attenuation of shear waves using ultrasonic spectroscopy," *Journal of the Acoustical Society of America* 99 (5) (1996) 2871.

- [69] L.X. Yao, J.A. Zagzebski, E.L. Madsen, "Backscatter coefficient measurements using a reference phantom to extract depth-dependent instrumentation factors," *Ultrasonic Imaging* 12 (1990) 58.

Vita

Caleb Hooper Farny was born in 1979 in Lincoln, Massachusetts. He attended Hartwell Elementary School and Brooks Middle School in Lincoln. He studied piano at the Rivers Music School from 1992-1997 and played double bass with the Youth Philharmonic Orchestra at the New England Conservatory of Music from 1994-1997. He graduated from Lincoln-Sudbury Regional High School in 1997, where he was on the cross-country ski team.

He attended the University of Rochester on a Rush Rhees Scholarship, where he studied mechanical engineering in the Class of 2001. In addition, he studied piano at the Eastman School of Music and played the double bass in the Symphony Orchestra on the River Campus.

A summer abroad, spent researching hydraulics at the Tampere University of Technology, led to the idea of studying acoustics, a blend of his musical and engineering interests. He started the master's program at the Department of Aerospace and Mechanical Engineering at Boston University in the fall of 2001 and had the good fortune to study with Robin Cleveland in the summer of 2002.

Permanent Address: 241 Lincoln Road, Lincoln MA, 01773.

This document was typeset using L^AT_EX by the author.